AD NUMBER

AD882000

NEW LIMITATION CHANGE

TO

Approved for public release, distribution unlimited

FROM

Distribution authorized to U.S. Gov't. agencies and their contractors; Critical Technology; NOV 1970. Other requests shall be referred to Air Force Armament Lab., Attn: DLRA, Eglin AFB, FL 32542.

AUTHORITY

Air Force Armament Development and Test Center ltr dtd 4 Aug 1976

AFATL-TR-70-123

AD882000

AD No.

CB (2)

AERODYNAMIC DISPERSION TECHNIQUES

ALPHA RESEARCH, INC.

TECHNICAL REPORT AFATL-TR-70-123

NOVEMBER 1970

AIR FORCE ARMAMENT LABORATORY

AIR FORCE SYSTEMS COMMAND • UNITED STATES AIR FORCE

EGLIN AIR FORCE BASE, FLORIDA

160

Aerodynamic Dispersion Techniques

James E. Brunk

FOREWORD

This final report documents work accomplished during the period 6 October 1969 through 6 October 1970, by Alpha Research, Inc., Santa Barbara, California, under Contract No. F08635-70-C-0012 with the Air Force Armament Laboratory, Eglin Air Force Base, Florida. Monitoring the program for the Armament Laboratory were Messrs. Edward S. Sears and Kenneth K. Cobb (DLRA). The principal investigator for the contractor was Mr. James E. Brunk.

Digital computer services in support of this effort were provided by the Armament Development and Test Center, Eglin Air Force Base, Florida.

Transonic wind tunnel test support, including model design and fabrication services, were provided by the 4T Projects Branch, PWT, Arnold Engineering Development Center, Arnold Air Force Station, Tennessee.

Information in this report is embargoed under the Department of State International Traffic In Arms Regulations. This report may be released to foreign governments by departments or agencies of the U. S. Government subject to approval of the Air Force Armament Laboratory (DLRA), Eglin AFB, Florida 32542, or higher authority within the Department of the Air Force. Private individuals or firms require a Department of State export license.

This technical report has been reviewed and is approved.

CHARLES K. ARPKE, Lt. Colonel, USAF
Chief, Technology Division

ii

ABSTRACT

The motion and dispersion characteristics of four proposed types of aerodynamic self-dispersing bomblets (S-curve bomblet, roll-through-zero bomblet, dual-mode bomblet, and spinning-disk bomblet) are evaluated for representative tactical cluster-dispenser delivery environments. Six-degrees-of-freedom simulations are used to investigate the flight dynamics of each type bomblet, and in addition, approximate motion theories are developed for the S-curve and roll-through-zero bomblets. The effects of various configurational asymmetries on the motion and dispersion are considered.

Impact patterns are computed for each of the proposed bomblets, and the area coverage capabilities are compared for low-speed and high-speed dispenser opening conditions, ranging in altitude from 300 to 2000 feet and flight path angle from 5 to 45 degrees. The area coverage of the proposed bomblets is contrasted with that of the CBU-24 munition and a hypothetical radial-force-ejection system.

The aerodynamic characteristics of each type bomblet are reviewed, and the problems of selecting candidate configuration are discussed. Results of supporting wind tunnel tests, accomplished in the 4T transonic wind tunnel at the Arnold Engineering Development Center (AEDC), are briefly described.

iii
(The reverse of this page is blank)

TABLE OF CONTENTS

LIST OF FIGURES

)

LIST OF FIGURES (Continued)

LIST OF FIGURES (Continued)

LIST OF FIGURES (Concluded)

LIST OF TABLES

LIST OF SYMBOLS

Symbol	Definition	Fortran Equivalent
C_D	Drag coefficient	
C_L	Lift coefficient	
C_{l_δ}	Fin effectiveness parameter	
C_x	Axial force coefficient	CX
C_N	Normal force coefficient	CN
C_M	Overturning moment coefficient	CM
C_{m_q}	Damping derivative ($\vec{\alpha}$ plane); qd/2V	CMQ
C_{n_r}	Damping derivative (Magnus plane); rd/2V	CNR
$C_{m_{pr}}$	Angular velocity coupling derivative; pd/2V, rd/2V	CMPR
$C_{n_{pq}}$	Angular velocity coupling derivative; pd/2V, qd/2V	CNPQ
C_{N_p}	Magnus force coefficient; pd/2V	CNPA
C_l	Spin torque coefficient	CL
C_{l_p}	Spin damping coefficient; pd/2V	CLP
C_{M_p}	Magnus moment coefficient; pd/2V	CMPA
C_{y_0}	Trim force coefficient along y body-fixed axis	CYO
C_{z_0}	Trim force coefficient along z body-fixed axis	CZO
C_{m_0}	Trim moment coefficient about y body-fixed axis	CMO
C_{n_0}	Trim moment coefficient about z body-fixed axis	CNO
C_{SF_1}	Side force coefficient due to aerodynamic roll angle	CSF1
C_{N_1}	Normal force coefficient due to aerodynamic roll angle	CN1
C_{SF_3}	Side force coefficient due to asymmetric vortices	CSF3
C_{SM_1}	Side moment coefficient due to aerodynamic roll angle	CSM1
C_{M_1}	Pitching moment coefficient due to aerodynamic roll angle	CM1
C_{SM_3}	Side moment coefficient due to asymmetric vortices	CSM3
$C_{l_{\phi_1}}$	Roll moment coefficient due to aerodynamic roll angle	CLPH1
$C_{l_{\phi_2}}$	Roll moment coefficient due to aerodynamic roll angle	CLPH2

LIST OF SYMBOLS (Continued)

Symbol	Definition
d	Aerodynamic reference length, ft (body diameter)
$\vec{F}$	Total aerodynamic force
g	Acceleration due to gravity, ft/sec^2
h	Altitude of dispenser function, ft
i	$\sqrt{-1}$
I_x	Axial moment of inertia, $slug\text{-}ft^2$
I_x'	$I_x/\rho Sd^3$, nondimensional inertia
I	Transverse moment of inertia, $slug\text{-}ft^2$
I'	$I/\rho Sd^3$, nondimensional inertia
$[I]$	Moment of inertia tensor
ℓ	Length of body not including stabilizing appendages, ft
m	Mass, slugs
m'	$m/\rho Sd$, nondimensional mass
M	Mach number
$\vec{M}$	Total aerodynamic moment
p	Roll rate, angular velocity about x axis, radians/sec
q	Pitch rate, angular velocity about y axis, radians/sec
r	Yaw rate, angular velocity about z axis, radians/sec
r	Cross-range impact dispersion, ft
R	Along-range impact dispersion, ft
S	Aerodynamic reference area ($\pi d^2/4$, for S-curve, RT0, and disk bomblets; $\ell \times d$, for dual-mode bomblet)
t	Time, seconds
$\hat{t}$	$(V/d)t$, nondimensional time
u	Axial velocity in direction of x axis, ft/sec
v	Velocity in direction of y axis, ft/sec
V	Total velocity, ft/sec
w	Velocity in direction of z axis, ft/sec

xii

LIST OF SYMBOLS (Concluded)

Symbol	Definition
x, y, z,	Body axes, x is axis of symmetry
x, y', z'	Fixed-plane axes
y_e, z_e	Earth-fixed axes perpendicular to line of flight
XYZ	Earth-fixed axes, Z down
$\vec{\alpha}$	Total angle of attack
α_T	Trim angle of attack
γ	Flight path angle with respect to horizontal
$\Delta\gamma$	Change in flight path angle
δ	Fin or wing differential deflection or cant, radians
ζ	Phase angle of symmetry plane (Figure I-3)
ζ	Vane trail angle
Θ	Euler elevation angle
λ	Euler angle for coning motion analysis (Appendix II)
ξ	Angle of attack plane parameter (Figure I-3)
ρ	Air density
σ	Euler angle for coning motion analysis (Appendix II)
$\phi, \tilde{\phi}$	Body roll orientation (Figure I-3, Figure II-1)
$\tilde{\phi}$	Angle of attack plane orientation from vertical (Figure II-1)
Φ	Aerodynamic roll angle (Figure I-3)
$\bar{\Phi}$	Angle of attack plane orientation from horizontal (Figure I-3)
$\vec{\Omega}$	General rotation velocity vector for triad
$\vec{\omega}$	Total angular velocity vector of body

Subscripts

( )$_o$	Initial value
( )$_T$	At trim angle of attack

Superscripts

($\dot{\ }$)	Time derivative
( )'	Derivative with respect to nondimensional distance

(The reverse of this page is blank)

SECTION I.

INTRODUCTION

The increasing utilization of cluster-type bombs and submunition dispensers for tactical warfare has led to the need for considering various bomblet dispersion techniques. The need for new dispersion techniques, as alternatives to existing magnus-rotor and radial ejection dispersion concepts, is heightened by the trend toward lower delivery altitudes and increased delivery Mach number, as well as the need for better impact pattern distributions and improved total weapon effectiveness. Further, new self-dispersing bomblet concepts are required, which can be adapted to many different warhead types (chemical, fragmentation, shaped-change, incendiary, etc.) and which provide alignment of the bomblet axis with the flight path at impact for improved fuzing and warhead functioning.

Four new aerodynamic self-dispersing bomblet concepts have been proposed which require investigation to determine their suitability for cluster and dispenser weapons. Two of the proposed bomblet concepts (the S-curve bomblet and roll-through-zero bomblet) utilize the lift force resulting from body incidence as a means of dispersion. These axisymmetric fin-stabilized ballistic-type configurations provide rapid dispersion and impact at small angles of attack. The dual-mode bomblet concept combines the dispersion capability of the magnus rotor with the small angle of attack impact characteristic of the ballistic-type bomblet. The spinning-disk bomblet utilizes the lift characteristics of the lenticular shape as a means of improving dispersion of the magnus rotor at high Mach numbers.

The present effort encompasses (1) analytical simulation of the flight characteristics of each bomblet-type to determine the motion, trajectory, and impact pattern characteristics, (2) development of theory and computer simulation capabilities pertinent to the proposed designs, and (3) static and dynamic wind tunnel tests of candidate bomblet configurations.

SECTION II.

ANALYTICAL INVESTIGATIONS AND
FLIGHT DYNAMICS SIMULATIONS

A.   S-CURVE BOMBLET

1.   Description of Concept.

The aerodynamic scattering of bomblets, through the use of a
trim angle of attack generated by a highly nonlinear aerodynamic restoring
moment characteristic (S-curve moment variation), was first described by
Merchant and Pope[1].

The S-curve type bomblet is comprised of an axially symmetric
body-fin configuration, which is designed to provide an unstable restoring
moment at small angles of attack, and a stable pitching moment slope at a
large trim angle of attack. The lift force resulting from the large trim angle
of attack causes the trajectory to deflect, thereby providing the desired dis-
persion.

One of the features of the S-curve type bomblet is that the trim
incidence is independent of the body roll attitude, such that direction of the
lift force vector with respect to a vertical plane is either fixed, or slowly
changing, even though the bomblet has an accidental spin. This character-
istic is enhanced as the rotational symmetry of the bomblet increases.

The tendency for the angle-of-attack plane to remain stationary,
i.e., for the coning motion to be zero, is the fundamental reason for the
large dispersion of the S-curve bomblet.

2.   Zero Coning Theory.

The requirements for zero coning can be stated more
precisely by considering in detail the equations of motion for ballistic flight.
A theoretical coning motion analysis, based on the equations of motion for
the pitching and lateral translation degrees of freedom and including the axial
spin as a parameter, is presented in Appendix II. As a result of the analysis,
it is shown that the orientation of the angle of attack plane, ϕ , can be
described approximately by a second-order nonlinear differential equation

2

of the form

$$I \alpha_T \ddot{\tilde{\phi}} - \left[\frac{I g \alpha_T \sin\gamma}{V} - \frac{I C_N \rho S V}{2m} + \frac{C_{n_r} \rho S d^2 V \alpha_T}{4} \right] \dot{\tilde{\phi}}$$

$$+ \left(\frac{I_x p g \cos\gamma}{V} \right) \cos\tilde{\phi} - \left(\frac{C_{n_r} g \rho S d^2 \cos\gamma}{4} \right) \sin\tilde{\phi} = \tag{1}$$

$$\left[\frac{C_{M_p} \rho S d^2 V}{4} + \frac{I_x C_N \rho S V}{2m} - \frac{I_x g \alpha_T \sin\gamma}{V} \right] p$$

In the above equation, it is assumed that the bomblet has a trim angle of attack, α_T, due to the S-curve pitching moment.

The existence of a steady-state solution for $\tilde{\phi}$ in Equation (1) is determined by setting $\ddot{\tilde{\phi}} = \dot{\tilde{\phi}} = 0$. This results in Equation (2a).

$$p I_x \left[\frac{g \cos\gamma \cos\tilde{\phi}}{V} - \frac{C_N \rho S V}{2m} + \frac{g \alpha_T \sin\gamma}{V} \right] - \frac{C_{n_r} g \rho S d^2 \cos\gamma \sin\tilde{\phi}}{4}$$

$$- \frac{1}{4} C_{M_p} p \rho S d^2 V = 0 \tag{2a}$$

where the first term in braces is the gyroscopic moment due to rate of change of flight path curvature, the second term is the damping moment, and the third term is the magnus moment. If the gyroscopic and magnus terms approach zero, i. e., a very small value of roll rate, then the damping term must also approach zero, implying further that $\tilde{\phi}$ is near zero. For the purpose of obtaining exact solutions for $\tilde{\phi}$, it is useful to consider the following alternative form of Equation (2a):

$$A \cos\tilde{\phi} + B \sin\tilde{\phi} = C \tag{2b}$$

where

$$A = p \left[\frac{I_x g \cos\gamma}{V} \right]$$

$$B = - \left[\frac{C_{n_r} g \rho S d^2 \cos\gamma}{4} \right]$$

$$C = p \left[\frac{C_{M_p} \rho S d^2 V}{4} + \frac{I_x C_N \rho S V}{2m} - \frac{I_x g \alpha_T \sin\gamma}{V} \right]$$

3

Solutions to Equation (2b) exist for

$$C^2 \leq A^2 + B^2$$

and do not exist if

$$C^2 > A^2 + B^2$$

For flat trajectories ($\gamma \to 0$) the latter inequality can be expressed as

$$\left| \left[\frac{C_{M_p} \rho S d^2 V}{4} + \frac{I_x C_N \rho S V}{2m} \right] p \right| > \left\{ \left[\frac{I_x g p}{V} \right]^2 + \left[\frac{C_{n_r} g \rho S d^2}{4} \right]^2 \right\}^{\frac{1}{2}} \quad (3)$$

Examination of Equation (3) shows that either a large value of C_{M_p} or a large value of p will preclude the attainment of a solution for $\tilde{\phi}$. If the aerodynamic and inertial parameters are established, i.e., a specific configuration is selected, there may be a range of $|p| < |p_{CR}|$ for which solutions for $\tilde{\phi}$ exist. In such cases, p_{CR} is referred to as the critical spin rate. At spin rate less than the critical spin rate, the coning rate is zero; at spin rates greater than the critical spin rate, the coning rate is finite.

Using Equation (2), multivalued solutions are obtained for $\tilde{\phi}$, when $|p| < |p_{CR}|$. To determine whether these solutions are stable solutions to the differential Equation (1), a perturbation equation is written, using the perturbation from the steady-state solution, $\Delta \tilde{\phi}$. Development of the perturbation equation for $\Delta \tilde{\phi}$ is aided by use of the following substitutions for $\cos \tilde{\phi}$ and $\sin \tilde{\phi}$:

$$\cos \tilde{\phi} = \cos (\tilde{\phi}_o + \Delta \tilde{\phi}) = \cos \tilde{\phi} - \Delta \tilde{\phi} \sin \tilde{\phi}_o$$

$$\sin \tilde{\phi} = \sin (\tilde{\phi}_o + \Delta \tilde{\phi}) = \sin \tilde{\phi}_o + \Delta \tilde{\phi} \cos \tilde{\phi}_o$$

$$(4)$$

Using representative values for the aerodynamic and inertial parameters in Equation (1), analysis shows that stable solutions to the perturbation equations exist only when $-\frac{\pi}{2} < \tilde{\phi}_o < \frac{\pi}{2}$; outside this region the $\Delta \tilde{\phi}$ perturbations are unstable. This implies that the nose of the bomblet is always nose-up with respect to the trajectory when stable zero-coning solutions exist.

Further analysis of Equation (2) shows that for positive spin rates the nose of the bomblet points to the left of the velocity vector (as viewed in the direction of flight) when the magnus moment is negative, and to the right when the magnus moment is positive. The reverse is true for negative spin rates.

For spin rates which are larger than the critical spin rate, the average effect of the terms containing $\cos \tilde{\phi}$ and $\sin \tilde{\phi}$ is small. In such cases it is possible to have a solution for $\dot{\tilde{\phi}}$, if $\ddot{\tilde{\phi}} \simeq 0$. Examination of Equation (1) shows that a linear relationship exists between $\dot{\tilde{\phi}}$ and p , specifically, $\dot{\tilde{\phi}}/p$ = constant. A good approximation for this constant, in most instances, is

$$\frac{\dot{\tilde{\phi}}}{p} = \frac{C_{M_p}}{C_{r_r} \alpha_T} \qquad (5)$$

While the zero coning theory provides useful performance criteria, it does not readily permit a direct prediction of either the transient or steady-state swerving motion.

A direct solution of Equation(1), along with integration of the equations for lateral translation, entails great complication. Consequently, the dispersion calculations are accomplished most easily by numerical integration, using a six-degrees-of-freedom computer program.

3.   Configurations.

The geometry of the S-curve bomblet and its center-of-gravity location are selected such that the proper nonlinear restoring moment characteristic is achieved. The aerodynamic center of pressure movement must be forward at small angles of attack to produce instability, and rearward at large incidence to produce a large trim angle of attack and adequate static stability margin. Various means are available for providing the necessary center-of-pressure movement. Nose rounding, boattailing, and low aspect ratio fins all tend to move the center of pressure forward at small angles of attack and rearward at large angles of attack, and these considerations have been used in the selection of candidate designs for analytical and experimental investigation.

The S-curve bomblet,which has been most extensively investigated during the present effort,is depicted in Figure 1. The body is a two-inch-diameter,four-caliber cylinder with either a blunt nose (0.25 caliber corner radius) or hemisphere nose and six low-aspect-ratio rectangular fins. The weight of the bomblet is assumed to be 1.51 pounds. The bomblet weight was determined by use of an average mass density, calculated from the weights and volumes of a selected group of bomblet munitions. The center of gravity location (1.5 calibers aft of the nose) presumes that the rear of the bomblet is hollow to a depth of about one caliber. The hollow afterbody and the fin design permit efficient packaging, as can be seen from the schematic packaging arrangement depicted in Figure 2.

5
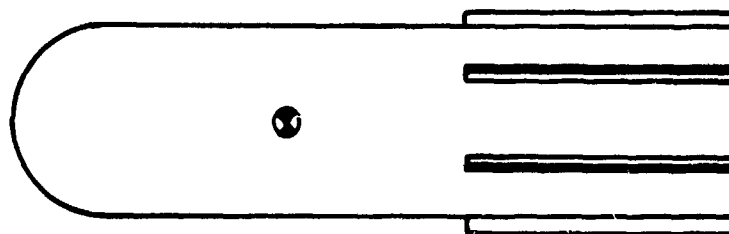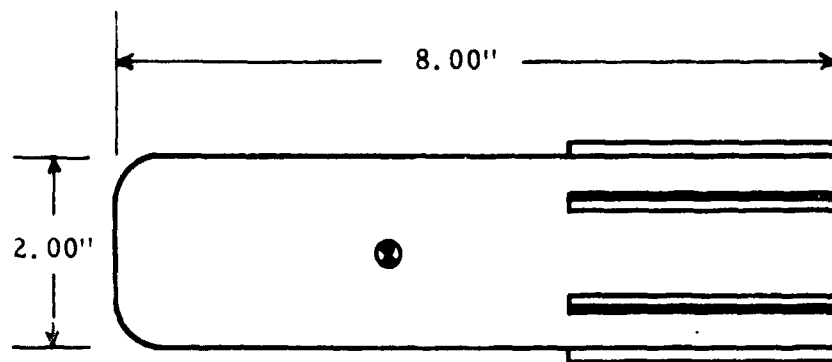
Alternate-Nose Bomblet

Physical Data

$$\text{Weight} = 1.51 \text{ pounds}$$
$$I_x = 1.629 \times 10^{-4} \text{ slug-ft}^2$$
$$I = 1.06 \times 10^{-3} \text{ slug-ft}^2$$

Figure 1. S-Curve Bomblet Physical Characteristics
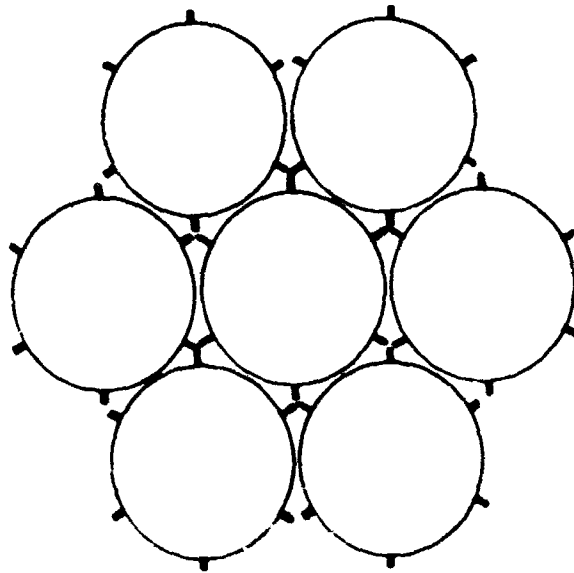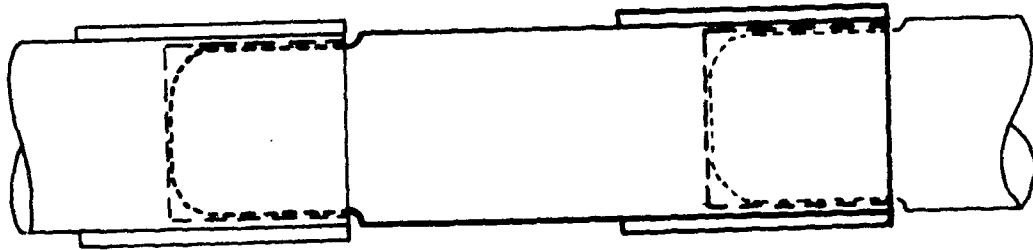
Figure 2.   Concepts for S-Curve Bomblet Packaging

The 4:1 fineness ratio body was selected primarily as a compromise between warhead geometry and aerodynamic considerations. The original S-curve bomblet configurations investigated by the Australian Weapons Research Establishment [1] were 5.73 calibers in length, but this fineness ratio is considered too large for a fragmenting warhead. A low fineness ratio bomblet was not chosen, because preliminary aerodynamic data for a series of two-caliber S-curve bomblets, which are under investigation by the Air Force Armament Laboratory, showed the aerodynamic moment curves to be quite sensitive to small configuration changes. This is probably due to the fact that the separated flow from the blunt nose extends rearward about two body diameters.

Several geometric modifications to the basic four-caliber S-curve bomblet were evaluated as a part of the wind tunnel test program (see Section IV). These alternate configurations have different trim, stability, and drag characteristics, and for some applications may be more suitable than the configurations shown in Figure 1. These factors will be discussed in subsequent sections.

Two different nose shapes are specified for the basic configuration because of the variation of the trim angle of attack with Mach number. The blunt nose bomblet trims at zero angle of attack at transonic Mach numbers, whereas the hemisphere-nose bomblet exhibits a finite trim angle of attack through the transonic regime.

4. Aerodynamic Characteristics.

The complete aerodynamic characteristics of the basic S-curve bomblet configuration (Figure 1) were required for the motion simulations and trajectory investigations. The static aerodynamic force and moment coefficients for the basic configurations were obtained from the AEDC wind tunnel tests described in Section IV (model designations $B_S N_{S1} A_{S1} F_{S2}$ and $B_S N_{S2} A_{S1} F_{S2}$ for blunt-nose and hemisphere-nose configurations, respectively). Plots of the restoring moment and normal force coefficients for these configurations, at Mach 0.3 and 0.9, are shown in Figure 3. The variation of the trim angle of attack with Mach number for each configuration is illustrated in Figure 4.

Because the results of the dynamic wind tunnel tests at AEDC were not available, pitch-damping, magnus-force and moment, roll-damping, and fin-effectiveness data were obtained from wind tunnel test results for a similar 5.73 caliber bomblet with eight low-aspect ratio fins [2]. The aerodynamic coefficients were assumed to be valid for the four-caliber bomblet without correction for fineness ratio, number of fins, or center-of-gravity location.
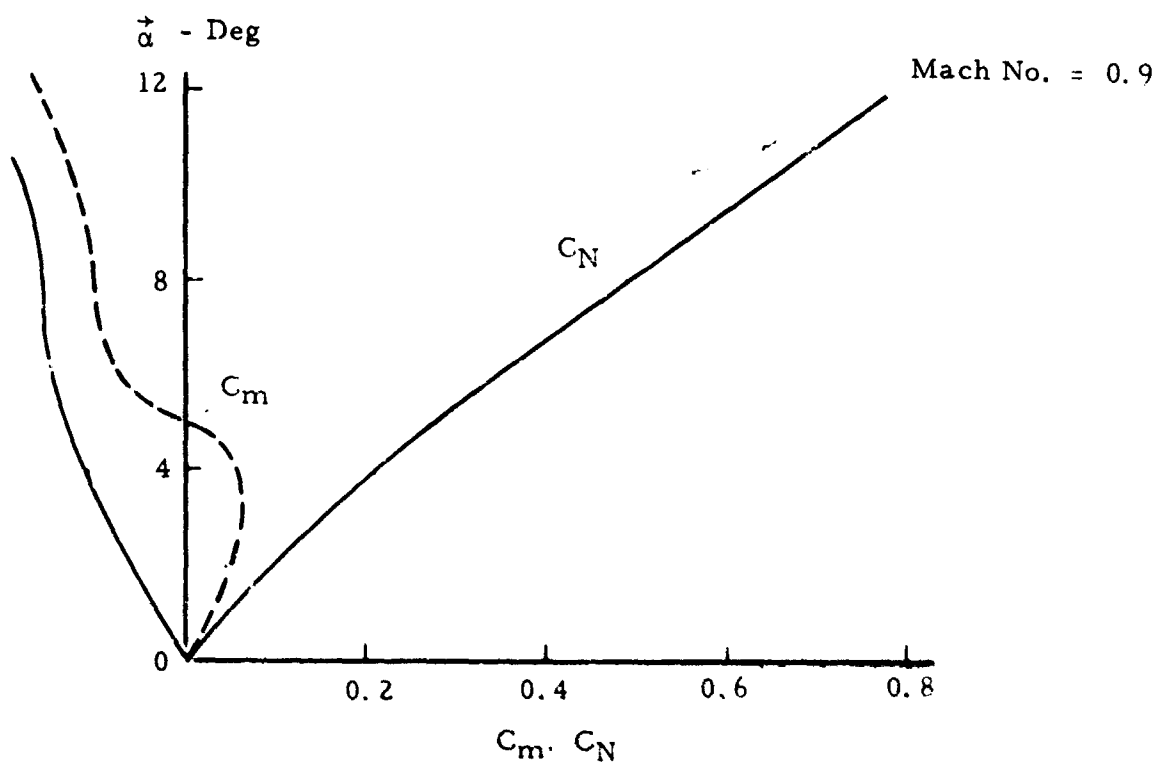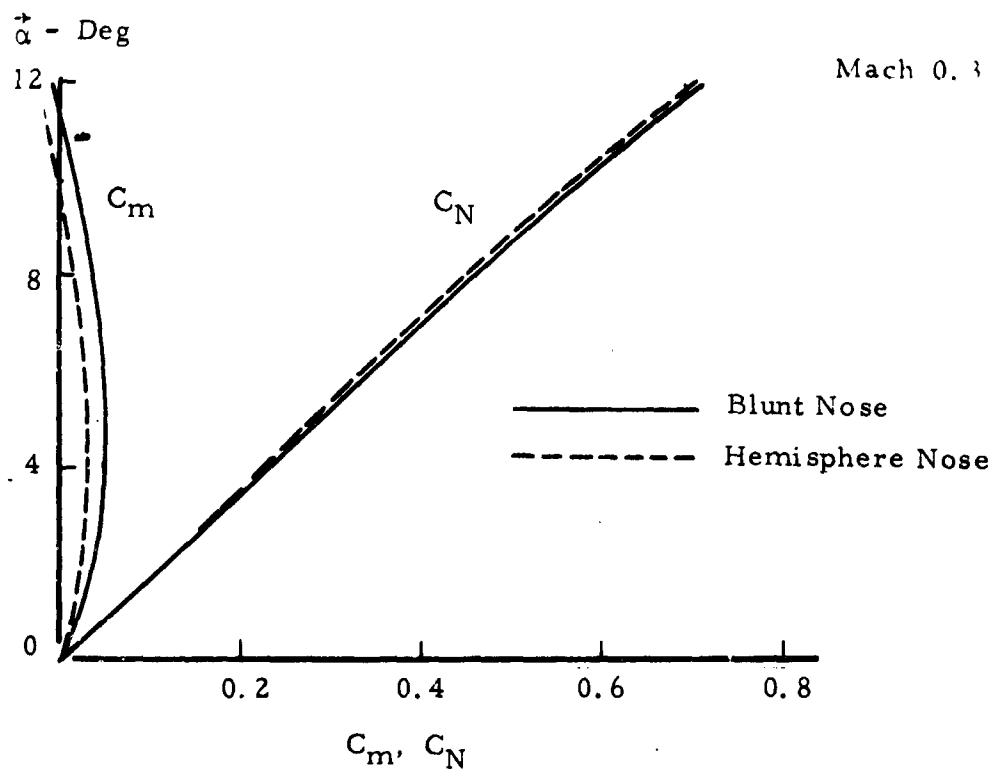
Figure 3. Restoring Moment and Normal Force Characteristics of Basic S-Curve Bomblet Configuration

9
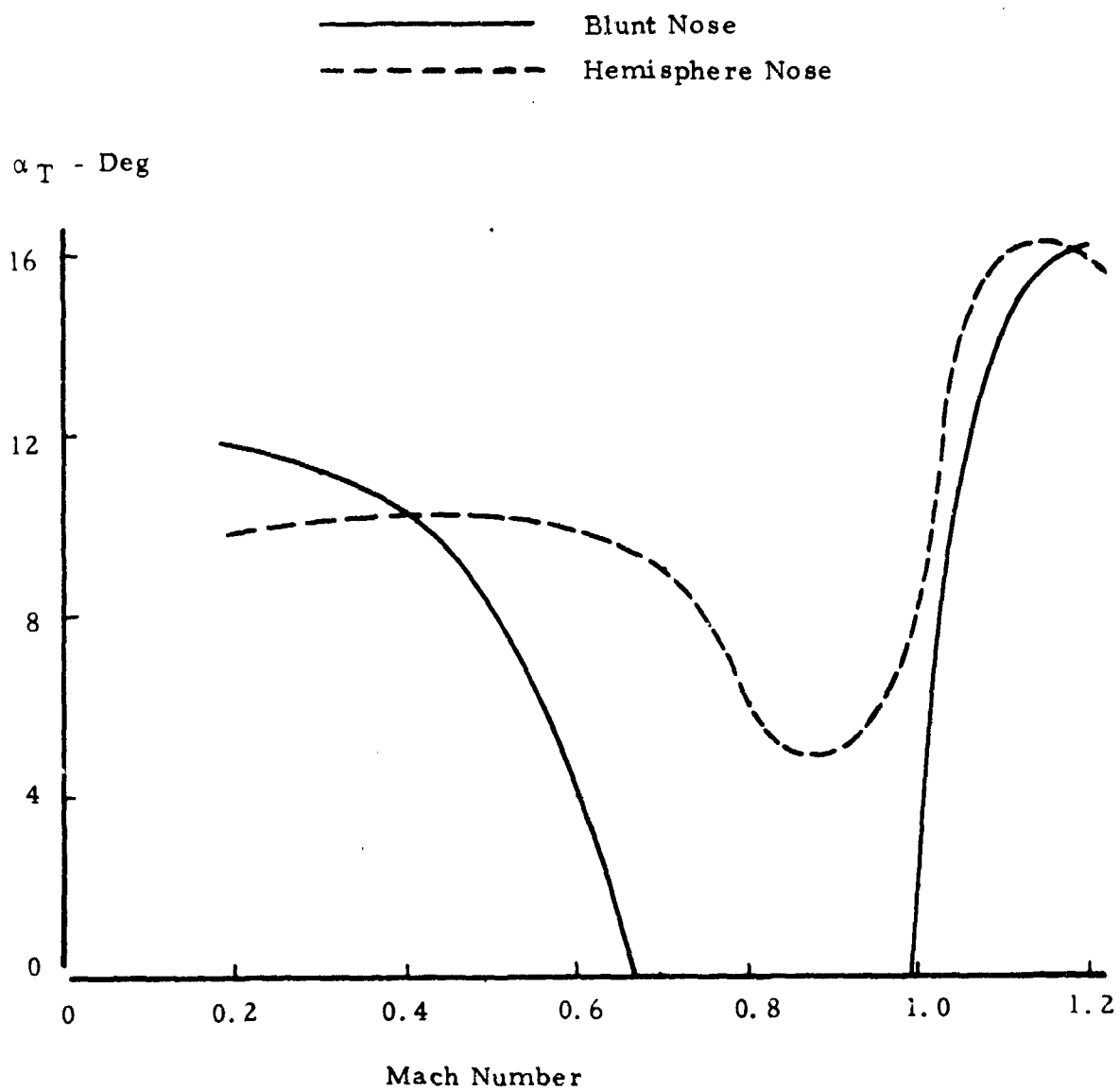
Figure 4. Variation of Trim Angle of Attack with Mach Number
for Basic S-Curve Bomblet Configuration

10

Table I summarizes the aeroballistic coefficients used for the six-degrees-of-freedom motion simulations. The coefficient notation is described in Appendix I. The rolling moment coefficient is tabulated for a fin cant angle of 0.1 degree. The aerodynamic coefficients are independent of the aerodynamic roll angle for the angle of attack range of interest.

5. Motion Simulations.

The motion, trajectory, and impact pattern characteristics of the S-curve type bomblet have been extensively investigated using the six-degrees-of-freedom (6-DOF) trajectory program,[3] and the previously described aerodynamic and physical characteristics data.

The 6-DOF motion simulations describe both the transient and steady-state dispersion characteristics, neither of which is predictable by the "zero coning" theory. In addition, the exact motion solutions have been used to determine the bomblet response to various initial flight conditions, disturbances, and configurational asymmetries.

The initial conditions used for motion simulation purposes are determined by the attitude and motion of the dispenser at time of functioning, and by the positioning of the bomblets within the dispenser. Some of the configurational asymmetries which must be considered are fin cant, longitudinal misalignment (C_{m_o} and C_{n_o}), and lateral center-of-gravity offset.

The initial attitude of the bomblets with respect to the dispenser flight path critically affects the motion simulations, both from the standpoint of the bomblet dynamics and the determination of an impact pattern. The bomblet impact pattern is most easily determined if each bomblet is assumed to be randomly oriented in a nose outward attitude at a fixed angle with respect to the dispenser centerline. Assuming that the dispenser is aligned with its flight path, the initial angle of attack of each bomblet will be constant, and the orientation of the angle of attack plane with respect to a vertical or horizontal reference will vary randomly from $0 \rightarrow 2\pi$. In most instances, the bomblet pitching response is sufficiently rapid that the angle between the bomblet axis and the dispenser axis (initial angle of attack) can be somewhat less than the bomblet trim angle of attack.

If the bomblet axis is initially aligned with the dispenser axis, both the angle of attack and pitching moment will be zero, and the bomblet will not pitch nose-out to the trim angle of attack unless disturbed. The disturbance can be produced by the motion of the dispenser or by the bomblet asymmetries. A simplified simulation of the zero angle of attack case can be accomplished by the use of a body-fixed pitch asymmetry (i. e. . C_{m_o} moment coefficient). The orientation of the body axes can be assumed to be random, and this, in turn, leads to various bomblet flight paths and ultimately to a dispersion pattern at ground impact.

11

TABLE I.   AERODYNAMIC DATA SUMMARY: BASIC BLUNT-NOSE S-CURVE BOMBLET

AEROBALLISTIC COEFFICIENTS

Coefficient	Mach Number	α ~ Degrees											
		0	2	4	6	8	10	12	16	20	24	30	90
CX	0-0.3	-.189	-.192	-.195	-.202	-.218	-.237	-.256	-.290	-.286	-.328	-.33	0
	0.5	-.220	-.238	-.251	-.279	-.309	-.337	-.366	-.406	-.440	-.482	-.48	0
	0.7	-.349	-.346	-.358	-.376	-.402	-.430	-.459	-.508	-.556	-.581	-.58	0
	0.9	-.487	-.493	-.518	-.547	-.578	-.604	-.632	-.664	-.687	-.718	-.72	0
CN	0-0.3	0	.12	.23	.34	.45	.58	.71	1.02	1.37	1.77	2.5	2.5
	0.5	.01	.12	.24	.35	.47	.60	.74	1.06	1.45	1.85	2.6	2.6
	0.7	.01	.12	.24	.35	.47	.60	.76	1.13	1.52	1.95	2.8	2.8
	0.9	.01	.12	.23	.36	.50	.66	.84	1.22	1.65	2.18	3.0	3.0
CM	0-0.3	0	.035	.045	.045	.035	.017	-.012	-.125	-.303	-.539	-.75	-.75
	0.5	0	.030	.040	.035	.018	-.010	-.050	-.178	-.368	-.630	-.85	-.85
	0.7	0	-.015	-.010	-.012	-.030	-.060	-.100	-.230	-.441	-.679	-1.00	-1.00
	0.9	0	-.098	-.135	-.148	-.160	-.192	-.240	-.355	-.525	-.703	-1.00	-1.00
CMQ, CNR	0-0.3	-30.0	-30.0	-30.0	-30.0	-30.0	-30.0	-30.0	-30.0	-30.0	-30.0	-30.0	-30.0
	0.5	-85.0	-85.0	-85.0	-85.0	-85.0	-85.0	-85.0	-85.0	-85.0	-85.0	-85.0	-85.0
	0.7	-100.5	-100.5	-100.5	-100.5	-100.5	-100.5	-100.5	-100.5	-100.5	-100.5	-100.5	-100.5
	0.9	-114.0	-114.0	-114.0	-114.0	-114.0	-114.0	-114.0	-114.0	-114.0	-114.0	-114.0	-114.0
CMPR, CNPQ	0-0.3	0	0	0	0	0	0	0	0	0	0	0	0
	0.5	0	0	0	0	0	0	0	0	0	0	0	0
	0.7	0	0	0	0	0	0	0	0	0	0	0	0
	0.9	0	0	0	0	0	0	0	0	0	0	0	0
CNP	0-0.3	0	.02	.05	.12	.25	.38	.50	.85	1.30	1.82	2.80	2.80
	3.5	0	.02	.05	.12	.25	.38	.50	.85	1.30	1.82	2.80	2.80
	0.7	0	.06	.14	.22	.35	.51	.67	.78	.50	-.15	-1.2	-1.2
	0.9	0	.10	.22	.32	.45	.65	.83	.72	.30	-2.00	-5.2	-5.2
CL×10³	0-0.3	.419	.576	.734	.890	1.014	1.10	1.19	1.40	1.68	1.99	2.44	2.44
	0.5	.419	.576	.734	.890	1.014	1.10	1.19	1.40	1.68	1.99	2.44	2.44
	0.7	.541	.665	.820	.960	1.065	1.15	1.21	1.28	1.19	0.66	0.82	0.82
	0.9	.645	.804	.925	1.030	1.135	1.19	1.24	1.17	0.70	0	0	0
CLP	0-0.3	-.32	-.42	-.53	-.62	-.71	-.77	-.82	-.84	-.77	-.59	0	0
	0.5	-.32	-.42	-.53	-.62	-.71	-.77	-.82	-.84	-.77	-.59	0	0
	0.7	-.44	-.52	-.61	-.69	-.76	-.82	-.85	-.84	-.70	-.20	0	0
	0.9	-.56	-.62	-.69	-.77	-.82	-.86	-.87	-.84	-.64	0	0	0
CMP	0-0.3	0	0	0	-.20	-.50	-1.00	-1.5	-2.4	-3.3	-4.4	-6.0	-6.0
	0.5	0	0	0	-.20	-.50	-1.00	-1.5	-2.4	-3.3	-4.4	-6.0	-6.0
	0.7	0	-.35	-.6	-.93	-1.17	-1.47	-1.63	-1.87	-2.10	-2.4	-2.70	-2.70
	0.9	0	-.65	-1.2	-1.67	-1.83	-1.93	-1.77	-1.33	-0.9	-0.4	.70	.70

12

Both the latter method, and the nose-outward method of initiating the bomblet motion are considered in the present report. In a future effort, a Monte Carlo technique will be used to realistically simulate the bomblet motion for a wide variety of initial conditions and perturbations.

The flight behavior of the S-curve type bomblet is most easily visualized by examination of the angle of attack and spin histories. To this end, the plane of the angle of attack with respect to horizontal will be defined by the angle, $\bar{\Phi}$, as depicted in Appendix I. It will be noted that $\bar{\Phi}$ is the negative complement of $\tilde{\phi}$, which in the zero coning theory is the orientation of the angle of attack plane with respect to vertical.

Motion with Finite Initial Angle of Attack and Varying Fin Cant. Figure 5 illustrates the angle of attack and roll dynamics of the basic blunt-nose bomblet configuration when released from a dispenser at an altitude of 1000 feet and an angle of attack of five degrees, velocity of 600 ft/sec, and flight path angle of 15 degrees. The bomblet is assumed to have a nominal fin cant angle of 0.02 degree, corresponding to positive roll rate. Three different initial orientations of the angle of attack plane are considered: $\bar{\Phi}$ = 0, 90, 180 degrees. The position of the bomblet nose with respect to the dispenser (when looking in the direction of flight) is left, up, and right, respectively.

In this example the spin rate due to the fin cant is less than the critical spin rate as defined by the zero coning theory, and it can be seen that $\bar{\Phi}$ approaches a quasi-steady value in agreement with the theory. The computed theoretical relationship between the angle of attack plane orientation and the roll rate is illustrated in Figure 6 for a Mach number of 0.3. Using the motion data for $\bar{\Phi}_0$ = 90 degrees as an example, the theoretical values of $\bar{\Phi}$ for Mach numbers less than 0.3 were computed and the results shown for comparison in Figure 5. It is seen that the 6-DOF and theoretical solutions for the orientation angle, $\bar{\Phi}$, differ by only a few degrees.

Figure 7 illustrates the effect of a larger fin cant angle (0.1 degree) on the motion histories of $\bar{\Phi}$, $\vec{\alpha}$, and p for the same dispenser event conditions that were considered in Figure 5. The 0.1 degree cant angle drives the roll rate above the critical spin rate, and $\bar{\Phi}$ does not approach a quasi-steady-value. Instead, $\bar{\Phi}$ increases negatively and the bomblet exhibits a counterclockwise coning motion. The coning motion causes the lift vector to rotate, whereas for the 0.02 degree cant angle the lift vector remained upward. As a result, the flight time is shortened. For example, consider the case where $\bar{\Phi}_0$ = 0; the flight time is reduced from 9.96 seconds to 5.6 seconds when the cant angle is increased from 0.02 to 0.1 degree.
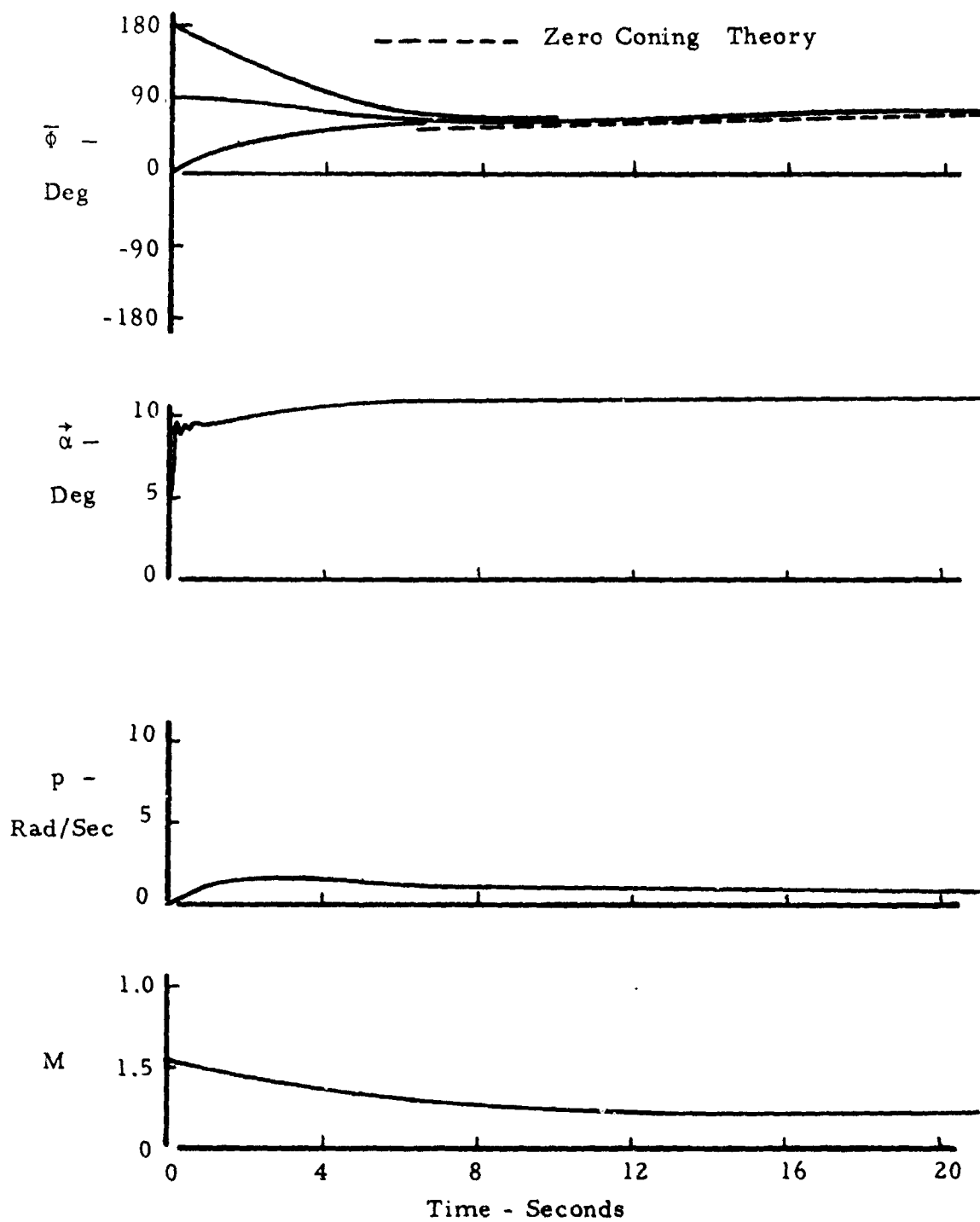
Figure 5.   Motion Histories for Basic Blunt Nose S-Curve Bomblet
with 0.02 Degree Fin Cant and Initial Angle of Attack
of 5.0 Degrees.

Dispenser Opening Conditions: h_o = 1000 ft, V_o = 600 ft/sec,
γ_o = 15 degrees

14

Figure 6.   Relation Between Angle of Attack Plane Orientation and
Roll Rate as Computed from Zero Coning Theory

Basic Blunt-Nose S-Curve Bomblet

15
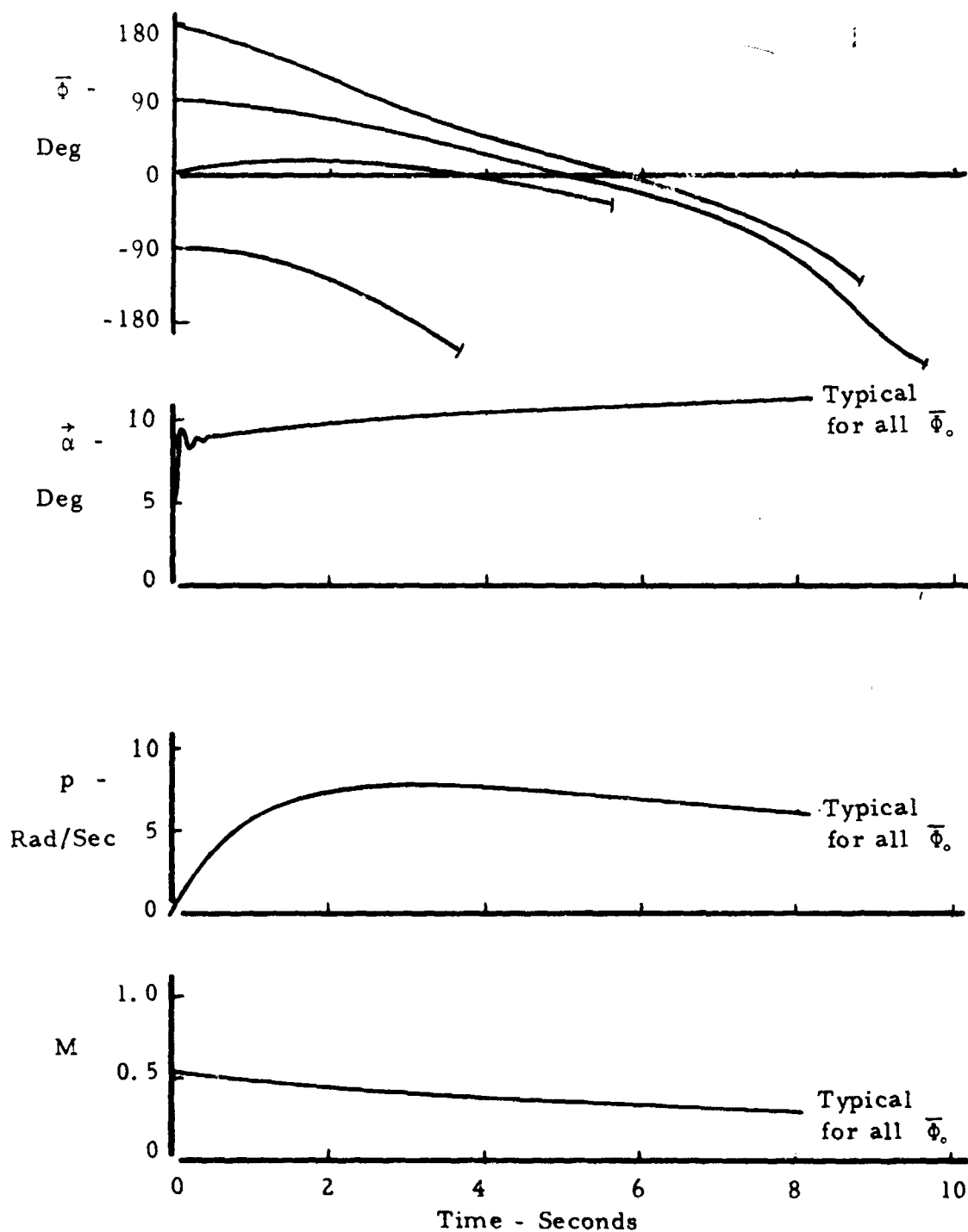
Figure 7. Motion Histories for Basic Blunt Nose S-Curve Bomblet
with 0.1 Degree Fin Cant and Initial Angle of Attack
of 5.0 Degrees

Dispenser Opening Conditions: h_o = 1000 ft, V_o = 600 ft/sec,
$Y_.$ = 15 degrees

16

Effect of Velocity and Mach Number. The deleterious effect
of increasing the cant angle to 0.1 degree is diminished if the initial flight
velocity is reduced. Data computed for a 300 ft/sec dispenser opening
velocity are shown in Figure 8. For $\bar{\phi}_o$ values which are greater than zero,
the angle of attack plane orientation approaches a constant, even though the
spin rate is greater than critical.

With increasing velocity at dispenser opening, the motion of the
basic S-curve type bomblet becomes more critical. For any cant angle, the
peak roll rate tends to increase in direct proportion to the velocity, and thus
there is a greater tendency for the critical spin rate to be exceeded. Another
factor is the effect of Mach number on the aerodynamic characteristics,
particularly the trim angle of attack. For Mach numbers between 0.7 and
about 1.0, the basic blunt-nose configuration is stable at small angles of
attack, thus precluding a trimmed lift in the region. For a 900 ft/sec. dis-
penser opening velocity, the effect of Mach number on the trim angle of
attack is clearly discernible in the motion plots of Figure 9.

The initial angle of attack of five degrees dampens almost
completely in the first 0.1 second of flight, and more than two seconds of
flight elapse before trimmed flight is achieved. The dispersion during the
remainder of the flight is small.

The alternate S-curve bomblet with hemisphere nose has a
finite trim angle of attack through the transonic range. For the 900 ft/sec
dispenser opening velocity, the motion of this bomblet is satisfactory, as
can be seen from the angle of attack data plotted in Figure 10.

Bomblet Release at Zero Angle of Attack. Bomblet release
at zero angle of attack requires a suitable disturbance or moment to initiate
rotation of the bomblet to the trim angle of attack. For the purposes of
analytical simulation, a body-fixed moment coefficient, C_{m_o}, was intro-
duced as a means of initiating the bomblet rotation. By varying the initial
orientation of the y body-fixed axis through an angular range, $0 - 2\pi$,
it was anticipated that an impact dispersion boundary would be produced.

A preliminary investigation was made using a moment coeffi-
cient of 0.001, and it was found that the $\bar{\phi}$ rapidly approached a value of
about $\pi/2$, regardless of the initial value of ϕ. Thus, all of the bomblets
impacted within a small area, even though the dispersion from the zero lift
trajectory was sizeable. This meant that the body-fixed moment was too
small in comparison with the moments tending to cause zero coning.

Next, a value of C_{m_o} equal to 0.02 was selected for investiga-
tion. A typical $\bar{\phi}$ history is presented in Figure 11 for a release velocity
of 600 ft/sec and a fin cant angle of 0.1 degree. In this case, a rapid
clockwise coning motion develops, with no tendency for a decrease in the

Figure 8. Motion Histories for Basic Blunt-Nose S-Curve Bomblet with 0.1 Degree Fin Cant and Initial Angle of Attack of 5.0 Degrees

Dispenser Opening Conditions: h_o = 300 ft, V_o = 300 ft/sec, γ = 5 degrees

18

Figure 9.   Motion Histories for Basic Blunt-Nose S-Curve Bomblet
with 0.1 Degree Fin Cant and Initial Angle of Attack
of 5.0 Degrees

Dispenser Opening Conditions: h_o = 2000 ft, V_o = 900 ft/sec,
Y_o = 45 degrees

Figure 10. Motion Histories for Alternate S-Curve Bomblet with Hemisphere Nose, 0.1 Degree Fin Cant, and Initial Angle of Attack of 5.0 Degrees

Dispenser Opening Conditions: h_0 = 2000 ft, V_0 = 900 ft/sec, γ_0 = 45 degrees

20
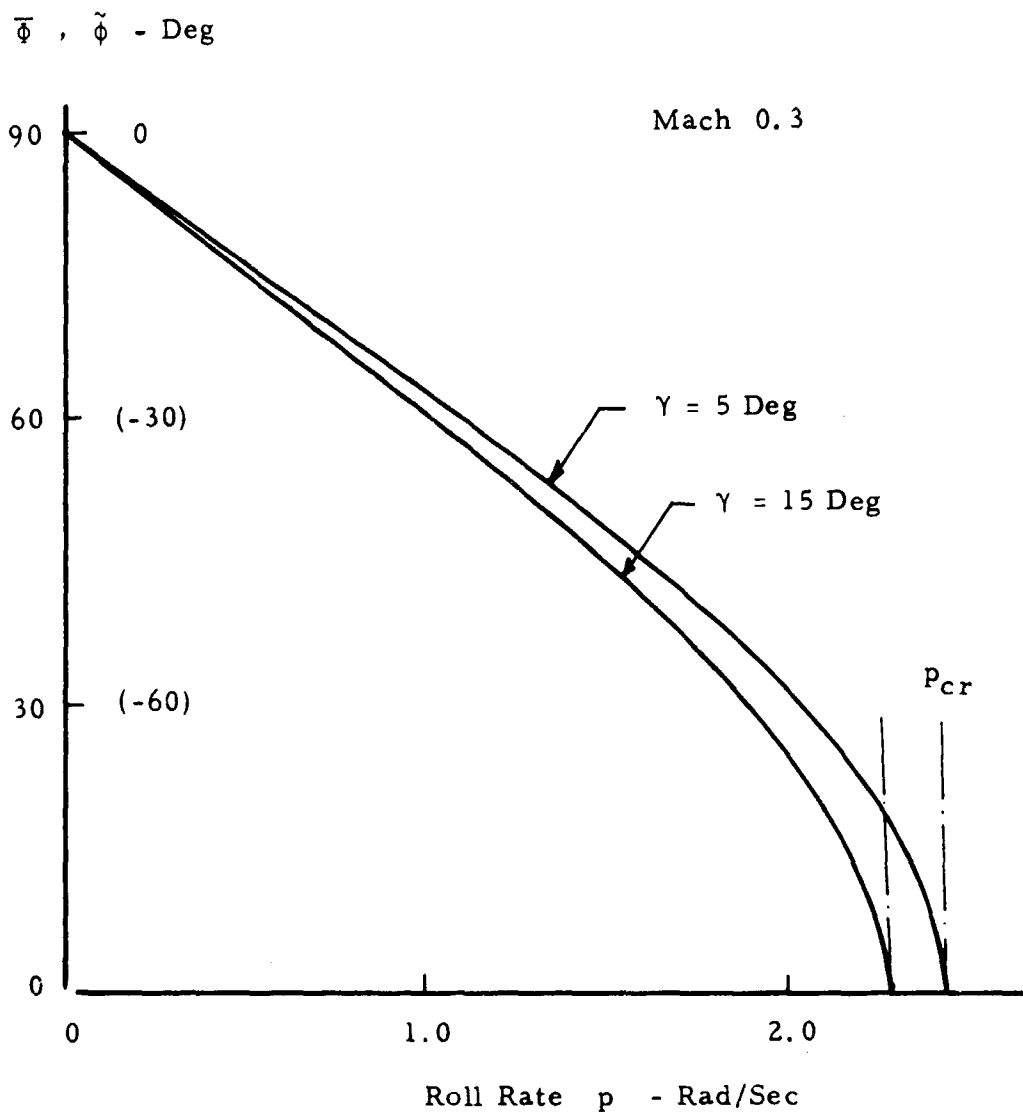
Figure 11.   Motion Histories for Blunt-Nose S-Curve Bomblet
with Zero Angle of Attack Release; $C_{m_O} = 0.02$

Dispenser Opening Conditions: $h_O = 300$ ft, $V_O = 600$ ft/sec,
$Y_o = 5$ degrees

21

rate of change of $\overline{\Phi}$ with time. The coning motion results from the fact that C_{m_0} contributes a magnus-type moment component, as a result of the angle-of-attack plane rotation lagging the rotation of the body axes. Although C_{m_0} is small (i. e., less than the magnitude of the static moment at two degrees angle of attack), it is several times larger than the magnus-moment coefficient evaluated at the trim angle of attack and for a roll rate of the order of 10 rad/sec.

Finally, an intermediate value of C_{m_0}, equal to 0.004, was evaluated for the same dispenser-opening conditions as above. The $\overline{\Phi}$ and $\vec{\alpha}$ histories are presented in Figure 12. The motion is seen to be satisfactory; the angle-of-attack plane orientation is reasonably well separated for each $\overline{\Phi}_0$, and the average variation of $\overline{\Phi}$ with time is only of the order 0.4 rad/sec.

Other Effects. Several types of perturbations were investigated to determine their effect on the bomblet motion and angle-of-attack plane orientation, $\overline{\Phi}$. These perturbations are briefly summarized below.

Perturbation	Magnitude of Perturbation	$\vec{\alpha}_0$	Fin Cant
$\vec{\alpha}$	$\vec{\alpha}_T$	$2\,\vec{\alpha}_T$	0.025 deg
Body-fixed q	2.0 rad/sec	α_T	0.025 deg
Body fixed r	-0.2 rad/sec	α_T	0.025 deg
c. g. lateral offset, Δy	0.0025 ft	α_T	0.025 deg
Lateral misalignment, C_{m_0}	0.004	α_T	0.001 deg
Lateral misalignment, C_{n_0}	0.004	α_T	0.002 deg
Lateral misalignment, C_{r_0}	0.004	α_T	0.003 deg

It was found that the first four perturbations did not significantly affect the rate of change of $\overline{\Phi}$ with time and had only slight effect on the impact dispersion. The effect of lateral misalignment and fin cant on the angle of attack plane orientation, $\overline{\Phi}$, is depicted in Figure 13. The initial $\vec{\Phi}$ was selected such that the misalignment couple was in a plane normal to the angle-of-attack plane. It is seen that the misalignment causes a rapid variation of $\overline{\Phi}$ with time (coning motion) in contrast to the result for zero misalignment. The initial coning motion is independent of the fin cant. After about two seconds, the coning stops and then reverses direction for the larger cant angles; for the smaller cant angle, the coning continues in the initial clockwise direction. The results just described reveal the difficulty of selecting suitable production tolerances for an S-curve type bomblet.
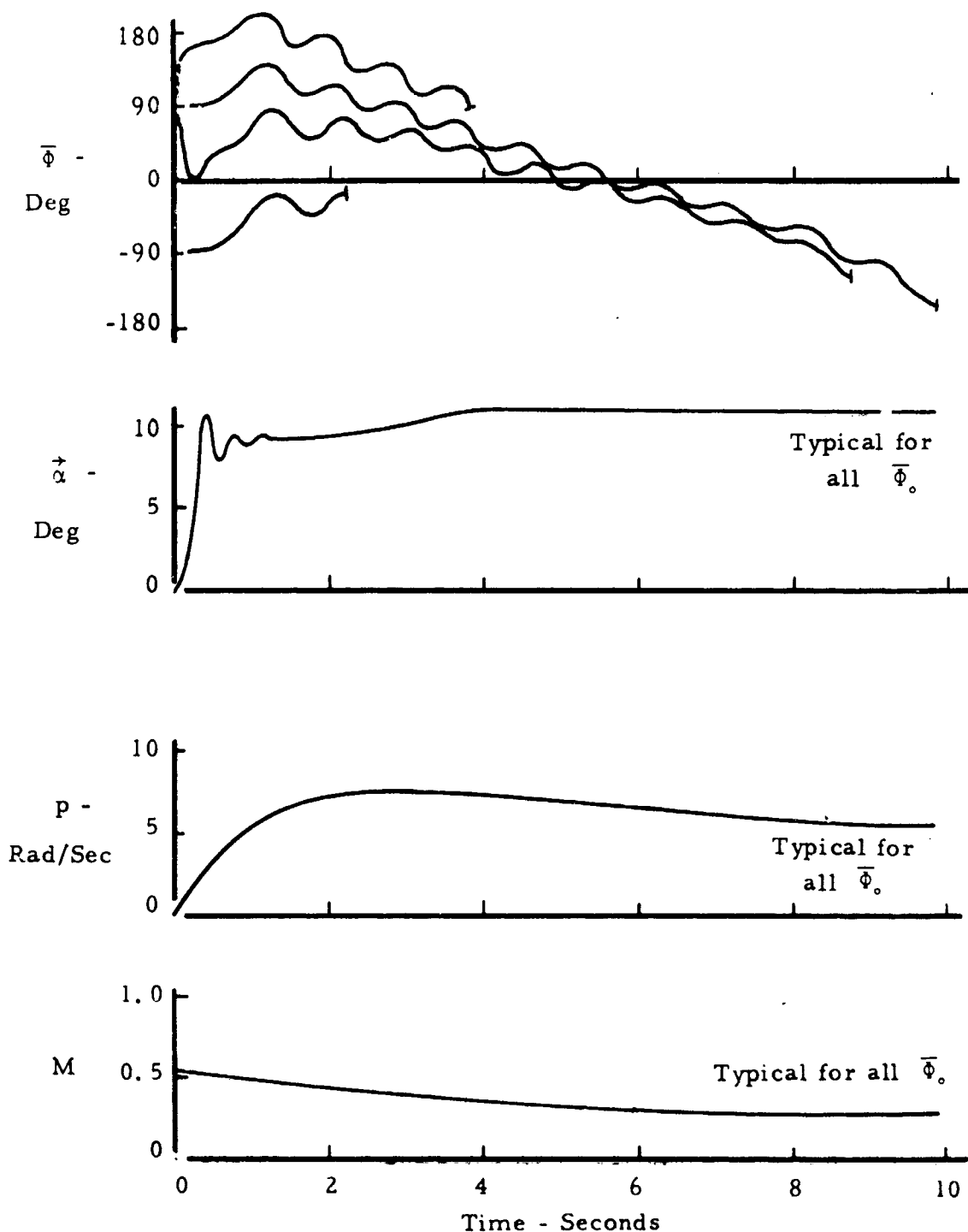
Figure 12. Motion Histories for Blunt-Nose S-Curve Bomblet with Zero Angle of Attack Release; C_{m_0} = 0.004

Dispenser Opening Conditions: h_0 = 300 ft, V_0 = 600 ft/sec, Y_0 = 5 degrees
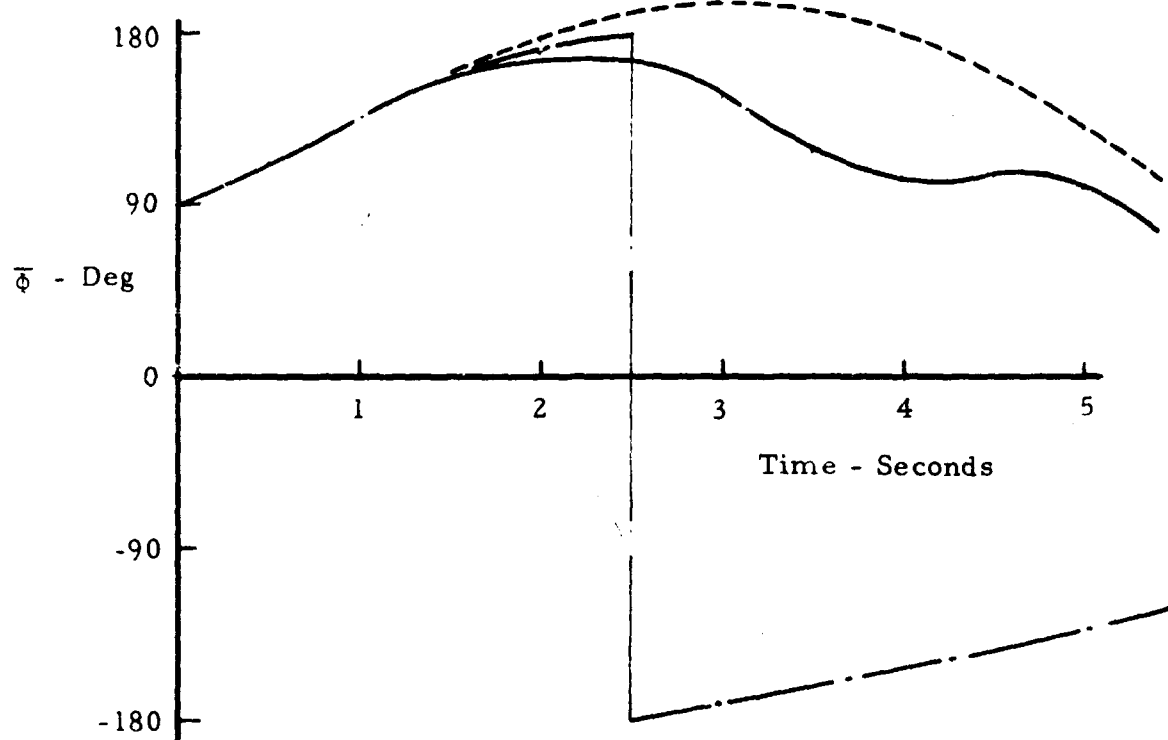
Figure 13.   Effect of Lateral Misalignment and Fin Cant
on Angle-of-Attack Plane Orientation

24

6.   Trajectory and Impact Pattern Characteristics.

        Trajectory and impact pattern data for the S-curve type bomblet
have been evaluated for four standard dispenser opening conditions as out-
lined below:

Standard Dispenser Opening Conditions

Condition	Altitude	Velocity	Mach Number	Flight Path Angle Below Horizontal
I	300 ft	300 ft/sec	0.27	5 deg
II	300 ft	600 ft/sec	0.54	5 deg
III	1000 ft	600 ft/sec	0.54	15 deg
IV	2000 ft	900 ft/sec	0.81	45 deg

The trajectory and impact data were computed using exact six-degrees-of-
freedom motion simulations as previously described.

        The maximum dispersion boundary for each set of initial
conditions and configuration parameters was determined by either varying
the orientation of the initial plane of incidence or the roll orientation of the
body-axes, depending on whether the bomblet was initially at a finite angle
of attack or zero angle of attack, respectively. This procedure approxi-
mates the maximum dispersion boundary but does not provide information
on the probable distribution of bomblets within the pattern. The latter
requires detailed statistical knowledge of bomblet configurational assymme-
tries and motion perturbations at dispenser opening. Consideration of these
factors was beyond the scope of the present program.

        For each dispenser opening condition, the vertical plane tra-
jectory projection, along with the ground impact boundary curve, has been
plotted (Figures 14 through 17). These data are presented for a nominal
fin cant angle of 0.1 degree.

        Comparing Figures 14 and 15 for the 300-foot release altitude,
it is noted that the size of the impact pattern increases greatly when the
dispenser velocity is raised from 300 ft/sec to 600 ft/sec. Increasing the
release altitude to 1000 feet and the flight path angle to 15 degrees (Figure
16) does not appreciably change the pattern size, but the total pattern width
is increased from about 1400 feet to 1600 feet while the pattern length is
reduced to about 2250 feet. For the 900 ft/sec dispenser opening condition
(Figure 17), the dispersion and impact pattern of the blunt-nose bomblet
are seen to be extremely small, due to the bomblet's stable flight
characteristics at small angles of attack in the transonic Mach number

25
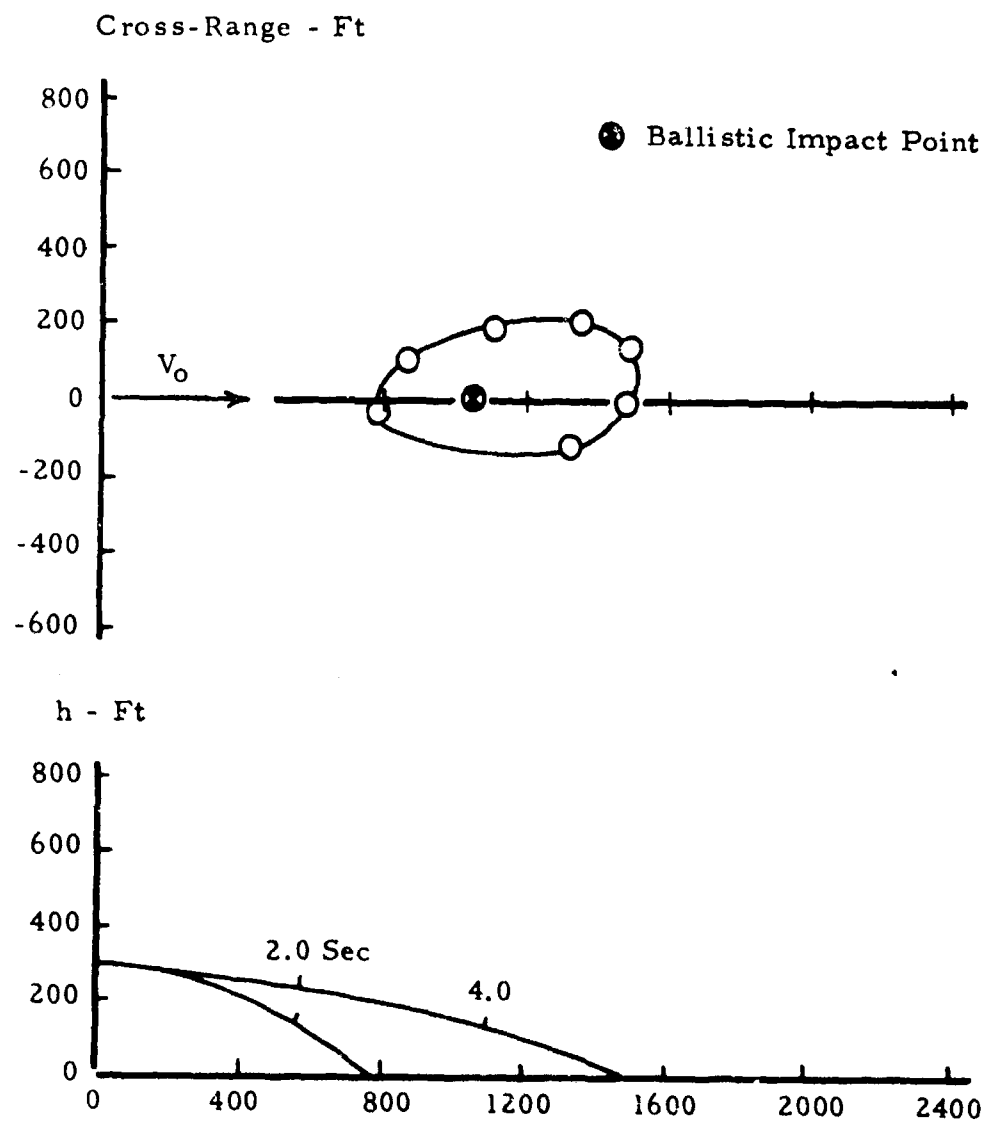
Figure 14. Trajectory and Impact Boundary Data for Blunt-Nose
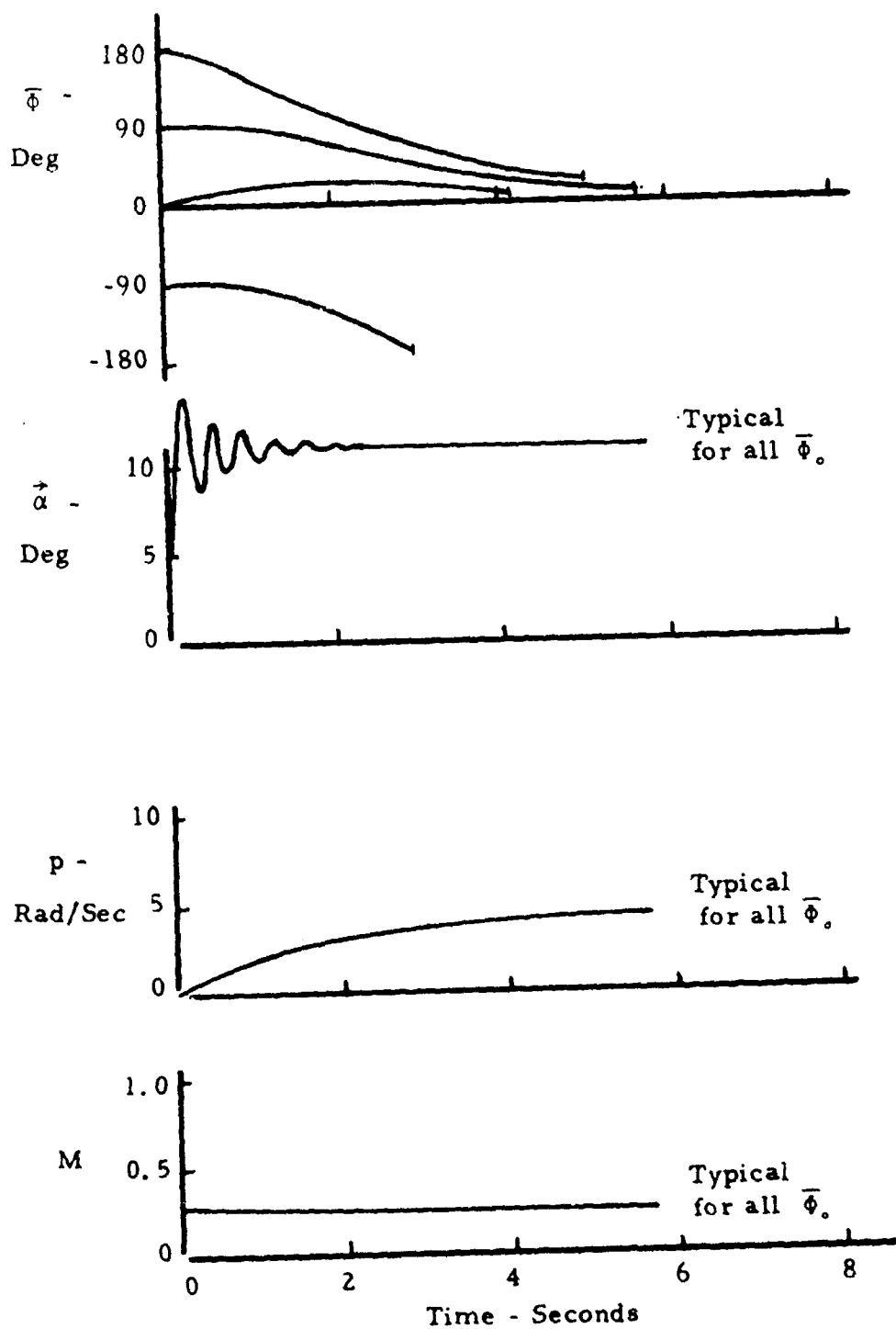S-Curve Bomblet with 0.1 Degree Fin Cant and Initial
Angle of Attack of 5.0 Degrees

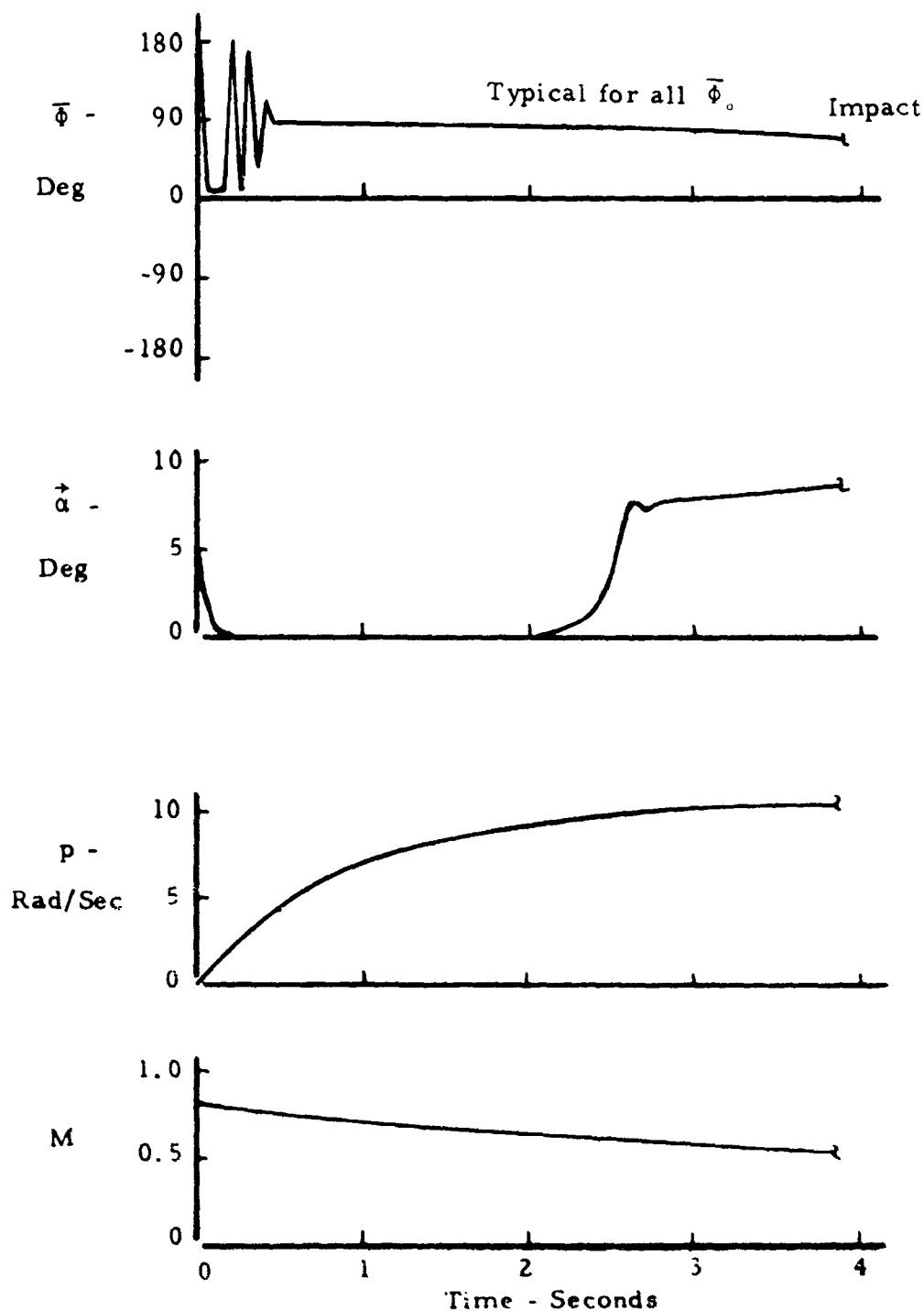Dispenser Opening Conditions: h_o = 300 ft, V_o = 300 ft/sec,
Y_o = 5 degrees
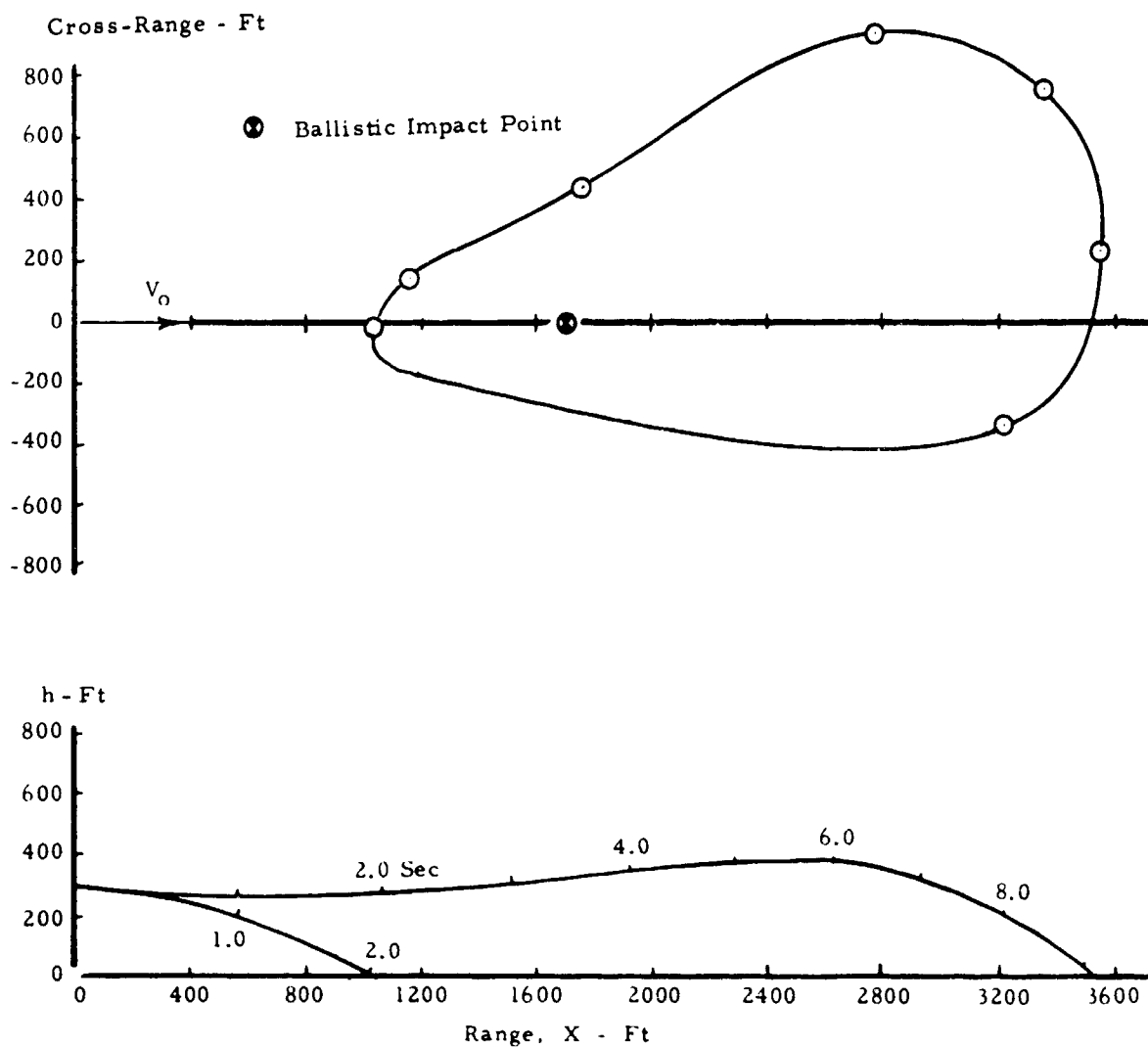
Figure 15. Trajectory and Impact Boundary Data for Blunt-Nose
S-Curve Bomblet with 0.1 Degree Fin Cant and Initial
Angle of Attack of 5.0 Degrees

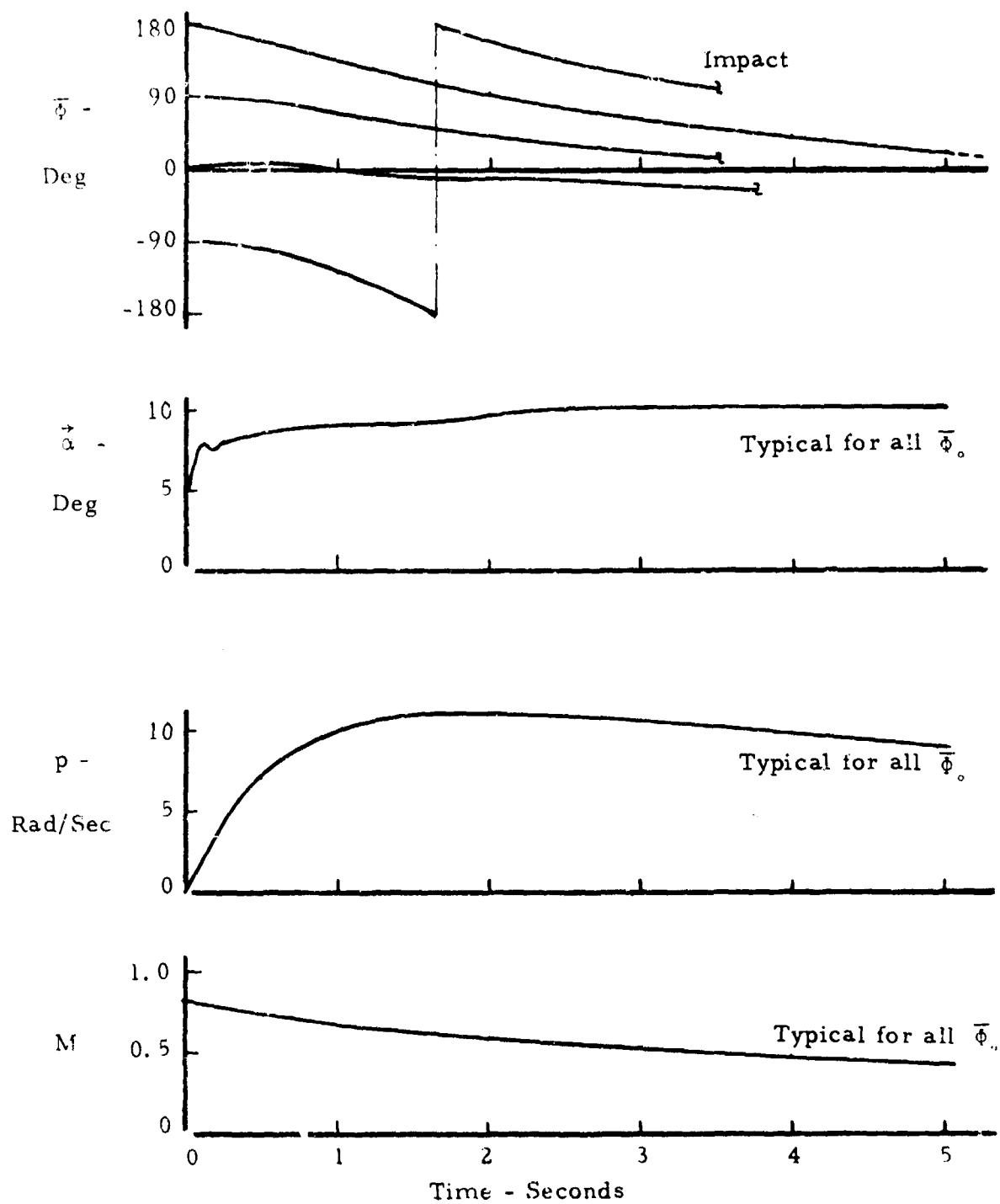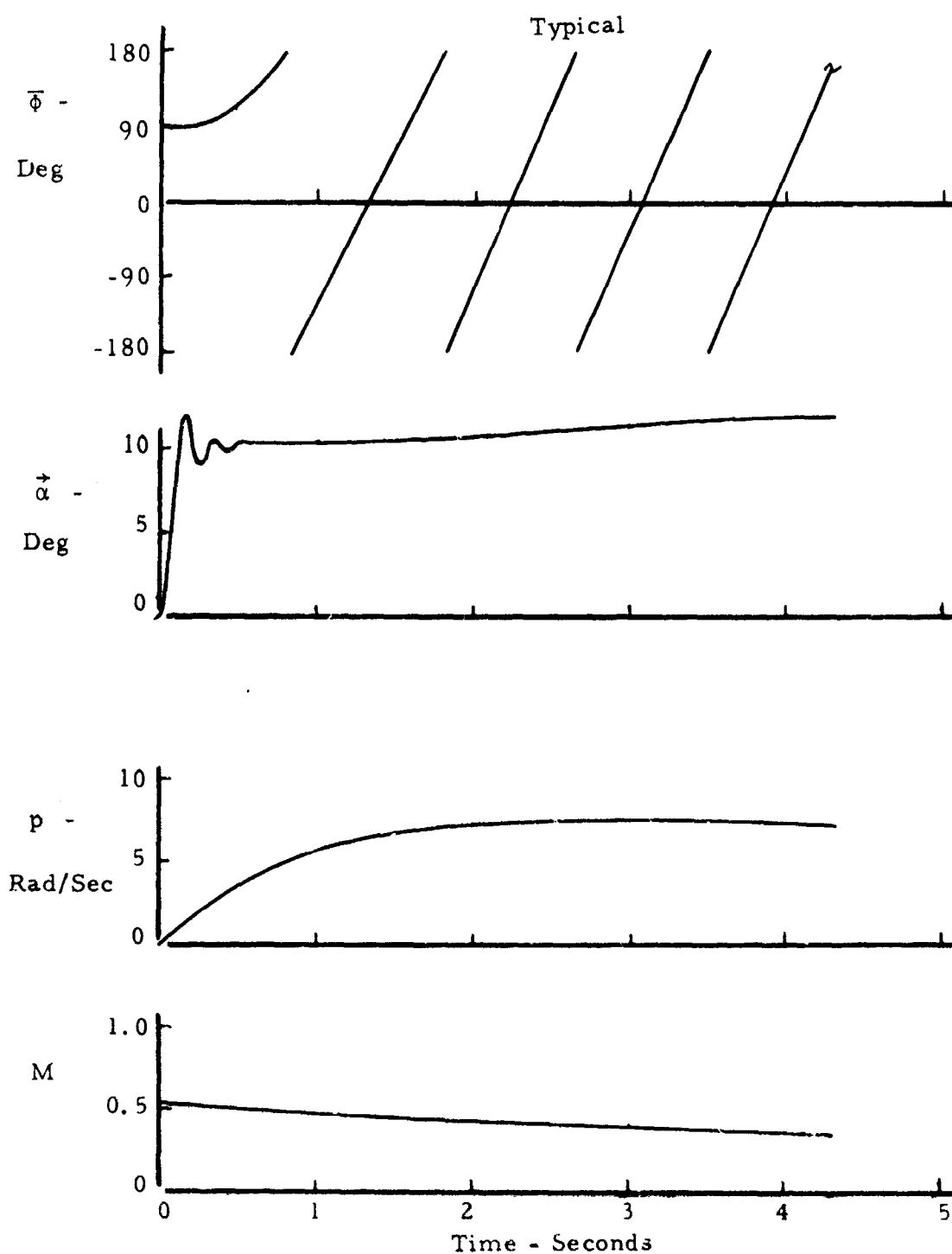Dispenser Opening Conditions: h_o = 300 ft, V_o = 600 ft/sec,
γ_o = 5 degrees

27
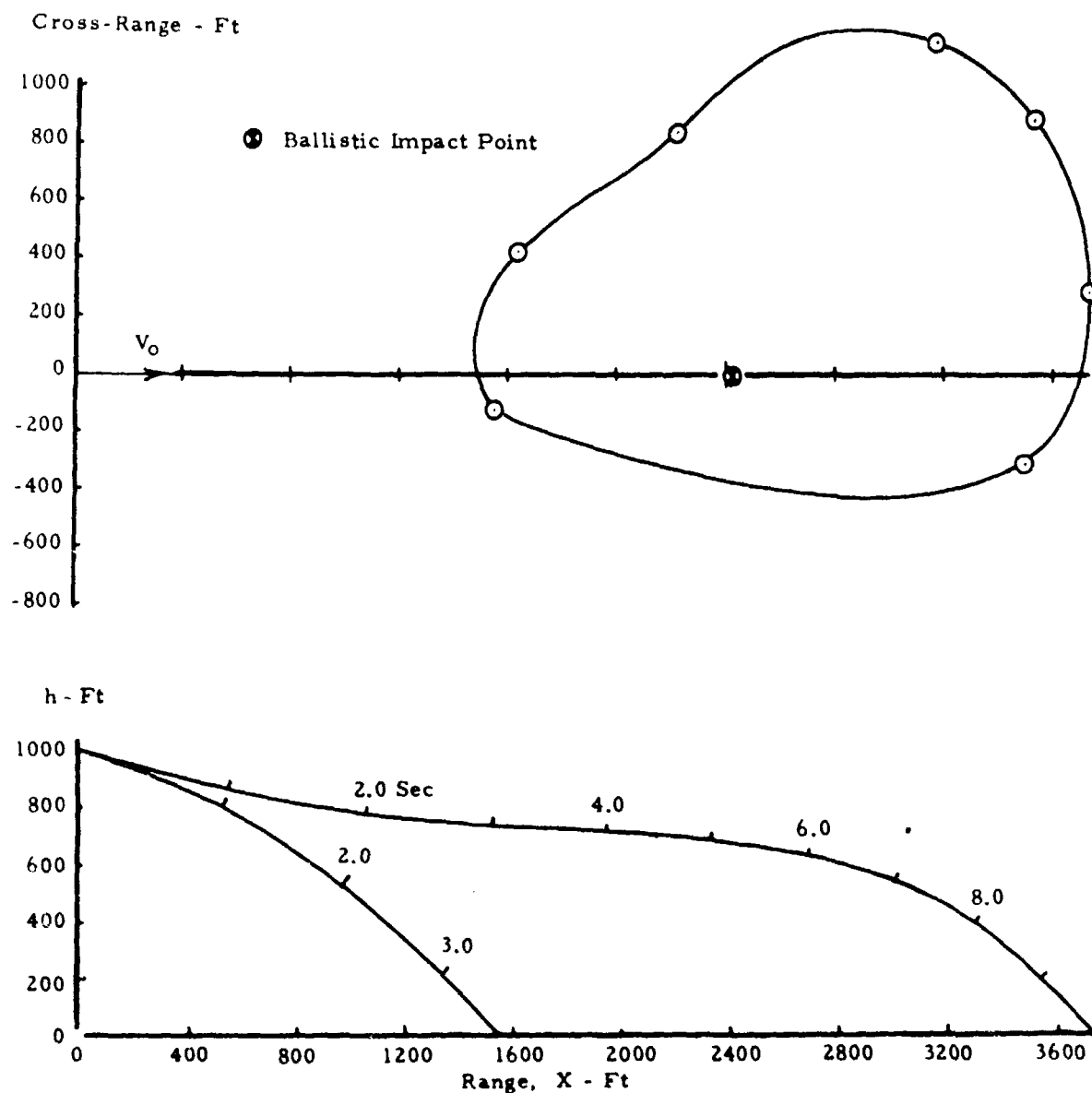
Figure 16.   Trajectory and Impact Boundary Data for Blunt-Nose
S-Curve Bomblet with 0.1 Degree Fin Cant and Initial
Angle of Attack of 5.0 Degrees

Dispenser Opening Conditions: h_o = 1000 ft.
V_o = 600 ft/sec, γ_o = 15 degrees

28
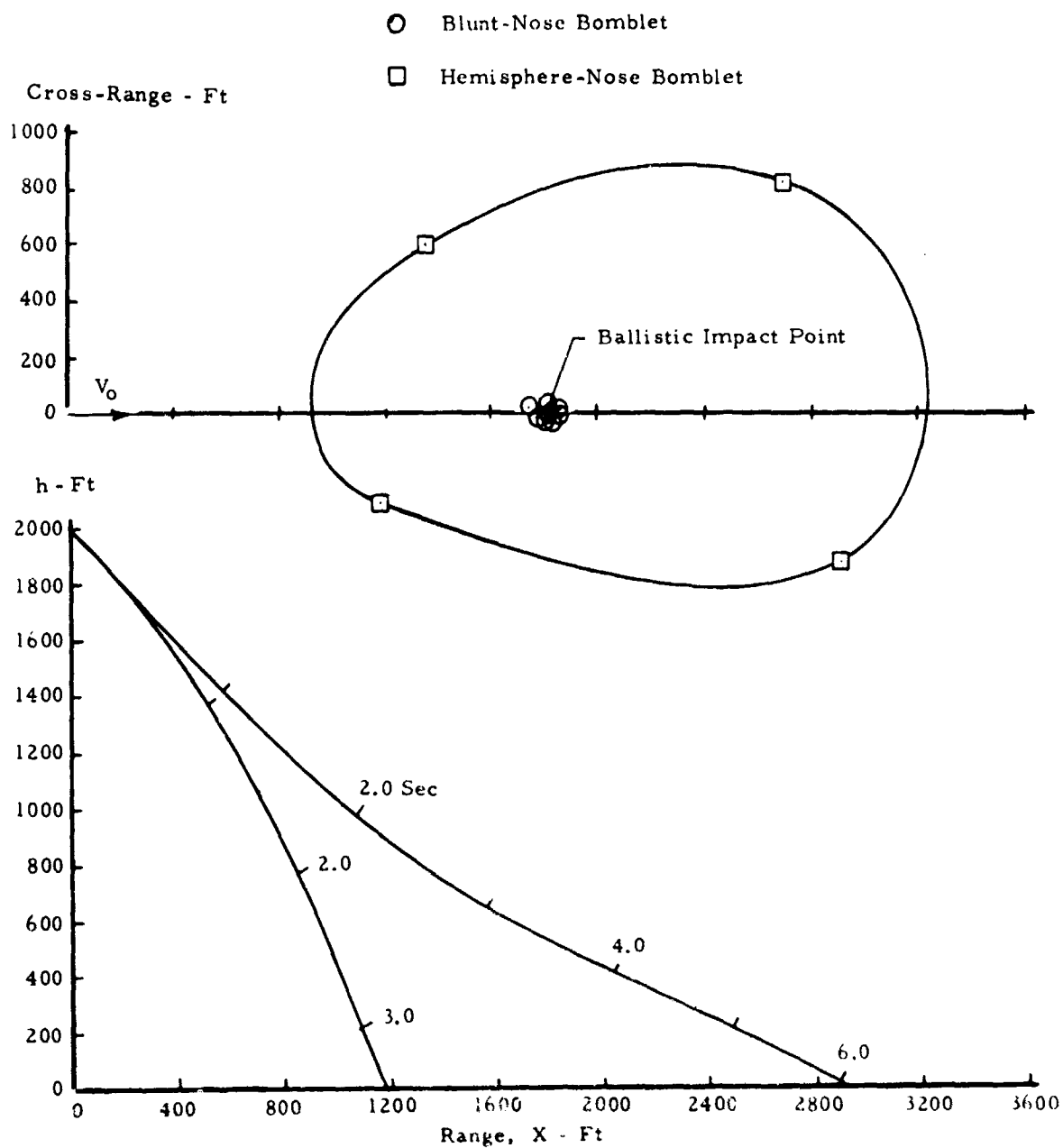
Figure 17. Trajectory and Impact Boundary Data for Blunt-Nose and
Hemisphere-Nose S-Curve Bomblets with 0.1 Degree Fin
Cant and Initial Angle of Attack of 5.0 Degrees

Dispenser Opening Conditions: h_o = 2000 ft.
V_o = 900 ft/sec, γ = 45 degrees

29

regime. The alternate hemisphere-nose bomblet, however, has a large dispersion pattern because the trim angle of attack is about 5.0 degrees at the release Mach number. The pattern size, at 900 ft/sec dispenser opening velocity, is about the same as at the 600 ft/sec dispenser opening conditions. The lack of pattern growth with increase in velocity from 600 ft/sec to 900 ft/sec is attributed to the increased coning rate at the higher velocity, as discussed previously.

Effect of Fin Cant. The effect of fin cant on the trajectory and dispersion data is depicted in Figures 18 and 19 for dispenser opening conditions II and III, respectively. For the shallow low-altitude delivery at 600 ft/sec (Figure 18), it is seen that the impact pattern boundary significantly decreases if the fin cant angle is raised to 0.5 degree. In contrast, the pattern boundary greatly expands when the fin cant angle is reduced to 0.02 degrees, and a pattern width in excess of 3000 feet is obtained. In the latter case, the spin rate is always less than the critical spin; therefore, the pattern size is the maximum achievable.

Similar results are obtained for the small fin cant angle at the 1000-foot bomblet release altitude, dispenser opening condition III.

An interesting aspect of the S-curve bomblet performance, is the extent of the increase in flight range when the spin rate is sub-critical. The horizontal distance to impact is three and two and one-half times that of the zero-lift trajectories, for dispenser opening conditions II and III, respectively.

Release at Zero Angle of Attack. The difficulty of simulating the S-curve bomblet dynamics when the bomblet angle of attack is initially zero has been previously described. For zero angle of attack release, the dispersion is critically dependent on the body-fixed moment coefficients C_{m_0} and C_{n_0}, as well as the fin cant.

The effect of C_{m_0} on the dispersion pattern is depicted in Figure 20 for dispenser opening condition II. A misalignment which produces a C_{m_0} of 0.02 is seen to result in a small size impact pattern, compared to the pattern boundary obtained for a 5.0-degree initial angle of attack. However, a smaller value of C_{m_0}, equal to 0.004, results in a pattern size slightly larger than that obtained with 5.0 degrees initial angle of attack.
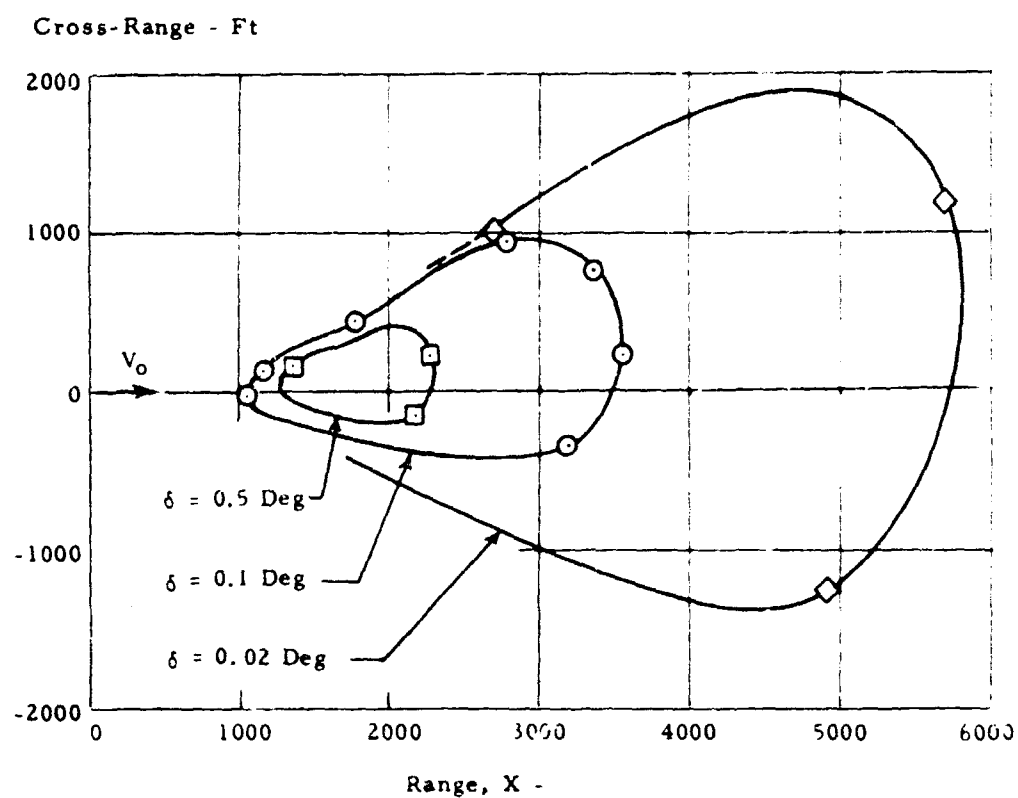
Figure 18.   Effect of Fin Cant on Impact Boundary for Blunt-Nose
             S-Curve Bomblet with Initial Angle of Attack of 5.0
             Degrees

             Dispenser Opening Conditions: h_o = 300 ft,
             V_o = 600 ft/sec, γ_o = 5 degrees

31

Cross Range - Ft

Range, X - Ft
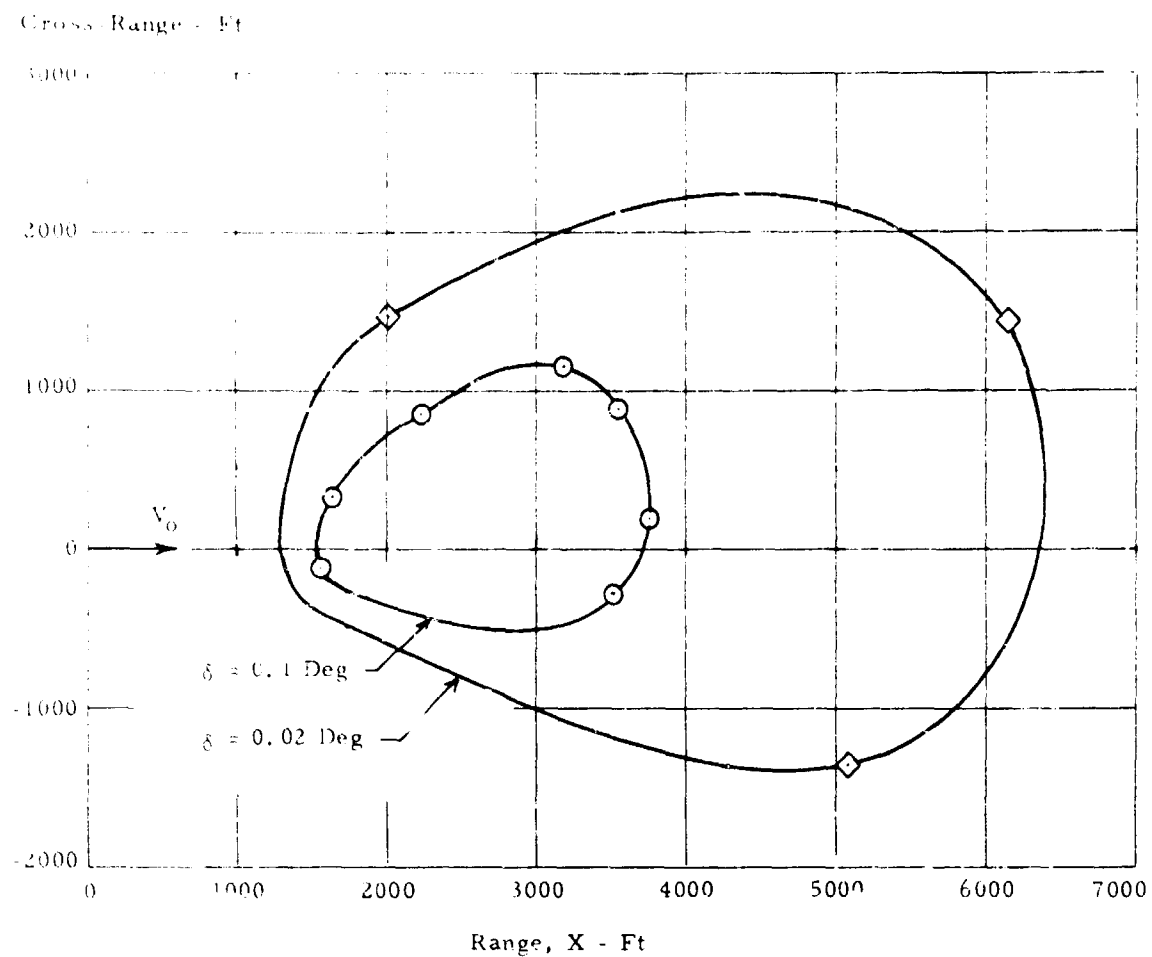
Figure 19.   Effect of Fin Cant on Impact Boundary for Blunt-Nose
S-Curve Bomblet with Initial Angle of Attack of 5.0
Degrees.

Dispenser Opening Conditions: h_o = 1000 ft,
V_o = 600 ft/sec, γ_o = 15 degrees

32

Cross-Range - Ft
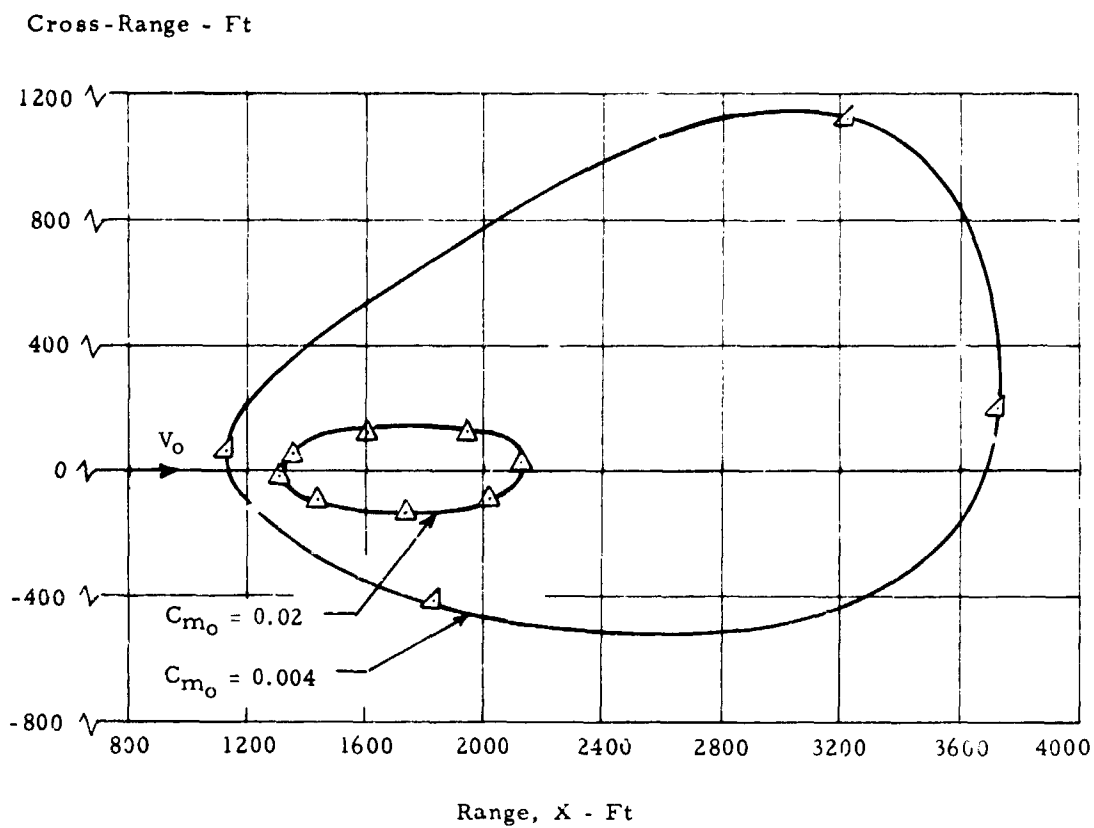
Figure 20. Effect of Release Angle of Attack and Misalignment
Moment on the Impact Boundary of the Blunt-Nose
S-Curve Bomblet with 0.1 Degrees Fin Cant

Dispenser Opening Conditions: h_o = 300 ft,
V_o = 600 ft/sec, $\dot{\gamma}_o$ = 5 degrees

33

B. ROLL-THROUGH-ZERO BOMBLET

1. Description of Concept.

A body-fixed trim incidence or lift force does not generally lead to large dispersion of ballistic bodies, since there is usually sufficient rolling motion from intentional or accidental asymmetries to cause the direction of the lateral force to vary continuously. As a result, the flight path has a corkscrew appearance and the deflection from the zero-lift trajectory is small. An exception to the above is the case where the body rolls through zero angular velocity. In this instance, there is a period where large dispersion can occur in a particular lateral direction.

The roll-through-zero (RT0) bomblet is comprised of a lifting-body configuration equipped with a roll-producing device which will cause the bomblet to spin in a direction opposite to that of the dispenser from which it is released.

2. Theory.

A simplified dispersion theory for the roll-through-zero type bomblet has been developed (Appendix III). which considers the roll and lateral translation degrees of freedom in an approximate manner. It is found that the deflection of the trajectory from the point at which zero roll rate occurs. is closely approximated when there are many subsequent roll cycles by the deflection which occurs during the first $\pi/4$ cycle of roll. If, in addition, several roll cycles occur prior to roll-through-zero, the total deflection of the trajectory is given by Equation (6):

$$\Delta \gamma = \frac{C_N}{2m'} \sqrt{\frac{\pi I_x'}{C_{\ell_\delta} \delta}} \qquad (6)$$

The above expression shows that the deflection of the lifting-body trajectory from the zero-lift trajectory is proportional to the normal force coefficient, as might have been expected. More significant is the fact that the deflection is inversely proportional to the square root of the rolling moment coefficient at zero roll rate, where for a canted-fin bomblet $C_{\ell_0} = C_{\ell_\delta} \delta$. Thus, if roll-through-zero can be made to occur by the use of a very small C_{ℓ_0} or fin cant, a large trajectory deflection can be achieved. Also noteworthy is the fact that the trajectory deflection is independent of the flight velocity.

The amount of dispersion at ground impact can be estimated, if the roll-through-zero period (time required to roll $\pm$ $\pi/4$ cycles from orientation at zero roll rate) is small compared to the total flight time. and

34

if the corresponding zero lift trajectory is closely approximated by a straight flight path, i.e., not affected by gravity. With these assumptions, the ground impact dispersion in the direction of flight, R , and the cross-range dispersion, r , can be expressed as

$$r = \frac{h \ C_N}{2 \ m' \ \sin \gamma} \sqrt{\frac{\pi I_x'}{C_{\ell_\delta} \ \delta}} \tag{7}$$

$$\frac{h \ C_N}{2m' \ \sin^2 \gamma} \sqrt{\frac{\pi I_x'}{C_{\ell_\delta} \ \delta}} \tag{8}$$

3.   Configurations.

The RTO bomblet configuration must basically provide for a trimmed lift, a predictable roll direction, and a minimum design roll torque. The principal problem in bomblet aerodynamic design, is the achievement of large trimmed lift without introduction of spurious roll moments, which can overpower the design roll torque.

On the basis of the above, it was decided that the bomblet body should have a fineness ratio of about six, both for good lift characteristics and to provide an adequate moment arm for the stabilizing fins. A boattail afterbody was considered desirable for the purpose of decreasing the overall fin size and the space required for bomblet packaging. As a means of reducing the induced roll, two design approaches were originally considered: (1) utilization of a ring-tail stabilizer, which would be relatively insensitive to roll, and (2) employment of wing incidence or body-nose cant, thereby permitting the body to trim at a small angle of attack. After some consideration of the problems associated with manufacturing, packaging, and aerodynamic testing, it was decided to delete the ring-tail and canted-nose body configurations from further consideration during the present effort.

The basic RTO configuration which evolved is shown in Figure 21. The cruciform fins of the basic RTO configuration have a thick wedge section for the purpose of increasing the fin effectiveness at transonic Mach numbers and to add drag. The fin tip section is modified to improve packaging. The low aspect ratio wing provides added lift and can also be used to produce the design rolling moment. The basic RTO bomblet can also be utilized without the wing surfaces, in which case fin tabs or fin incidence would be used for roll control and longitudinal trim.

The basic RTO configuration was scaled to a 3-inch diameter prototype size, and the bomblet was assumed to weigh 3.2 pounds. The size

35

Configuration Nomenclature

Body: BR1
Wing: WR1
Cruciform Fins: FR2

Roll Tabs
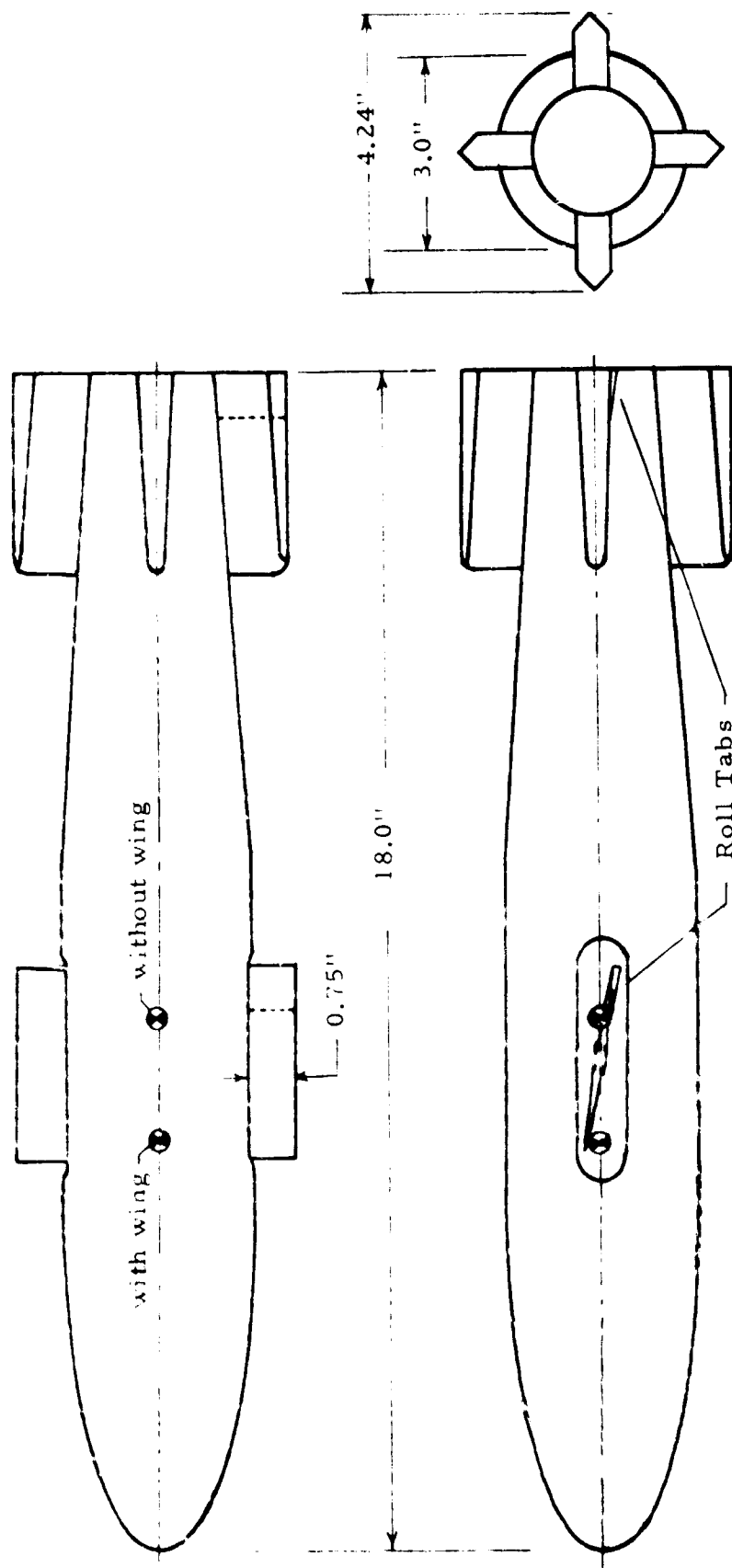
Physical Data

Weight = 3.2 pounds

I_x = 0.0008 slug-ft^2

I = 0.00875 slug-ft^2

Figure 21. Basic Roll-Through-Zero Bomblet Physical Characteristics

and inertia properties of the basic RT0 bomblet configuration are comparable to the Australian S-curve bomblet [1].

During the course of the analytical investigations, it became apparent that a bomblet geometry similar to the basic S-curve bomblet configuration might also be considered. The S-curve bomblet shape has the advantage of a small induced roll moment, even though the lift curve slope is considerably less than that of the basic RT0 configuration. Consequently, an alternate RT0 configuration (Figure 22) was adopted. The alternate RT0 bomblet was scaled to a 2-inch-diameter prototype size, and the physical characteristics, except for c.g. location, are the same as the blunt-nose S-curve bomblet (Figure 1).

4. Aerodynamic Characteristics.

The subsonic lift and pitching moment characteristics of the basic RT0 bomblet with the wing attached at 10 degrees incidence are shown in Figure 23. These data, as well as all other static aerodynamic data for the RT0 bomblet, were obtained from the wind tunnel tests accomplished at AEDC as part of the present effort. These test data are described in detail in (4). The pitching moment data in Figure 23 are presented for two center-of-gravity locations: the aft location (2.6 calibers from nose) was used for the AEDC wind tunnel data reduction, and the forward location (2.077 calibers aft of the nose) was used for flight simulations. As can be seen, unfavorable wing-tail interference results in a large region of instability for the aft center-of-gravity location. With the forward c.g., the trim angle of attack with 10 degrees wing incidence is 8 degrees, and the corresponding trimmed normal force coefficient is 1.09, which includes the body-fixed zero angle-of-attack lift contribution of the wing.

Figure 24 shows the roll moment, side force, and side moment coefficients of the basic RT0 bomblet with wing at 10 degrees incidence, as a function of the angle of attack and aerodynamic roll angle, ϕ. The induced aerodynamic force and moments are appreciable, even at small angles of attack, largely due to the presence of the wing.

Without the wing, the subsonic lift and pitching moment characteristics of the basic RT0 bomblet are as shown in Figure 25, for a center-of-gravity location 2.7 calibers aft of the bomblet nose. In this configuration, a body-fixed moment coefficient of 0.205 is required for trim at 8 degrees angle of attack. This moment can be obtained with fin incidence or fin tabs. The subsonic trimmed normal force coefficient is 0.55, which is about one-half the normal force obtained with the winged configuration. The roll moment, side force, and side moment coefficient, as a function of angle of attack and aerodynamic roll angle, are shown in Figure 26. It will be observed that the induced roll moment is reduced to zero at angles of attack
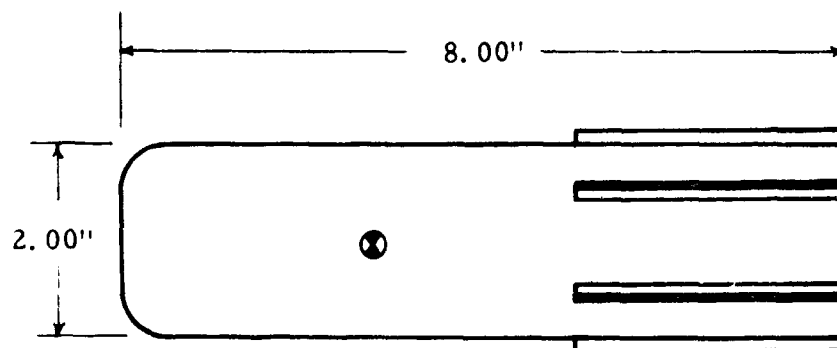
Physical Data

Weight = 1.51 pounds

$I_x = 1.629 \times 10^{-4}$ slug-ft^2

$I = 1.06 \times 10^{-3}$ slug-ft^2

Figure 22. Alternate Roll-Through Zero Bomblet Physical
Characteristics
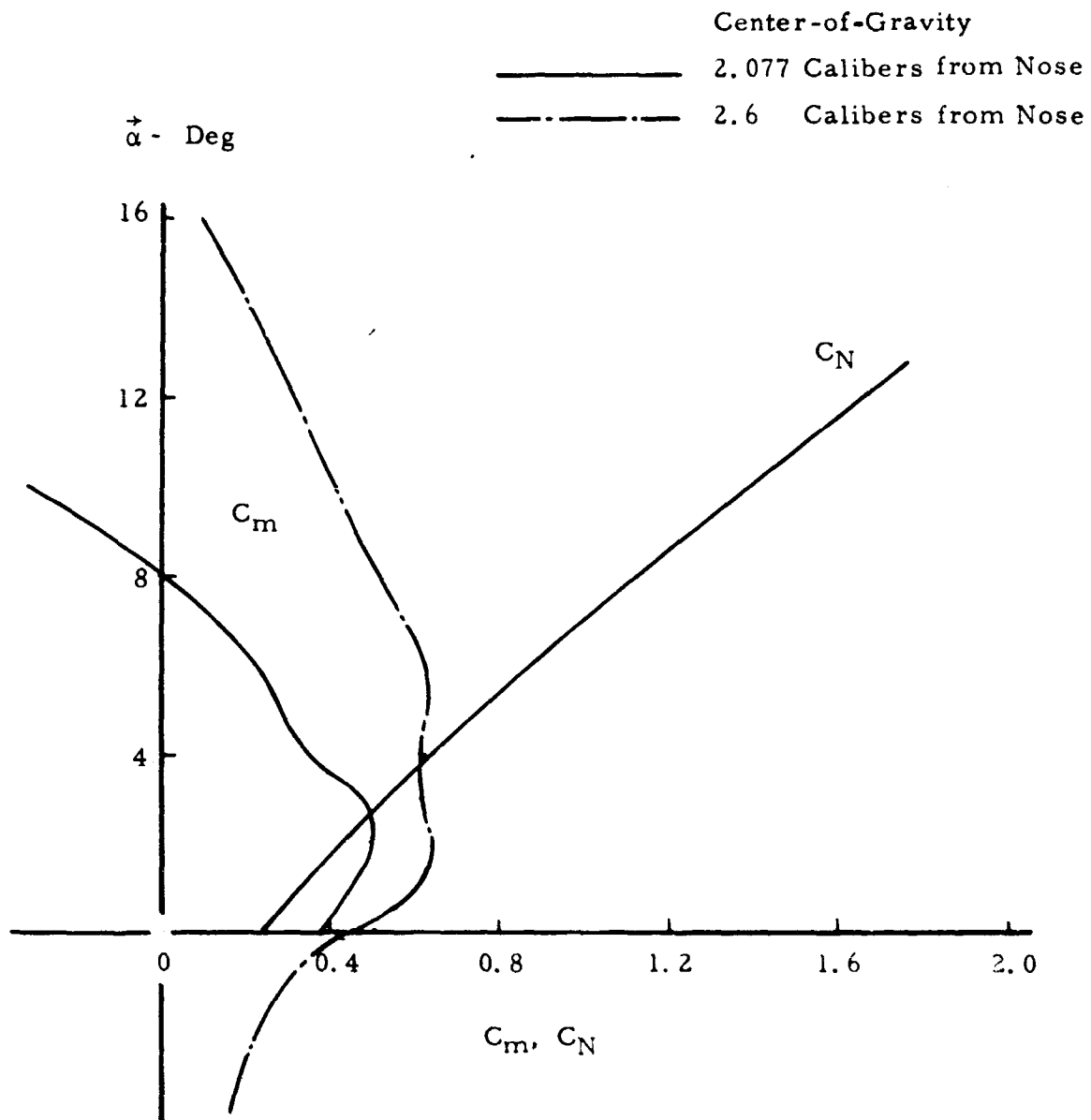
Figure 23.   Subsonic Lift and Pitching Moment Characteristics
of Basic RT0 Bomblet Configuration with Wing at
10 Degrees Incidence
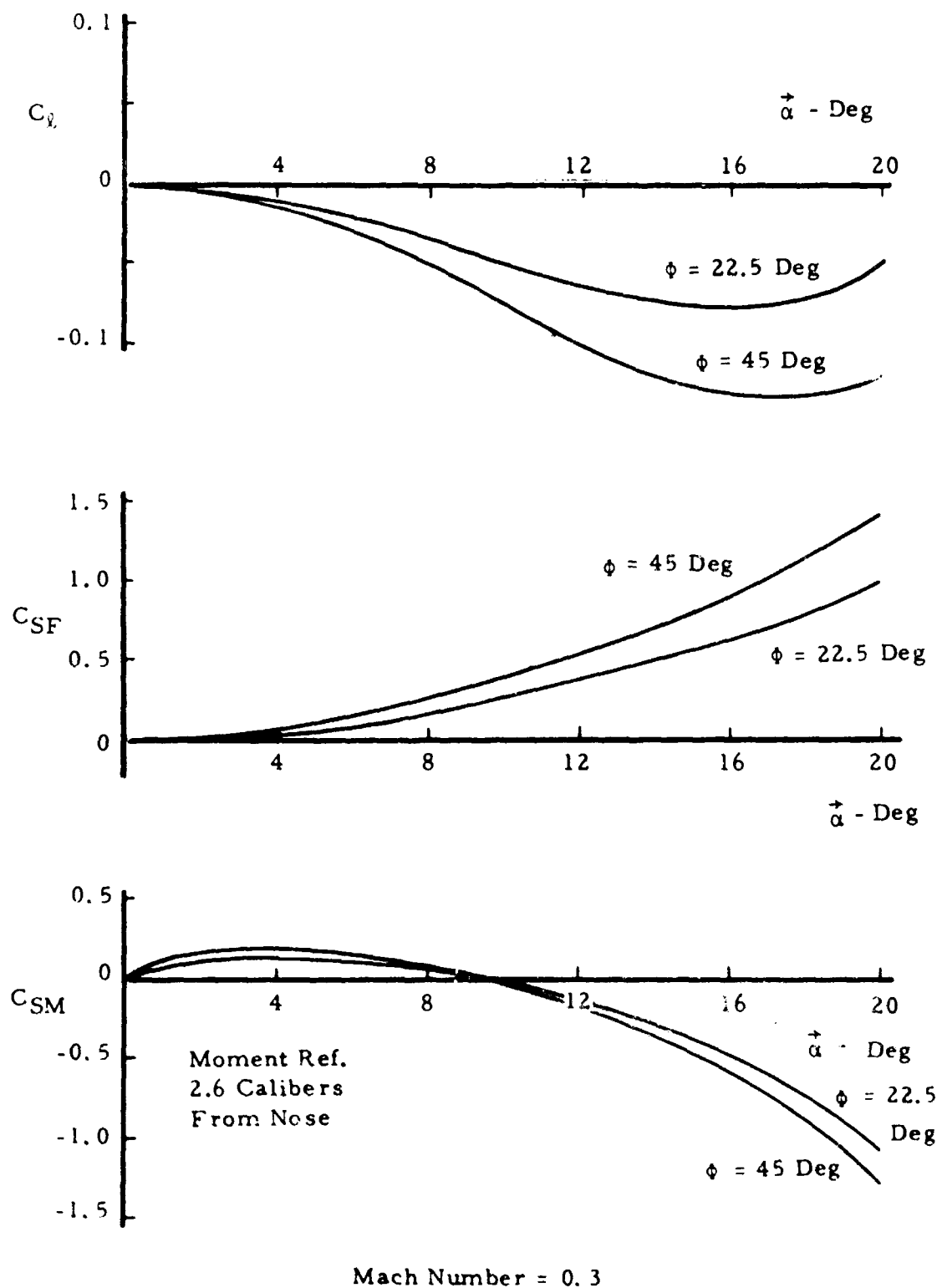
Mach Number = 0. 3

Figure 24.   Roll Moment, Side Force, and Side Moment Characteristics of Basic RTO Bomblet with Wings at 10 Degrees Incidence

40
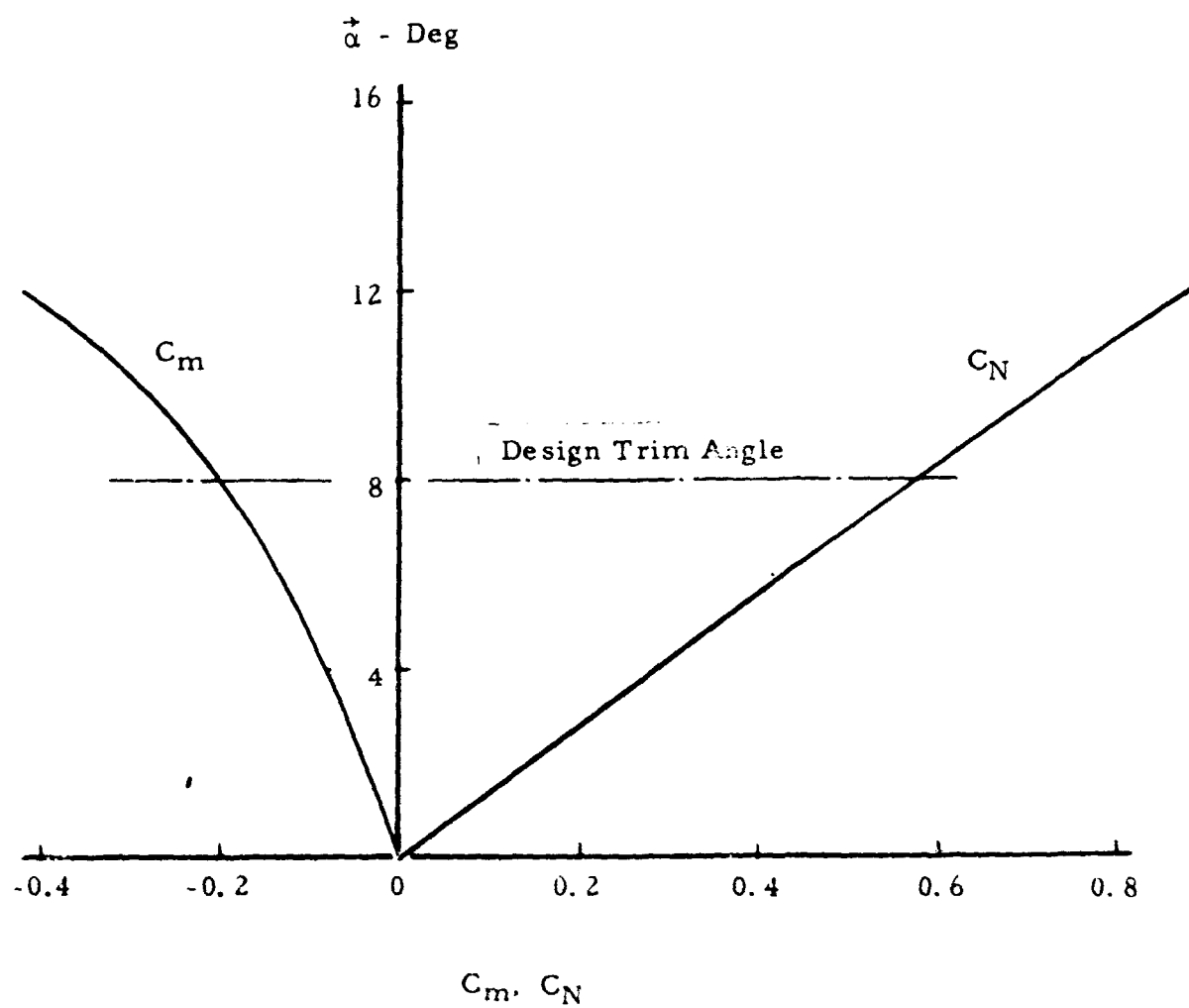
Figure 25.   Subsonic Lift and Pitching Moment Characteristics
of Basic RT0 Bomblet without Wing

41
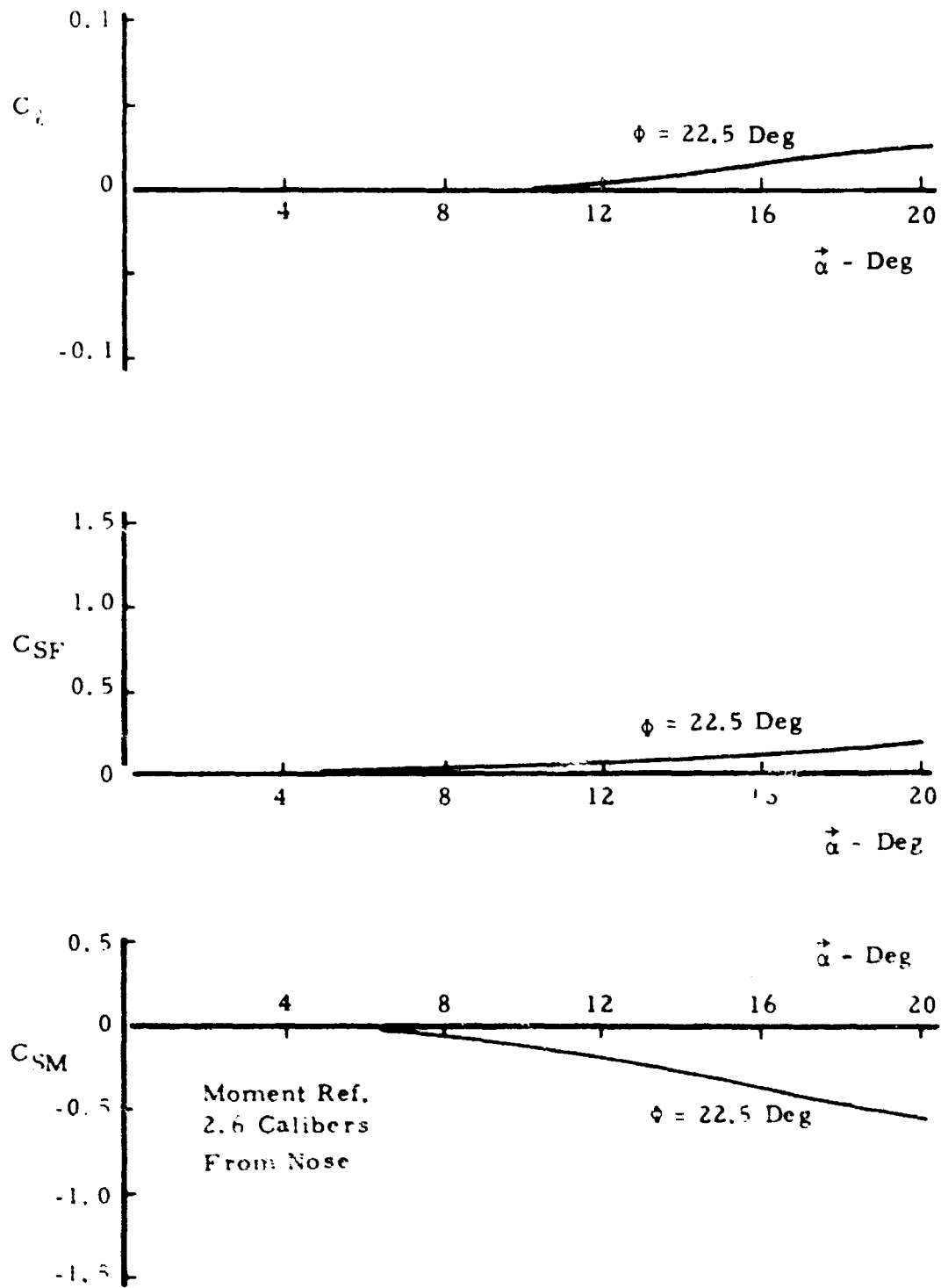
Figure 26. Roll Moment, Side Force, and Side Moment
Characteristics of Basic R T0 Bomblet
without Wings

42

less than 12 degrees by removal of the wing. However, the induced side moment remains large.

For the analytical investigations, it was necessary to estimate the aerodynamic roll characteristics of the basic RT0 bomblet, since the roll dynamics data from the AEDC wind tunnel tests were not available. For the basic RT0 condigurations, a design rolling moment coefficient of 0.0015 was assumed. This is the estimated roll torque produced by $\pm$ 0.3 degree differential deflection of the wing surfaces.

Pitch damping data were also estimated. The pitch damping was assumed to be linear and due entirely to the lift of the stabilizing fins.

A summary of the aeroballistic and aerodynamic coefficients of the basic RT0 bomblet without wings, including Mach number variations, is presented in Table II. These data are presented in the notation used for the 6-DOF trajectory program, as described in Appendix I.

For the alternate RT0 bomblet configuration (S-curve bomblet geometry), the aerodynamic data are identical to that shown in Figure 3 for the basic blunt-nose S-curve bomblet, except that the center-of-gravity is moved 0.1 caliber forward. This bomblet has a design trim angle of attack of 10 degrees at Mach number 0.5, which requires a trim moment coefficient of 0.07. The induced roll moment of the alternate RT0 bomblet configuration is zero for angles of attack less than 16 degrees, and the induced side moment is small in the trim angle-of-attack range. The design rolling moment for the alternate RT0 bomblet is based on 0.3 degrees fin cant.

5. Motion Simulations.

Exact motion simulations have been carried out for the RT0 type bomblet using the 6-DOF trajectory program described in (3) and the aerodynamic and physical characteristics data described in the preceding paragraphs. The 6-DOF motion simulations supplement the basic roll-through-zero dispersion theory, and provide a description of the bomblet flight behavior as influenced by all of the aerodynamic coefficients and the coupling of the rolling and pitching degrees of freedom. In addition, the transient effects introduced by the initial flight conditions are determined by the 6-DOF simulations.

As with the S-curve bomblet concept, the principal motion variables of interest are the angle of attack and the orientation of the angle of attack plane with respect to an earth-fixed reference frame. The latter is described by the angle $\overline{\Phi}$, which is defined in Appendix I. The other variables of interest are the orientation of the angle-of-attack plane with respect to the body axes (angle Φ). and the roll rate.

TABLE II. AERODYNAMIC DATA SUMMARY

RT0 BOMBLET WITHOUT WINGS

AEROBALLISTIC COEFFICIENTS										
Coefficient	Mach Number	$\vec{\alpha} \sim$ Degrees								
		0	2	4	6	8	12	16	20	30
CX	0-0.3	-.226	-.231	-.239	-.246	-.248	-.250	-.264	-.248	-.248
	0.7	-.255	-.258	-.262	-.267	-.272	-.276	-.280	-.264	-.264
	0.9	-.284	-.287	-.294	-.301	-.308	-.314	-.319	-.316	-.316
CN	0-0.3	0	.130	.260	.400	.550	.850	1.210	1.61	2.8
	0.7	0	.130	.270	.420	.570	.900	1.310	1.67	3.2
	0.9	0	.140	.280	.440	.600	.990	1.470	1.98	3.6
CM	0-0.3	0	-.022	-.074	-.135	-.205	-.420	-.719	-1.02	-1.2
	0.7	0	-.049	-.088	-.148	-.243	-.515	-.844	-1.25	-1.5
	0.9	0	-.041	-.102	-.196	-.330	-.701	-1.068	-1.40	-1.65
CMQ = CNR	0-0.3	-34.0	-34.0	-34.0	-34.0	-34.0	-34.0	-34.0	-34.0	-34.0
	0.7	-34.0	-34.0	-34.0	-34.0	-34.0	-34.0	-34.0	-34.0	-34.0
	0.9	-34.0	-34.0	-34.0	-34.0	-34.0	-34.0	-34.0	-34.0	-34.0
CMPR = CNPQ	0-0.3	0	0	0	0	0	0	0	0	0
	0.7	0	0	0	0	0	0	0	0	0
	0.9	0	0	0	0	0	0	0	0	0
CNP	0-0.3	0	0	0	0	0	0	0	0	0
	0.7	0	0	0	0	0	0	0	0	0
	0.9	0	0	0	0	0	0	0	0	0
CL	0-0.3	.0015	.0015	.0015	.0015	.0015	.0015	.0015	.0015	.0015
	0.7	.0015	.0015	.0015	.0015	.0015	.0015	.0015	.0015	.0015
	0.9	.0015	.0015	.0015	.0015	.0015	.0015	.0015	.0015	.0015
CLP	0-0.3	-.739	-.739	-.739	-.739	-.739	-.739	-.739	-.739	-.739
	0.7	-.739	-.739	-.739	-.739	-.739	-.739	-.739	-.739	-.739
	0.9	-.739	-.739	-.739	-.739	-.739	-.739	-.739	-.739	-.739
CMP	0-0.3	0	0	0	0	0	0	0	0	0
	0.7	0	0	0	0	0	0	0	0	0
	0.9	0	0	0	0	0	0	0	0	0

ADDITIONAL AERODYNAMIC COEFFICIENTS (BODY-FIXED)										
CMO	0-0.3	.205	.205	.205	.205	.205	.205	.205	.205	.205
	0.7	.205	.205	.205	.205	.205	.205	.205	.205	.205
	0.9	.205	.205	.205	.205	.205	.205	.205	.205	.205
CSF1	0-0.3	0	.002	.0065	.0135	.026	.072	.134	.193	.3
	0.7	0	.0015	.0045	.0135	.0285	.0815	.1585	.223	.4
	0.9	0	.0015	.0055	.0165	.0365	.1025	.197	.27	.5
CSM1	0-0.3	0	-.004	-.0125	-.0320	-.065	-.115	-.270	-.545	-.545
	0.7	0	-.0065	-.0125	-.0340	-.080	-.255	-.442	-.610	-.610
	0.9	0	-.005	-.0150	-.044	-.080	-.305	-.495	-.635	-.635
CLPHI	0-0.3	0	0	0	0	0	0	.015	.025	.025
	0.7	0	0	0	0	0	.010	.026	.026	.026
	0.9	0	0	0	0	0	.010	.026	.026	.026

Figure 27 depicts the motion histories of a hypothetical RTO bomblet (similar to the basic RTO bomblet configuration) with linear aerodynamics and a design trim lift coefficient of 0.5. In this example,the induced roll moment, side force, and side moment coefficients are assumed to be zero. The dispenser opening conditions are h_o = 1000 ft, V_o = 600 fps, and γ = 15 degrees, and the bomblet is released at zero angle of attack and with a negative roll rate of 2 cycles per second. Following release from the dispenser, the bomblet roll direction reverses, due to the built-in positive roll torque (C_ℓ = 0.0015). At the same time, the angle of attack, $\vec{\alpha}$, responds to the built-in trim moment and rapidly damps to the static trim angle of four degrees. The orientation of angle-of-attack plane with respect to the body axes (angle Φ) is at first oscillatory and then damps to zero, indicating that the rolling and non-rolling trim angle-of-attack vectors are coincident. The orientation of the angle of attack plane with respect to horizontal (angle $\bar{\Phi}$) also shows oscillatory behavior due to pitch-roll coupling effects. The region where $\bar{\Phi}$ is within π/4 of the value of Φ at zero roll rate is indicated in Figure 27, and the corresponding time period is noted to be about 0.92 second. On the basis of the simplified theory, this period is

$$ t = \frac{2d}{V} \sqrt{\frac{\pi\, I_x}{C\ell_o}} \tag{9} $$

$$ t = 0.86\ \text{sec} $$

which illustrates fair agreement between the 6-DOF results and the simplified theory. Comparisons of the theoretical and 6-DOF results for flight path deflection and lateral dispersion show that for this case the theory underpredicts these quantities, the predicted dispersion being about 20 percent less than that indicated by the 6-DOF simulations.

Figure 28 illustrates typical motion histories which were obtained using the measured aerodynamic data for the basic RTO bomblet configuration with the wing at 10 degrees incidence (see Figures 23 and 24). In this case, the induced roll moment overpowers the built-in positive roll torque and produces very large pitch-roll coupling effects. The aerodynamic roll angle, Φ , initially damps, but then slowly diverges. This results in a gradual increase in the induced side moment as well as the induced roll moment, and after approximately 0.8 second, a rapid, unstable, counterclockwise coning motion develops. Figure 29 shows the development of the coning motion in θ , ψ coordinates. Because of the erratic flight dynamics and poor dispersion of the RTO bomblet configuration with wing surfaces, and since there was no apparent method for reducing the roll dependent aerodynamic characteristics contributed by the wing, this type RTO bomblet was dropped from further consideration.
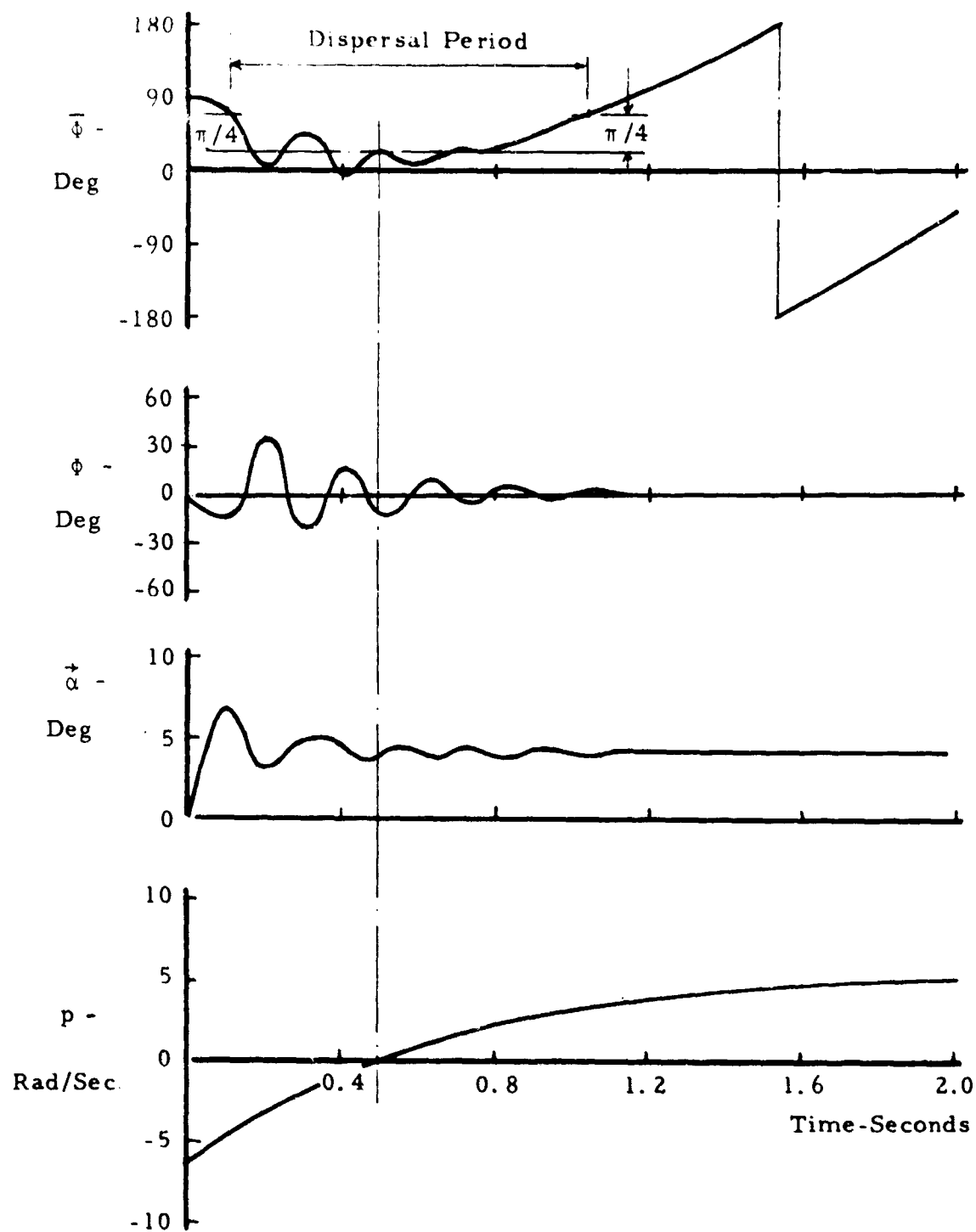
Figure 27. Motion Histories for Winged RT0 Bomblet with Linear Aerodynamics and No Roll Dependent Coefficients

Dispenser Opening Conditions: h_o = 1000 ft, V_o = 600 ft/sec, Y = 15 degrees

46

Figure 28. Motion Histories for Basic RTO Bomblet
with Wing at 10 Degrees Incidence

Dispenser Opening Conditions: h_o - 300 ft,
V_o = 600 ft/sec, Υ = 5 degrees

47

$h_o = 300$ ft

$V_o = 600$ ft/sec

$\gamma_o = 5$ deg

Θ - Deg

ψ - Deg

0.88 Sec
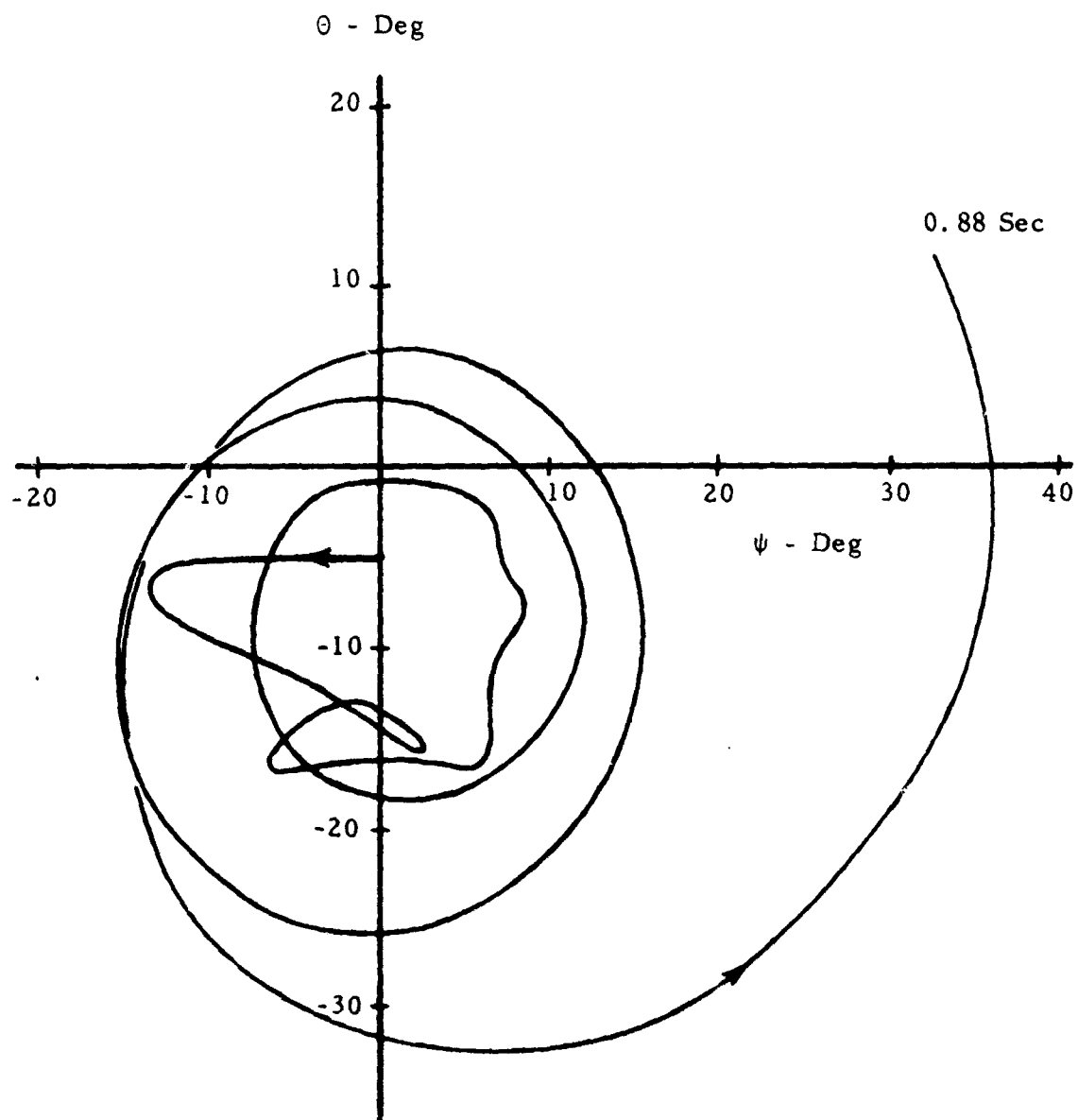
Figure 29.   Motion Diagram for Basic RT0 Bomblet
with Wing at 10 Degrees Incidence

Typical flight characteristics of the wingless RTO bomblet [Figure 21(A)] are depicted in Figure 30 for release conditions identical to those considered for the preceding cases. This configuration possesses an induced side moment, but no induced roll moment at the static trim angle of attack. The angle-of-attack dynamics for the wingless configuration exhibit considerable pitch-roll coupling including relatively large-amplitude poorly-damped oscillations of ϕ, $\vec{\phi}$, and $\vec{\alpha}$. The ϕ oscillations have a near zero mean and consequently the side moment has a small net effect on the motion. Although the $\vec{\phi}$ oscillations are large, there is a relatively long period (about 0.8 second) where the angle-of-attack plane remains within one quadrant, and this provides for significant deflection of the flight path from the zero-lift trajectory.

The alternate RTO bomblet (Figure 22) also has zero-induced roll moment at angles of attack equal to or less than the trim angle of attack and small induced side moment. However, the configuration has less static stability than the basic RTO bomblet without wings. As a result, the angle-of-attack dynamics are distinctly different. Figure 31 shows time histories of the same motion variables which have been examined previously. In this example, the angle, ϕ, does not approach zero, but rather, slowly changes with time as a function of the direction and magnitude of the roll rate. This phenomenon is typical near-resonance behavior, and the magnitude of ϕ represents the phase angle between the rolling and non-rolling trim vectors. After about 0.8 second the orientation of ϕ is such that, for a six-fin configuration, the sign of the side moment changes from negative to positive. The positive side moment reduces the effective damping, and consequently the static trim angle of attack is amplified. These characteristics are often observed in sounding rockets and have been extensively studied in connection with the roll lock-in and resonance problem areas. [See, for example, (5)].

For the alternate RTO bomblet, the angle $\vec{\alpha}$ varies smoothly with time; however, there is only about a 0.5 second period where $\vec{\phi}$ is within $\pi/4$ of the roll-through-zero orientation. Consequently, the dispersion of the alternate RTO bomblet configuration is somewhat poorer than that of the basic RTO configuration without the wing. One of the reasons for this is that the design roll torque for the alternate RTO bomblet configuration is about twice that of the basic configuration.

6.   Trajectory and Impact Pattern Characteristics.

The impact dispersion characteristics of the roll-through-zero type bomblet have been evaluated for the standard dispenser opening conditions I - IV. This permits the RTO bomblet dispersion boundaries to be compared with those for the S-curve type bomblet. The trajectory and impact pattern data for the RTO-type bomblet were computed using the exact six-degrees-of-freedom equations of motion.

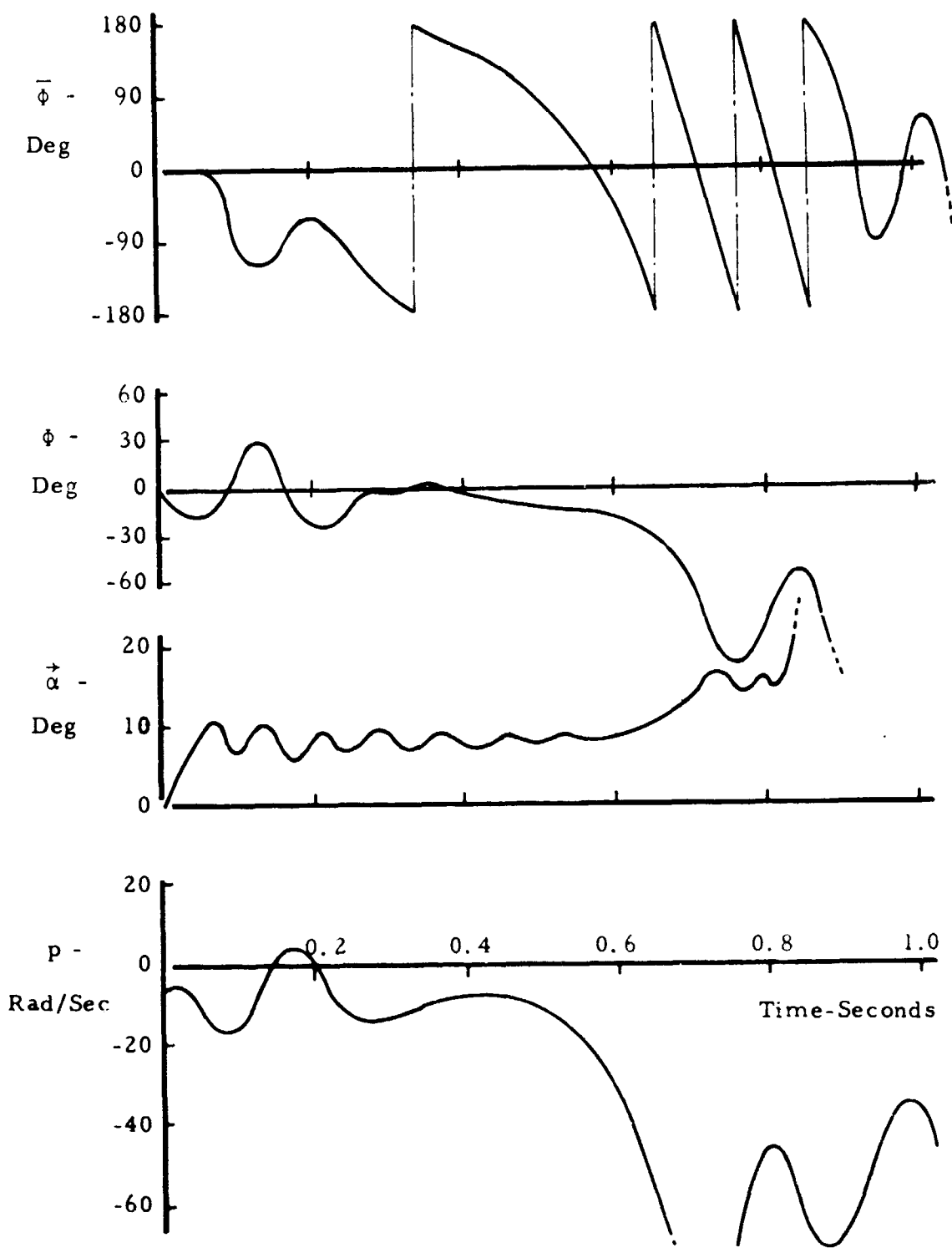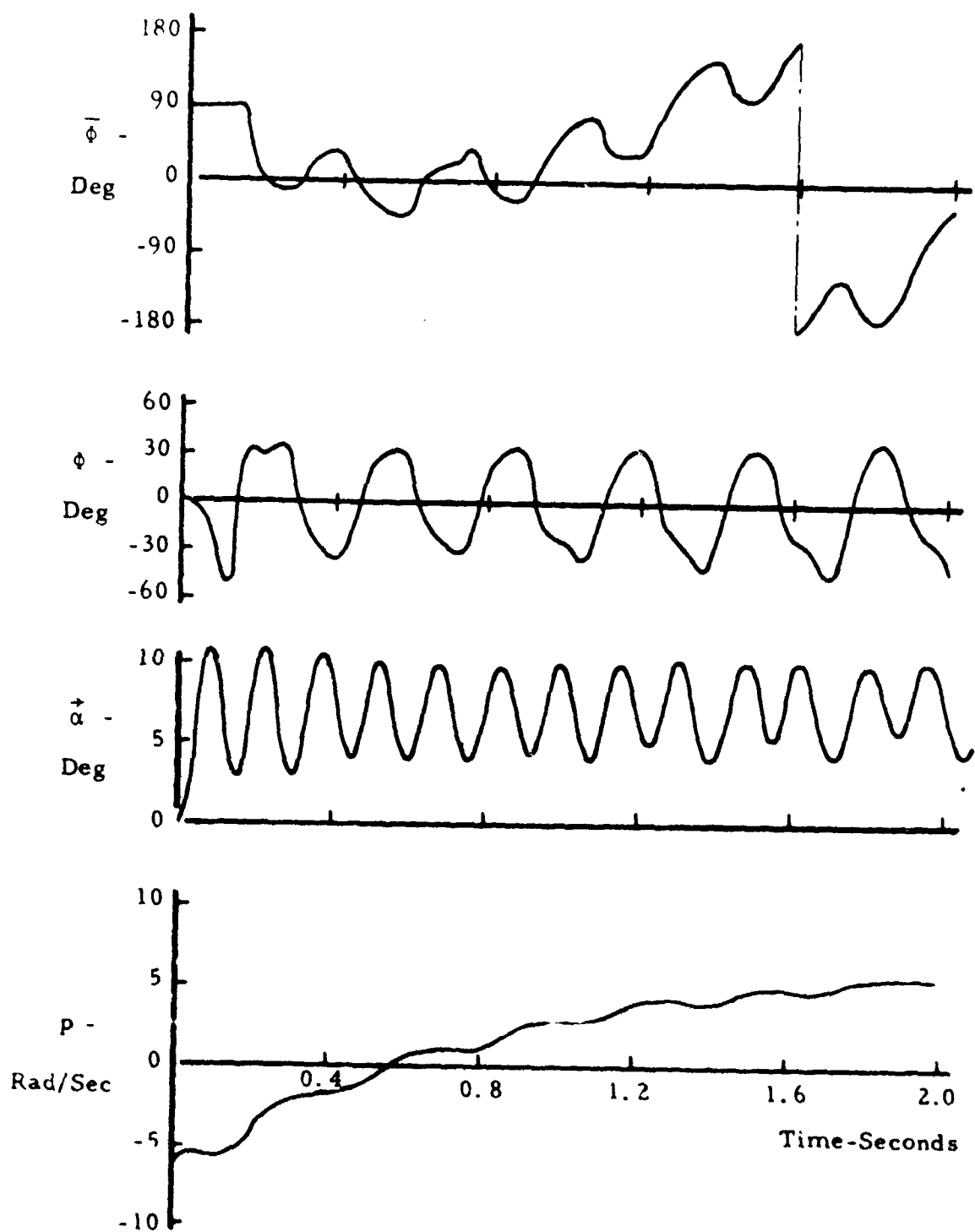Figure 30. Motion Histories for Basic RT0 Bomblet without Wings

Dispenser Opening Conditions: $h_o = 1000$ ft, $V_O = 600$ ft/sec, $Y_s - 15$ degrees
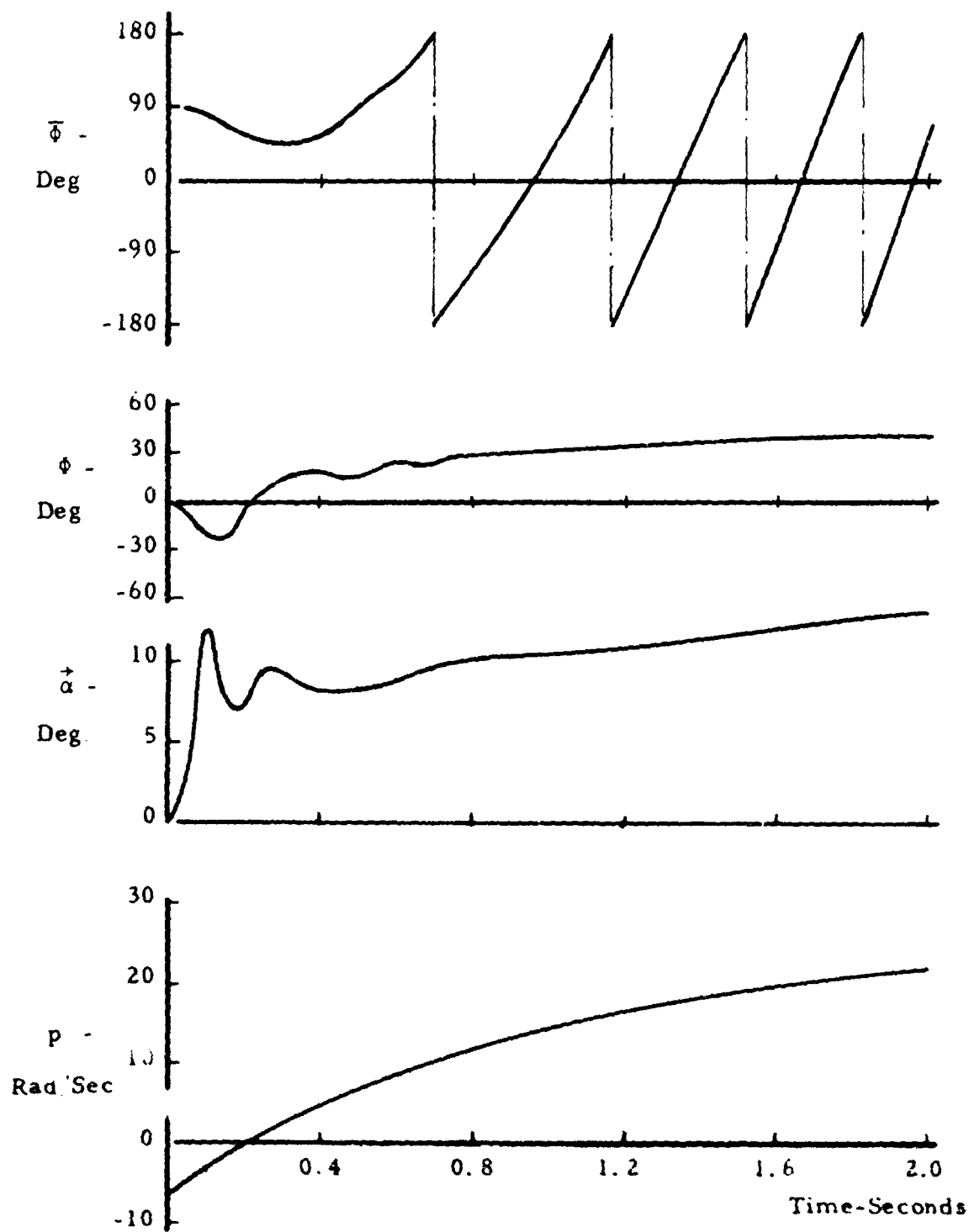
Figure 31. Motion Histories for Alternate RTO Bomblet Configuration

Disperser Opening Conditions: $h_o = 1000$ ft, $V_o = 600$ ft/sec, $Y = 15$ degrees

51

In all cases, it was assumed that the RT0 bomblets had zero angle of attack at the instant of release from the dispenser. This was possible since the trim moment, C_{m_0}, causes the nose of each bomblet to rotate outward from the dispenser line of flight. To establish a ground impact boundary curve, the initial orientation of the y-z body axes was varied by selecting values of : between zero and 2π (at intervals of $\pi/4$). Since each bomblet rolls through almost exactly the same number of roll cycles between release and the roll-through-zero point, the deflection of the flight path at zero roll rate also occurs in various radial directions.

Figures 32-35 present trajectory and dispersion data for the RT0 bomblet configurations.

First, attention will be drawn to the dispersion characteristics of the basic wingless RT0 bomblet, with a mean roll torque coefficient of 0.0015. For the low-speed dispenser opening condition (Figure 32), the dispersion pattern corresponding to the mean roll torque has a mean width of about 150 feet, which is small. For the high-speed dispenser opening conditions, the impact pattern size increases significantly, and for dispenser opening condition III, a mean pattern width of about 600 feet is indicated, while for dispenser opening conditions II and IV, the mean pattern width is in excess of 400 feet.

For dispenser opening conditions II and III, the dispersion patterns of the basic RT0 bomblet tend to be elliptical, with a maximum ratio of along-range to cross-range deflection of about 3:1. For the 45 degree release angle, dispenser opening condition IV, the impact pattern becomes nearly circular.

Alternate RT0 Bomblet Configuration. The dispersion of the alternate RT0 bomblet configuration is compared in Figure 34 and is about one-half that of the basic RT0 bomblet. The reduction in pattern size is due primarily to the larger roll torque coefficient of the alternate bomblet configuration.

Comparison with Theory. In accordance with the simplified theory, the lateral dispersion of the basic RT0 bomblet correlates almost linearly with the slant range between the roll-through-zero point and impact point, except for a slight discrepancy in the case of dispenser opening condition IV. A good correlation with slant range would be expected, because all of the other parameters in the theoretical dispersion equation were held constant in the simulation of the basic configuration. The 6-DOF results confirm that the RT0 bomblet dispersion is essentially independent of the flight velocity.

Cross-Range - Ft
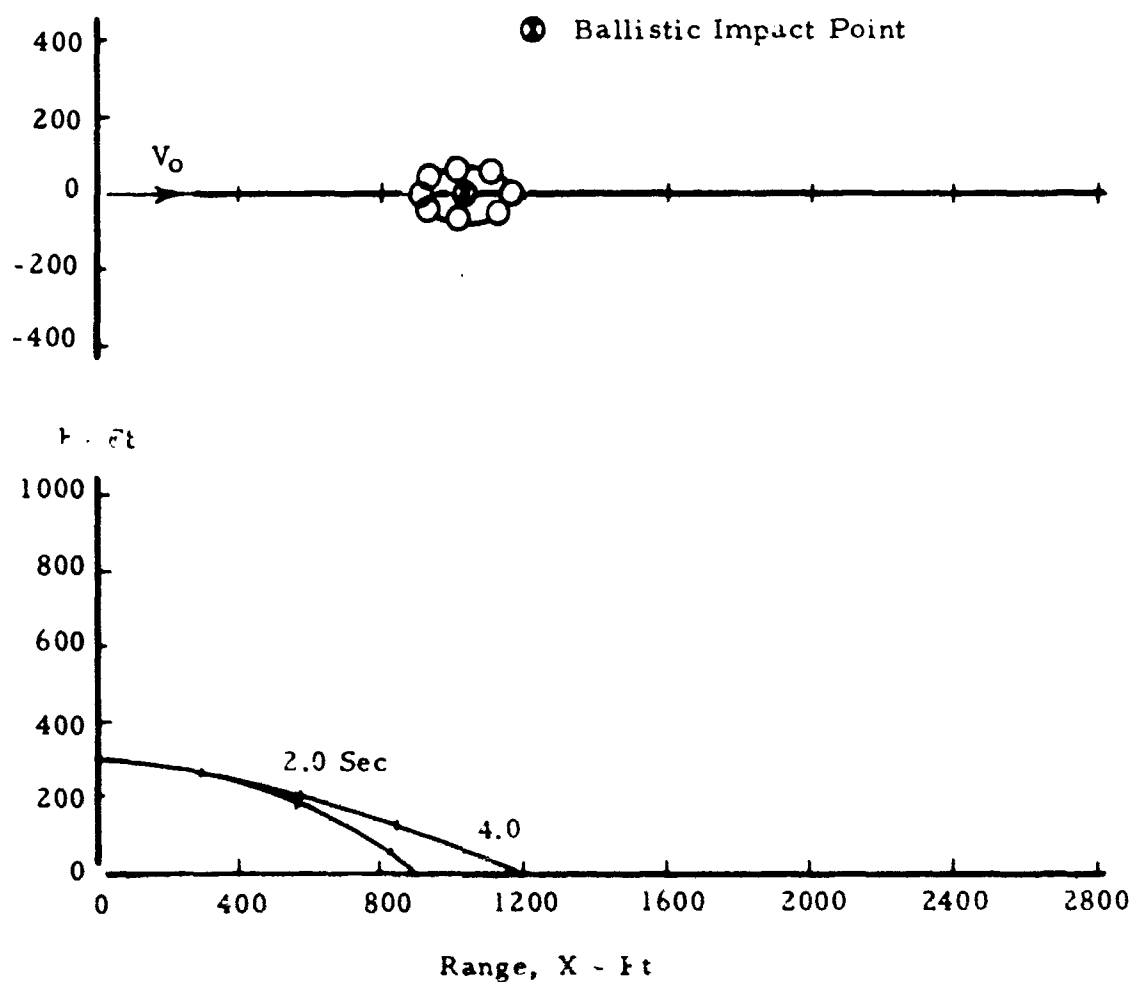
Figure 32. Trajectory and Impact Boundary Data for
Basic RT0 Bomblet with Wing Removed

Dispenser Opening Conditions: h_o = 300 ft,
V_o = 300 ft/sec, Y = 5 degrees

53
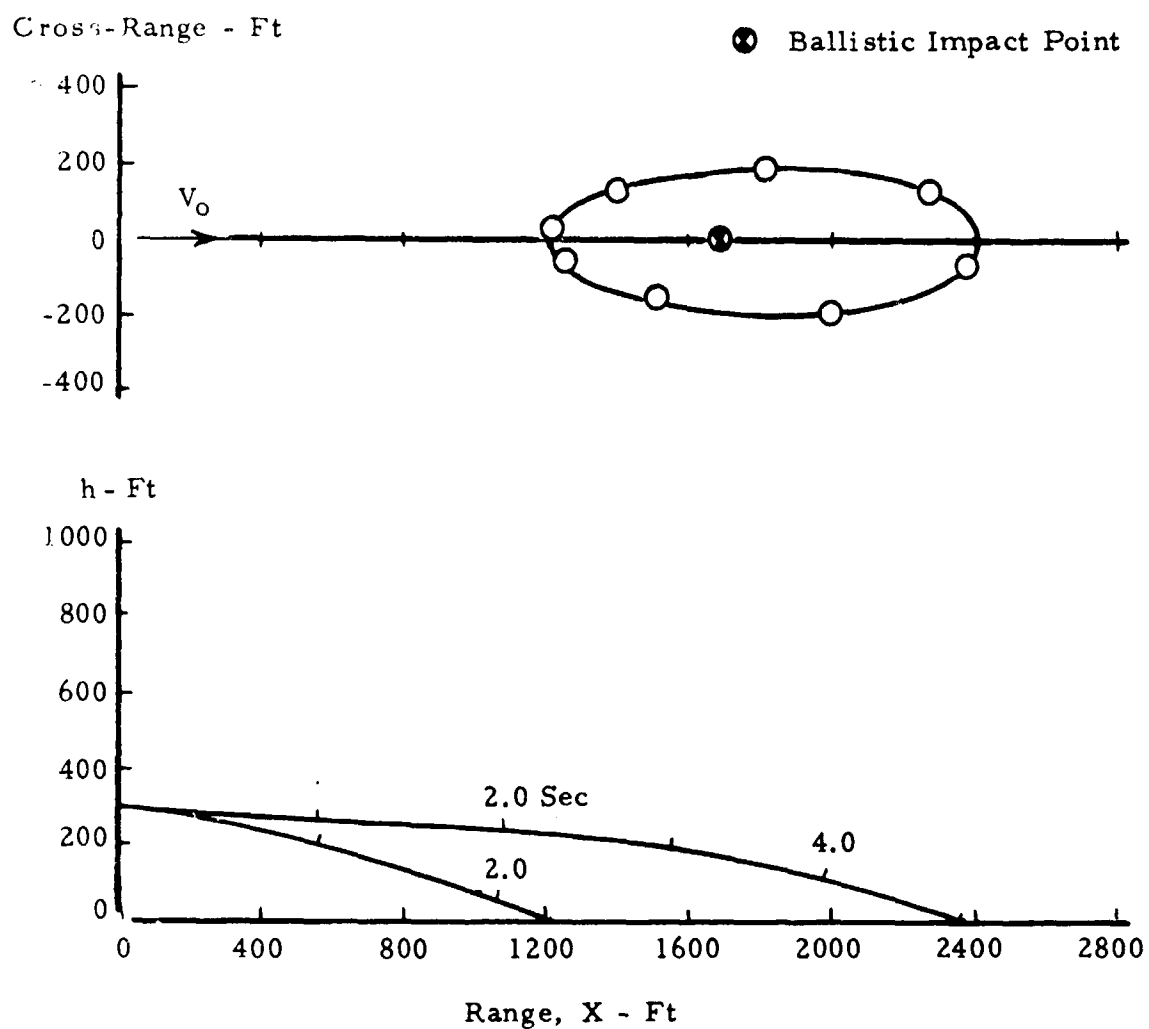
Figure 33.   Trajectory and Impact Boundary Data for
Basic RT0 Bomblet with Wing Removed

Dispenser Opening Conditions: $h_o = 300$ ft,
$V_o = 600$ ft/sec, $\gamma_o = 5$ degrees

54
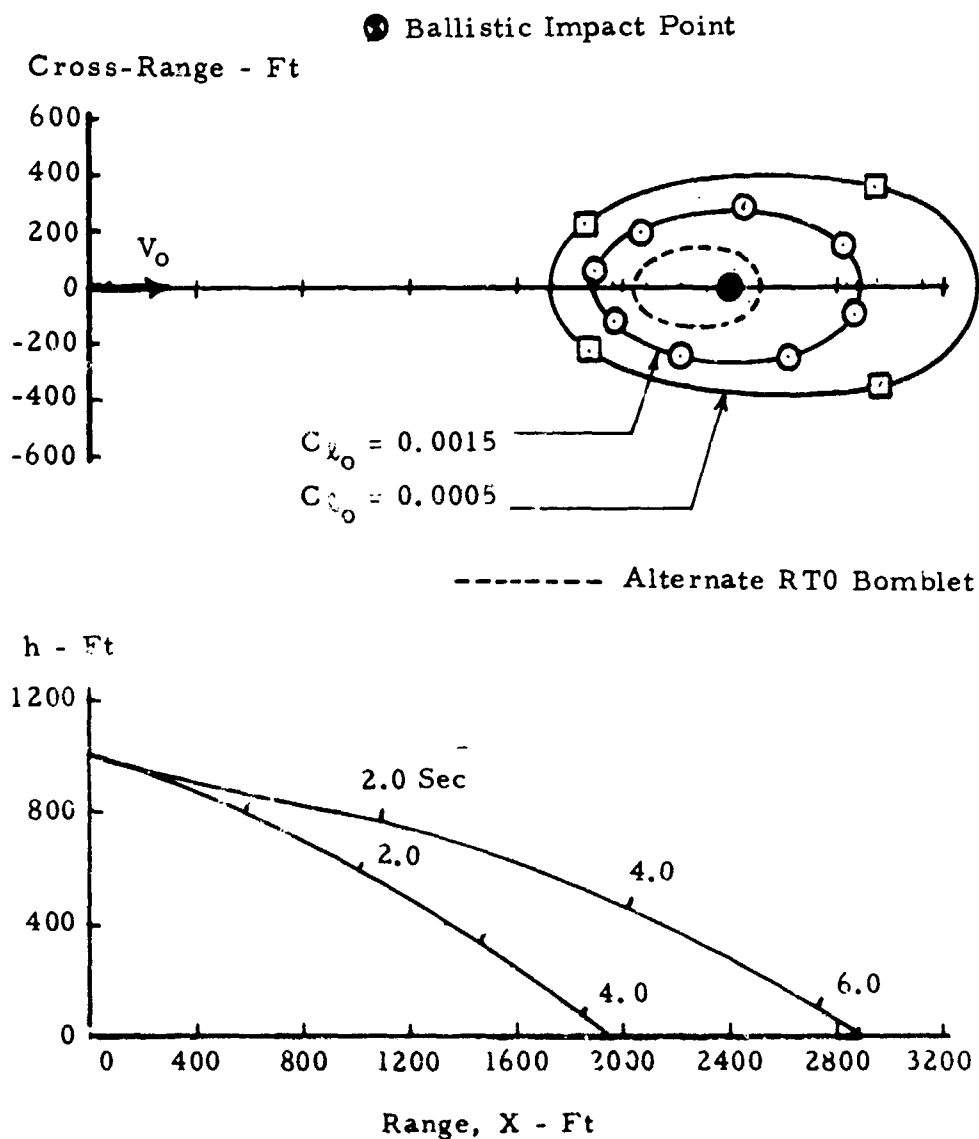
Figure 34.   Trajectory and Impact Boundary Data for
Basic RT0 Bomblet with Wing Removed

Dispenser Opening Conditions: $h_o = 1000$ ft,
$V_o = 600$ ft/sec, $Y_o = 15$ degrees
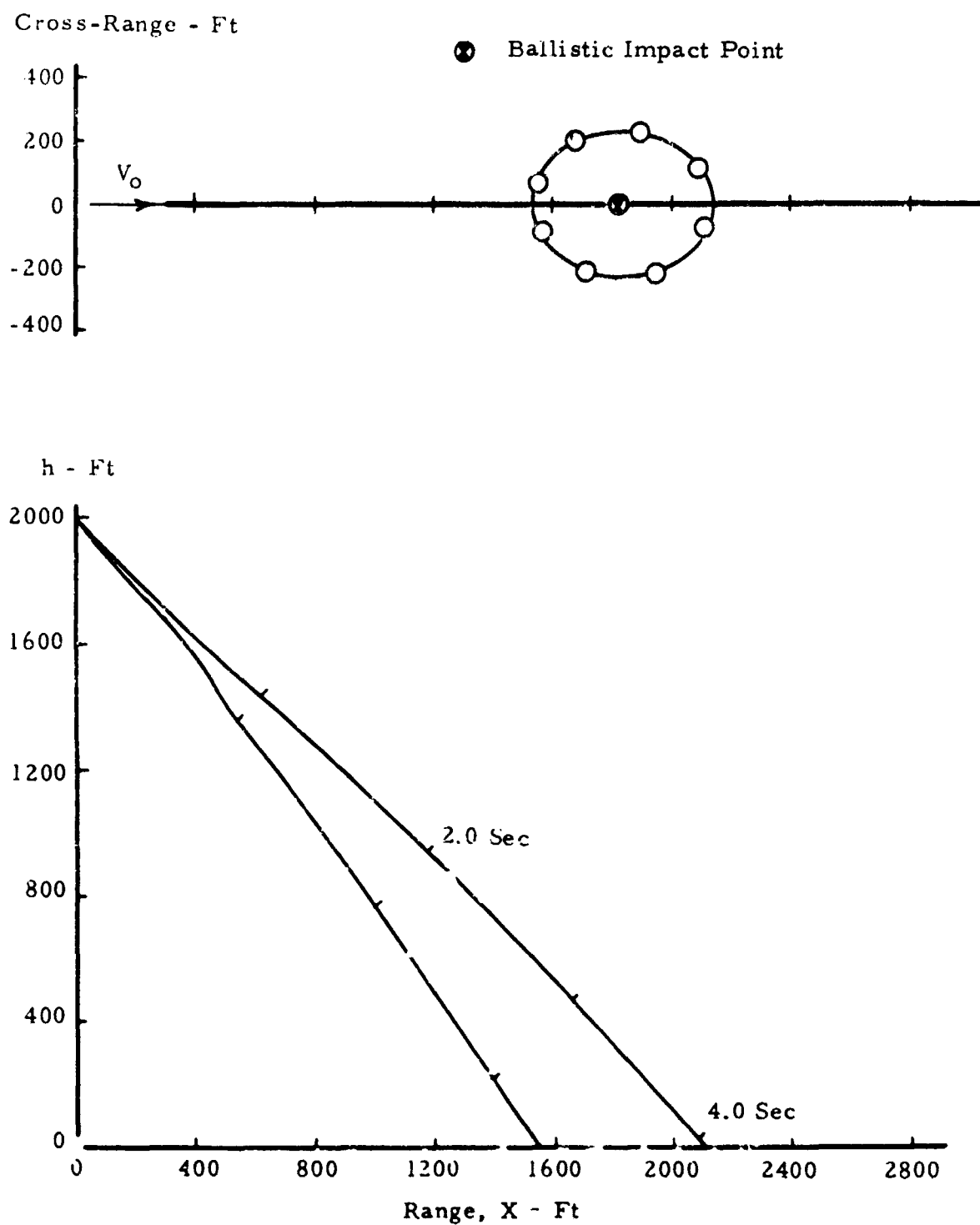
Figure 35. Trajectory and Impact Boundary Data for
Basic RT0 Bomblet with Wing Removed

Dispenser Opening Conditions: $h_0 = 2000$ ft,
$V_0 = 900$ ft/sec, $Y_a = 45$ degrees

Effect of Roll-Torque Coefficient. The impact points which have thus far been presented for the roll-through-zero type bomblet do not, as in the case of S-curve bomblet, represent the maximum dispersion. The computed dispersion is that corresponding to a mean value of the design roll torque, i.e., the design roll torque coefficient. Assuming that the stabilizing fins are canted to produce the design torque, it must be considered that the average fin cant will not be identical for all bomblets due to production tolerances, assembly, damage, etc. The statistical variation of the fin cant may be something like the normal distribution sketched below:
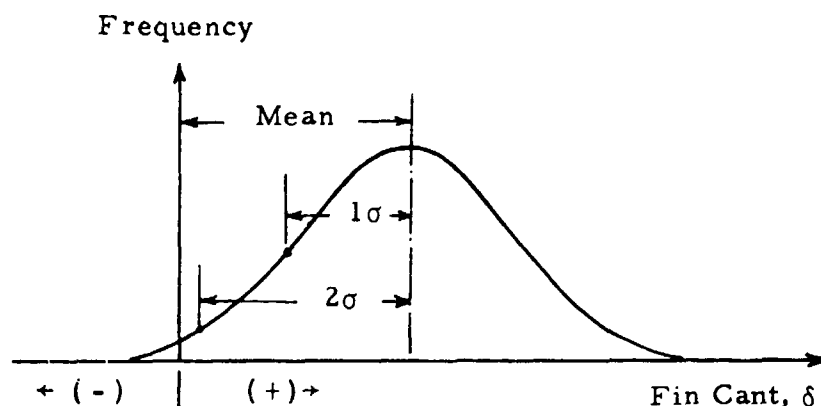
Thus, bomblets which have δ values less than the mean value will tend to have greater dispersion, while those with δ values greater than the mean will have less dispersion. It is also to be noted that some bomblets have negative δ and hence will not reverse their roll direction. These bomblets will have very small dispersion.

Assuming for the basic wingless RT0 bomblet that the two sigma error in the design roll torque coefficient is 0.0010, then the pattern boundary containing 95 percent of the bomblet impacts would be evaluated with C_ℓ = 0.0005. Such a boundary is shown in Figure 34 for dispenser opening condition III. The pattern width is increased to about 800 feet. It is noteworthy that the exact calculation for the effect of C_ℓ on dispersion is in close agreement with theory, i.e., the dispersion is inversely proportional to the square root of the roll torque coefficient.

Effect of Dispenser Spin Rate. The dispenser spin rate affects the RT0 bomblet performance in two ways. First, an increase in the dispenser spin rate delays the time at which roll-through-zero occurs. This causes the trajectory to be deflected closer to the target, thus reducing the dispersion. Second, the dispenser spin rate affects the change in roll orientation which occurs prior to roll-through-zero. If the dispenser

Cross-Range - Ft
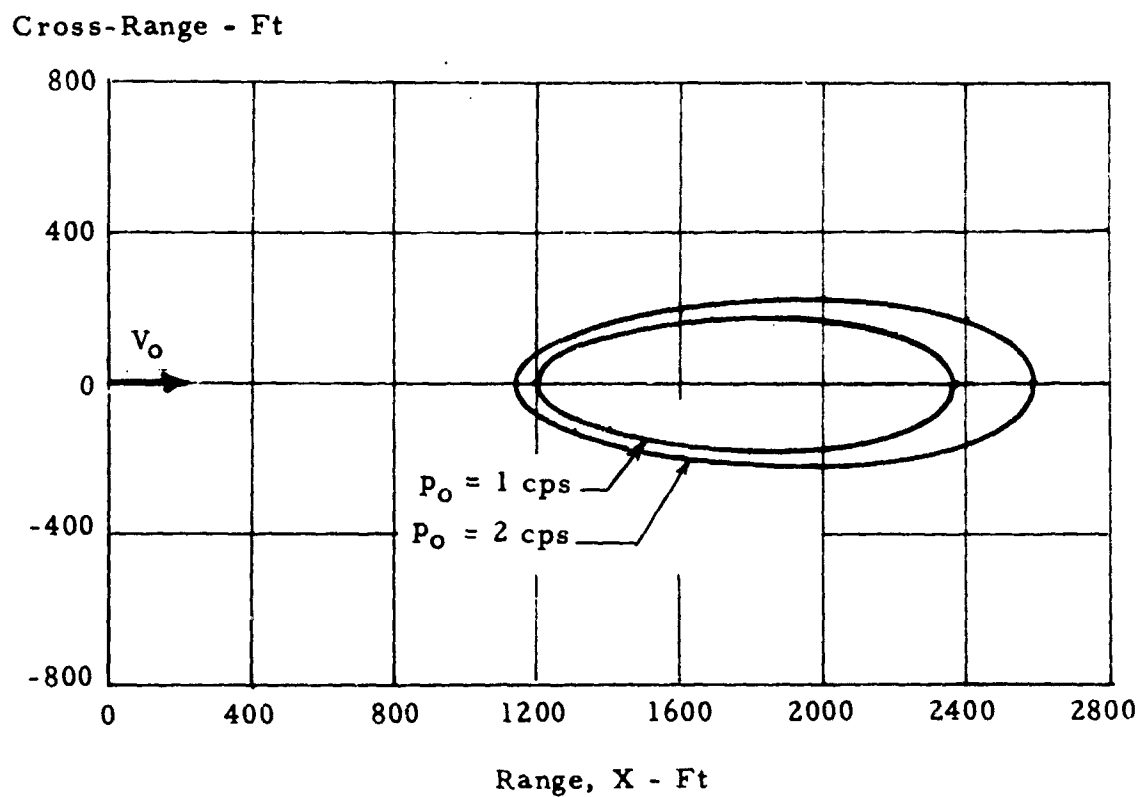
Figure 36.   Effect of Dispenser Spin Rate on RT0 Bomblet
             Impact Dispersion

             Dispenser Opening Conditions: h_o = 300 ft,
             V_o = 600 ft/sec, Υ_o = 5 degrees

58

spin rate were initially zero, the trajectory deflection would be reduced to about one-half the maximum value.

An exact determination of the effect of dispenser spin rate was accomplished by use of the 6-DOF trajectory program. The hypothetical RTO bomblet with linear aerodynamics and design lift coefficient of 0.5 was utilized for the investigation. The bomblet rolling moment coefficient was assumed to be 0.0015. The resulting impact pattern data are shown in Figure 36 for dispenser spin rates of 1.0 and 2.0 cycles per second. The dispersion is about 30 percent greater for the 2.0 cps spin rate.

C. DUAL-MODE BOMBLET

1. Description of Concept.

The dual-mode bomblet concept combines the dispersion capability of the magnus rotor with the terminal flight characteristics of the conventional bomb. The dual-mode feature requires a change in bomblet configuration during flight, for both the purposes of retarding or stopping the spin associated with the magnus-rotor operation and stabilizing the configuration at small angle of attack for terminal impact. The dual-mode bomblet configurations investigated to date [(6), (7), and (8)], have been comprised of a cylindrical body with two-position folding vanes. When closed, the vanes serve to spin the magnus rotor; when open, they provide stabilizing surfaces for ballistic flight. The open vanes also provide an increase in drag which results in a more vertical flight path at impact.

2. Background.

The dual-mode bomblet concept was evolved as a means of providing an efficient fragmenting-warhead geometry, together with a near-vertical impact capability. The cylindrical-shaped warhead, with a fineness ratio of about 2:1, was found to provide greater lethality than existing spherical magnus-rotor munitions.

Preliminary analytical studies of the dual-mode concept were concerned with the bomblet flight dynamics during transition from magnus rotor to ballistic flight. These investigations determined that the dual-mode concept was feasible, based on available but incomplete aerodynamic data. At the same time, limited wind tunnel tests of dual-mode bomblet configurations were undertaken, both for measurement of aerodynamic forces and evaluation of the transition spin dynamics. These experiments revealed that a major problem area was the tendency of the stabilizing vanes to auto-rotate at large angular velocities in the ballistic flight mode. It was realized

59

that autorotation could produce a large magnus moment, which would preclude stable ballistic flight at small angles of attack.

To mitigate this effect, a symmetric blunt-leading-edge vane was developed for the Fliptail dual-mode bomblet (8). This vane produced no autorotation at small angles of attack and only slow autorotation angular velocities at large angles of attack. Subsequently, a successful flight demonstration of the Fliptail bomblet was accomplished at 120 knots airspeed, and transition from the magnus rotor mode to ballistic flight was observed to occur in about one second.

3. Configurations.

For the present effort, both a vane-stabilized (Fliptail-type) dual-mode bomblet and a ballute-stabilized dual-mode bomblet were selected for evaluation. Each bomblet is comprised of a cylindrical warhead body, 1.78 calibers in length, plus the necessary spin-torque vanes and stabilizing appendages. The warhead body was scaled to 3.38 inches in diameter, and the bomblet weight was assumed to be 6.5 pounds, consistent with the Fliptail bomblet characteristics. The external configuration of each bomblet and the corresponding physical characteristic data are summarized in Figure 37.

Each dual-mode bomblet has the same magnus-rotor configuration, consisting of four spin-torque vanes and two square-type end plates. The end plates serve primarily to hold the spin-torque vanes in position and are jettisoned at the start of transition.

Previous analytical work (8), (9) and unpublished results from flight tests show that the magnus-rotor configuration is dynamically stable in gliding flight.

Two ballistic versions of the Fliptail bomblet have been considered, corresponding to vane trail angles, ζ , of zero and 45 degrees. Two vane angles were selected for evaluation, because of the variation in the restoring moment, magnus moment, and spin damping characteristics with vane angular position.

The ballute-type stabilizing device was selected because of its simplicity of operation, and it is envisioned that its deployment would be initiated by an internal pressure source. The ballute-type stabilizer necessitates the use of separate throw-away spin vanes for magnus rotor operation.

The ballute geometry is based on the data of (10), and includes a circumferential flow separation ring. In addition, four longitudinal ribs are attached to the forward surface of the ballute as a means of increasing the roll damping.
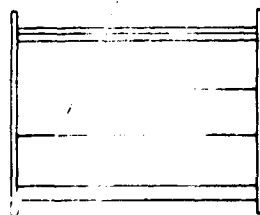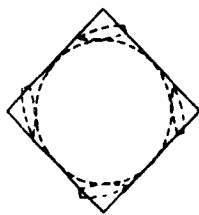
a) Magnus Rotor

Weight = 6.5 lbs.
$I_x = 0.00278$ slug-ft^2
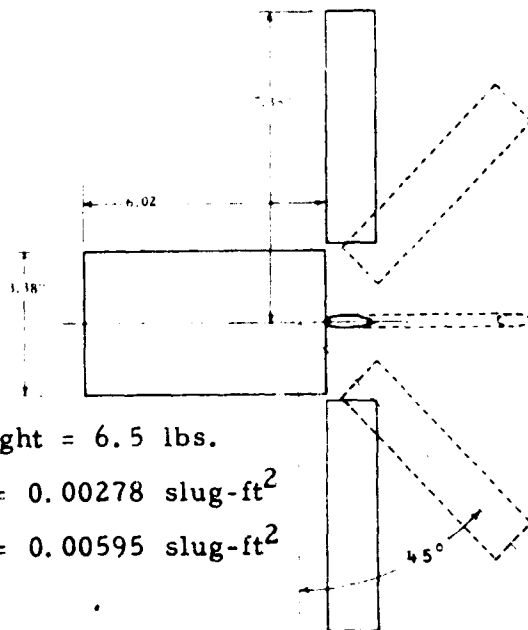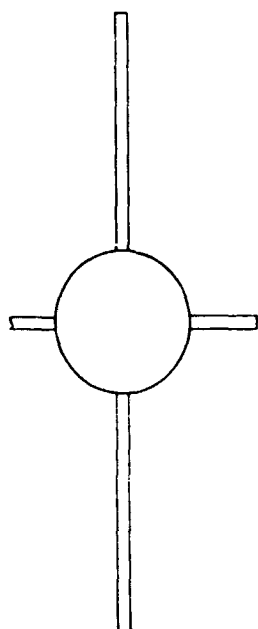
Weight = 6.5 lbs.
$I_x = 0.00278$ slug-ft^2
$I = 0.00595$ slug-ft^2

b) Vane-Stabilized Bomblet
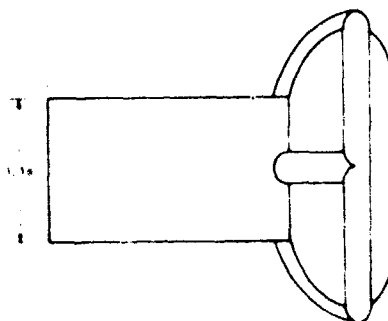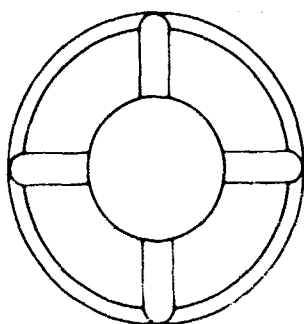
Weight - 6.5 lbs.
$I_x = 0.00278$ slug-ft^2
$I = 0.00595$ slug-ft^2

c) Balute-Stabilized Bomblet

Figure 37.   Dual-Mode Bomblet Configurations
and Physical Characteristics Data

61

4.   Aerodynamic Data - Ballistic Configurations.

Static Aerodynamic Data.   The static aerodynamic force and
moment coefficients for the dual-mode bomblet configurations were obtained
from wind tunnel tests at AEDC.   The details of these tests, which were
accomplished concurrently with the present contractual effort, are described
in (4).   Subsonic normal force, drag force, and pitching moment
data were measured at angles of attack from zero to 160 degrees, and the
effect of the aerodynamic roll angle was determined for angles of attack
from zero to 20 degrees.   These data are presented in Figures 38-41.

The principal difference in the static aerodynamic character-
istics of the three dual-mode bomblets is the variation of the pitching moment
with angle of attack.   The trailing-vane configuration (ζ = 45 degrees) is
more stable than the configuration with no trail (ζ = 0) at all angles of
attack.   The ballute configuration has greater stability than either of the
vane configurations at zero angle of attack but less stability at 90
degrees angle of attack.   The ballute configuration is also stable in backward
flight, which may be an undesirable characteristic.   At zero angle of attack,
the ballute configuration has about three times as much drag as either of the
vane-stabilized configurations.

Dynamic Aerodynamic Coefficients for Vane-Stabilized
Bomblet.   Magnus force and moment and spin damping data for the vane-
stabilized bomblets were estimated from published and unpublished Aerojet-
General test data for the Fliptail bomblet.   The magnus coefficients for the
vane configurations with zero trail were determined from tests of a model
with twisted vanes   and hence may be considerably in error.   The magnus
data for the trailing-vane configuration were measured at low spin rates
and may also be inaccurate.   However, the overall magnitude and trend of
the magnus data are believed to be adequate for investigation of the dual-
mode bomblet transition dynamics.

Pitch damping data for the vane-type dual-mode bomblet were
based on previous estimates for the Fliptail bomblet.   The rolling moment
due to vane cant was estimated from the data of (11).

Table III summarizes the aerodynamic data which were used
for six-degrees-of-freedom simulations of the vane-type dual-mode bomblet
(ζ = 45 degrees).

Dynamic Aerodynamic Coefficient for Ballute-Stabilized
Bomblet.   Magnus and damping coefficients for the ballute-stabilized bomb-
let had to be approx   since neither adequate theory nor test data were
available.   The pitch   ng was estimated from the assumption that the
ballute drag force wou'd align with the local flow.   The magnus force and
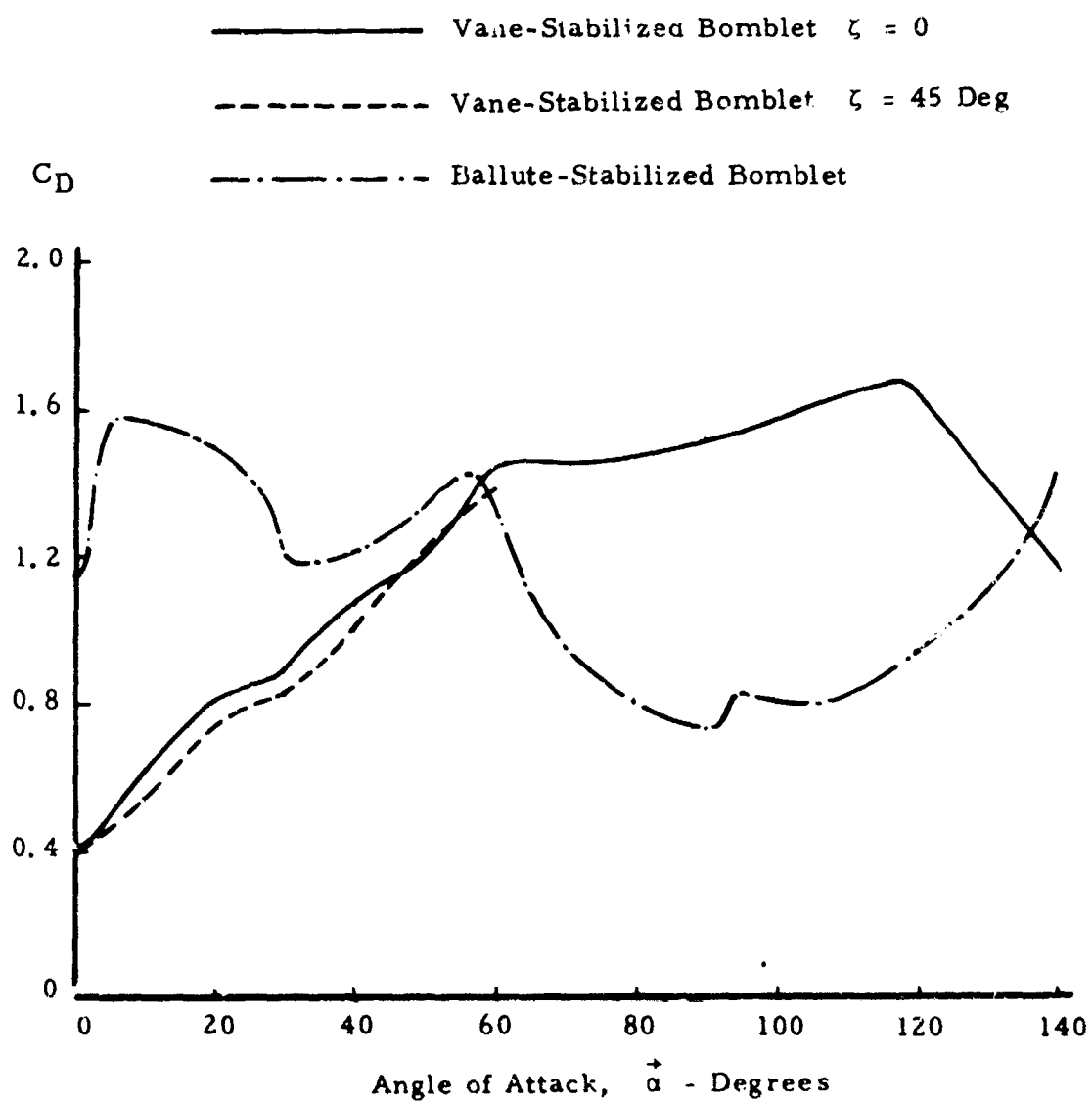
Figure 38. Drag Coefficien` of Dual-Mode Bomblet Configurations
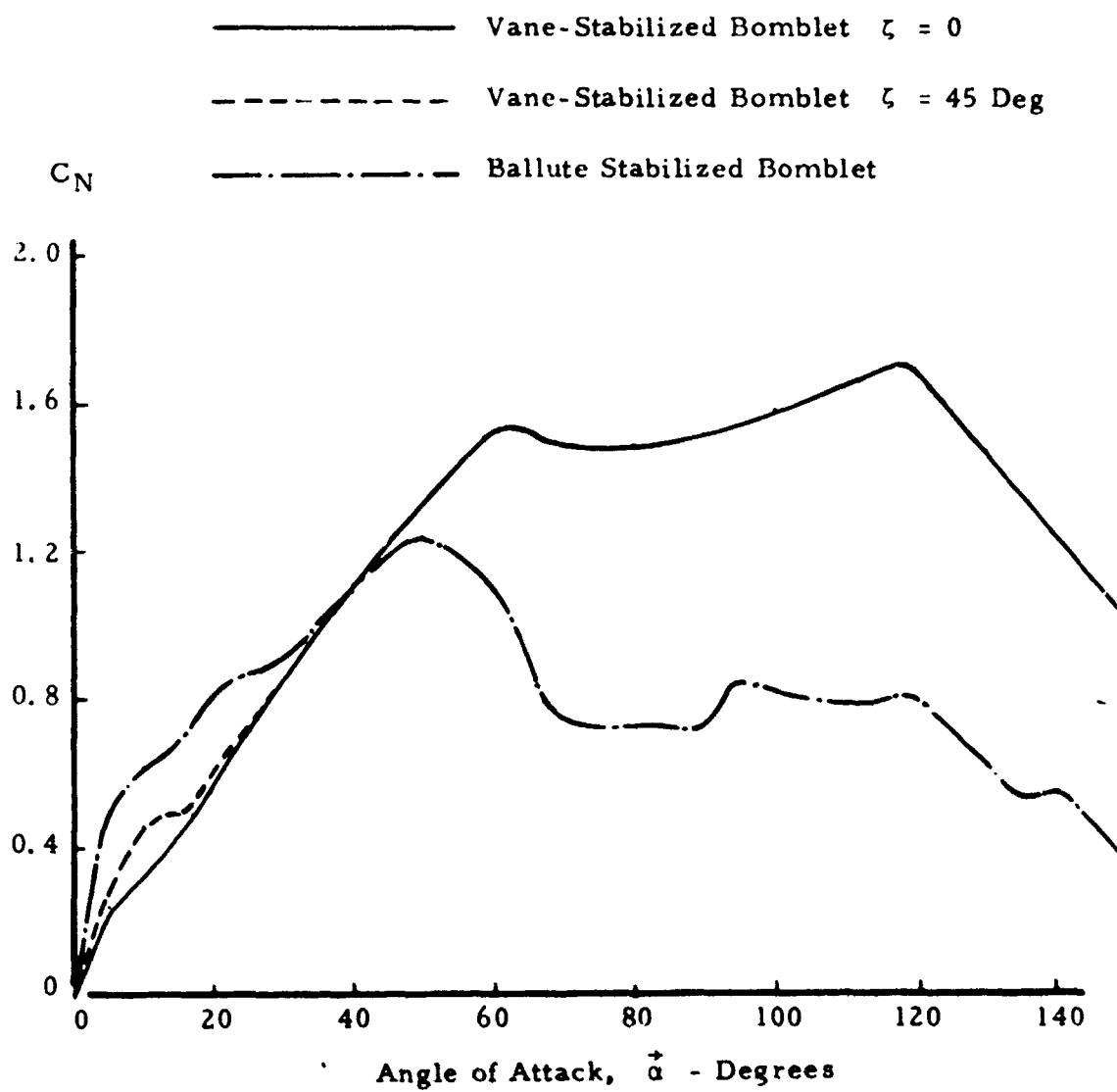
Figure 39.   Normal Force Coefficient of Dual-Mode Bomblet
             Configurations
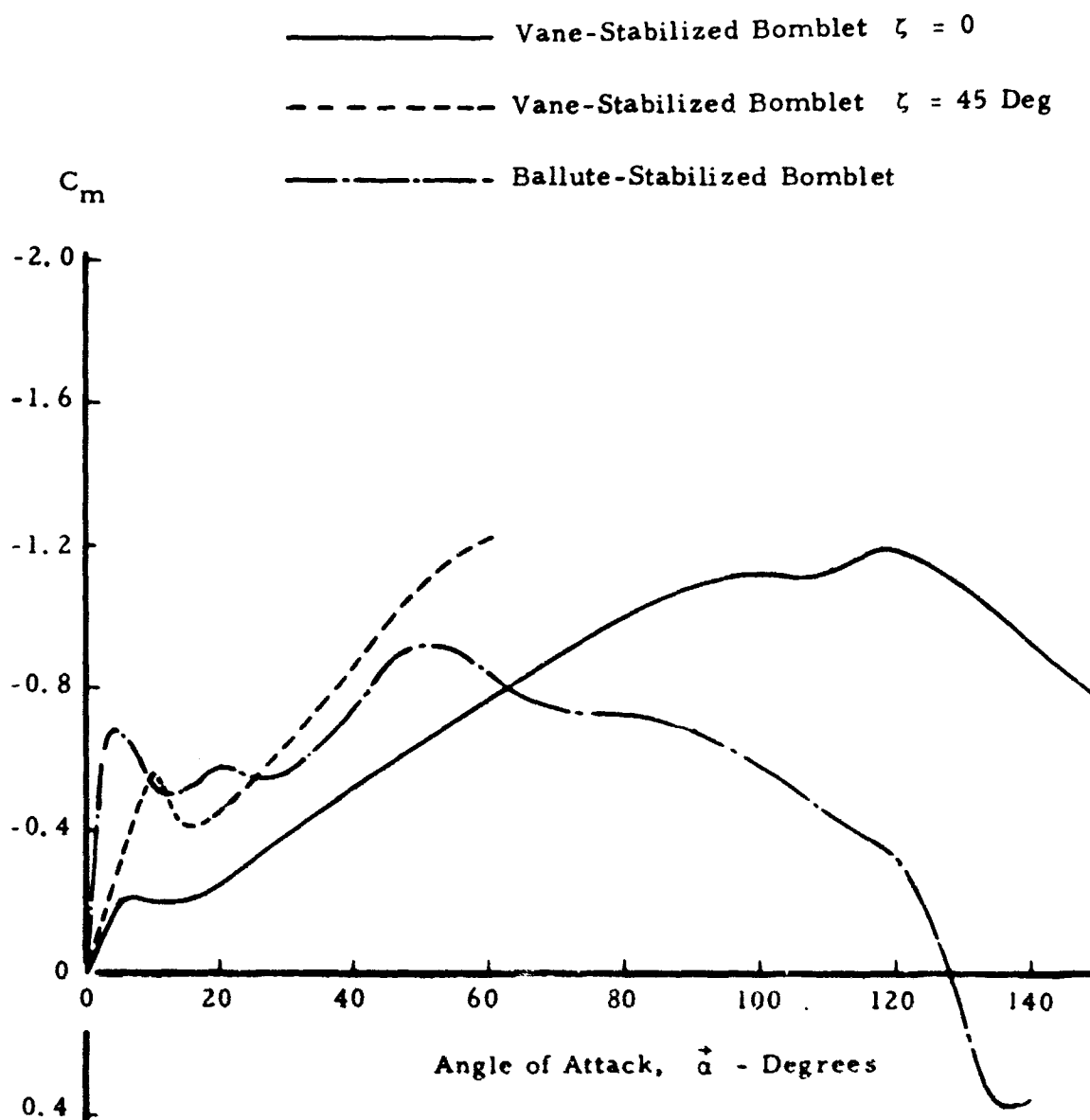
Figure 40. Pitching Moment Coefficient of Dual-Mode
Bomblet Configurations
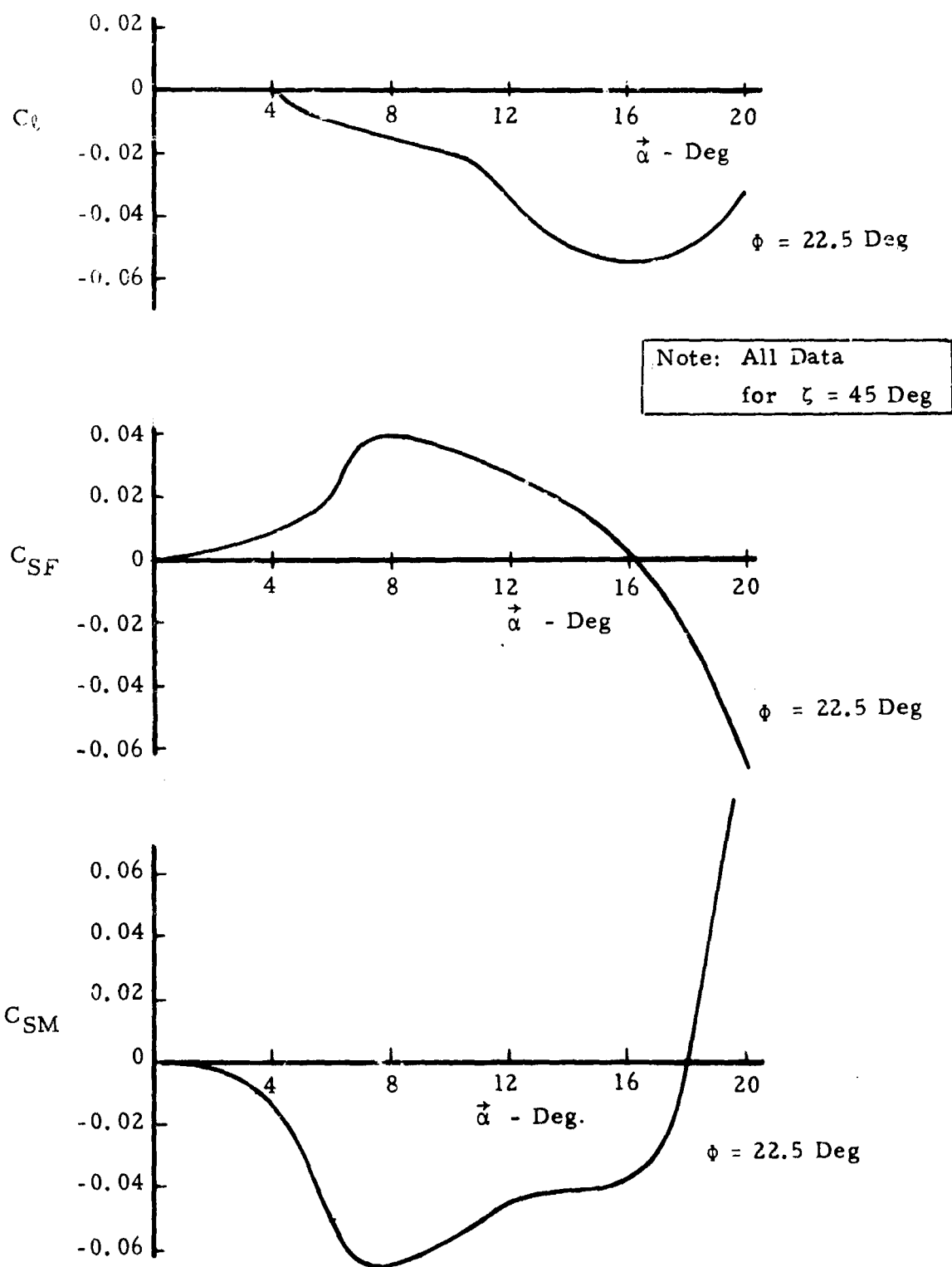
Figure 41.   Rolling Moment, Side Force, and Side Moment
Characteristics of Vane-Stabilized Dual-Mode
Bomblet as a Function of Angle of Attack and
Aerodynamic Roll Angle

66

TABLE III. AERODYNAMIC DATA SUMMARY: VANE-STABILIZED DUAL-MODE BOMBLET

($\zeta = 45$ DEGREES)

AEROBALLISTIC COEFFICIENTS

$\alpha \sim$ Degrees

Coefficient	0	2	4	6	10	15	20	25	30	40	50	60	70	80	90	100	110	125	140	180
CX	-.38	-.385	-.410	-.430	-.485	-.550	-.570	-.530	-.490	-.420	-.330	-.170	-.07	.01	.11	.25	.36	.57	.80	.55
CN	0	.09	.15	.33	.45	.49	.61	.72	.81	1.09	1.32	1.50	1.64	1.75	1.82	1.75	1.80	1.65	1.55	0
CM	0	-.08	-.20	-.37	-.54	-.41	-.48	-.55	-.65	-.86	-1.08	-1.22	-1.45	-1.59	-1.80	-1.90	-1.95	-1.89	-1.70	0
CMQ	-8.4	-8.4	-8.4	-8.4	-8.4	-8.4	-8.4	-8.4	-8.4	-8.4	-8.4	-8.4	-8.4	-9.4	-8.4	-8.4	-8.4	-8.4	-8.4	-8.4
CNR	-8.4	-8.4	-8.4	-8.4	-8.4	-8.4	-8.4	-8.4	-8.4	-8.4	-8.4	-8.4	-8.4	-8.4	-8.4	-8.4	-8.4	-8.4	-8.4	-8.4
CMPR	0	0	0	0	0	0	0	0	0	0	0	0	0	0	0	0	0	0	0	0
CNPQ	0	0	0	0	0	0	0	0	0	0	0	0	0	0	0	0	0	0	0	0
CNP	0	-.08	-.16	-.24	-.40	-.80	-1.40	-2.20	-3.15	-4.72	-4.72	-4.2	-3.0	-2.0	-2.0	-2.0	-2.0	-2.0	-2.0	0
CL	0	0	0	0	0	0	0	0	0	0	0	0	0	0	0	0	0	0	0	0
CLP	-8.5	-8.5	-8.5	-8.5	-8.5	-8.5	-8.5	-8.5	-8.5	-8.5	-8.5	-8.5	-8.5	-8.5	-8.5	-8.5	-8.5	-8.5	-8.5	-8.5
CMF	0	.08	.16	.24	.40	.60	.80	1.2	1.80	2.7	3.5	4.5	5.4	6.25	6.25	6.25	5.40	1.75	0	0

ADDITIONAL AERODYNAMIC COEFFICIENTS (BODY-FIXED)

Coefficient	0	2	4	6	10	15	20	25	30	40	50	60	70	80	90	100	110	125	140	180
CYO	0	0	0	0	0	0	0	0	0	0	0	0	0	0	0	0	0	0	0	0
CZO	0	0	0	0	0	0	0	0	0	0	0	0	0	0	0	0	0	0	0	0
CMO	0	0	0	0	0	0	0	0	0	0	0	0	0	0	0	0	0	0	0	0
CNO	0	0	0	0	0	0	0	0	0	0	0	0	0	0	0	0	0	0	0	0
CSF1	0	0	.008	.024	.034	.013	-.065	0	0	0	0	0	0	0	0	0	0	0	0	0
CN1	0	0	-.01	-.08	-.06	.09	.05	0	0	0	0	0	0	0	0	0	0	0	0	0
CSF3	0	0	0	0	0	0	0	0	0	0	0	0	0	0	0	0	0	0	0	0
CSM1	-.002	-.0035	-.0175	-.049	-.055	-.040	.106	0	0	0	0	0	0	0	0	0	0	0	0	0
CM1	0	0	-.02	-.12	-.03	.17	.06	0	0	0	0	0	0	0	0	0	0	0	0	0
CSM3	0	0	0	0	0	0	0	-.01	0	0	0	0	0	0	0	0	0	0	0	0
CLPH1	0	0	-.0015	-.0100	-.0250	-.0530	-.0325	0	0	0	0	0	0	0	0	0	0	0	0	0
CLPH2	0	0	0	0	0	0	0	0	0	0	0	0	0	0	0	0	0	0	0	0

Note: All data low speed.

moment were determined with the aid of magnus-rotor data, for angles of attack near 90 degrees; at intermediate angles of attack the magnus force was assumed to be due entirely to the lateral cross force on the windward rib. The spin damping was estimated from the local cross force on the ribs except where they were immersed in the wake. The dynamic coefficients for the ballute stabilized bomblet are summarized below:

$$C_{m_q} = -3.9$$

$$C_{N_p} = -0.72 \; : \; \vec{\alpha} = 90 \text{ degrees}$$

$$C_{M_p} = 1.00 \; : \; \vec{\alpha} = 90 \text{ degrees}$$

$$C_{M_p} = 0.86 \; : \; \vec{\alpha} = 0$$

$$C_{\ell_p} = -.203 \; : \; \vec{\alpha} = 90 \text{ degrees}$$

$$C_{\ell_p} = -.162 \; : \; \vec{\alpha} = 0$$

5. Aerc dynamic Data - Magnus Rotor Configuration.

Aerodynamic data for the magnus rotor flight phase were taken from (8). The coefficient values at 90 degrees angle of attack and subsonic conditions are as follows:

$$C_D = 1.13$$

$$C_{L_p} = 1.23$$

$$C_\ell = 0.075$$

$$C_{\ell_p} = -0.170$$

6. Motion Simulations.

The practicability of the dual-mode bomblet concept depends almost entirely upon the bomblet behavior during the transition period following termination of magnus-rotor flight. The transition to ballistic flight must occur rapidly, and at the end of the transition period the bomblet must have attained a stable motion.

One of the purposes of the present effort was to ascertain the factors which contribute to improved transition behavior. Secondly, there was need for investigation of the dynamic effects introduced by the addition of roll-dependent aerodynamic coefficients, accidental fin cant, and body-fixed longitudinal asymmetry, factors which had not heretofore been considered.

Initial Conditions   Motion simulations have been carried out for the dual-mode bomblets, using the 6-DOF trajectory program described

68

in (3). The bomblet transition dynamics were investigated for initial flight conditions corresponding to steady gliding flight in the magnus-rotor mode, specifically,

$$V_O = 175 \text{ ft/sec}$$

$$\gamma_O = 64.93 \text{ degrees}$$

$$p_O = 548 \text{ rad/sec}$$

$$\vec{\alpha}_O = 90 \text{ degrees}$$

Vane-Type Dual-Mode Bomblet ($\zeta = 0$). The transition dynamics of the vane-type dual mode bomblet (no vane trail, $\zeta = 0$) were computed without consideration of configurational asymmetries. The resulting histories of spin rate, angle of attack, and azimuth orientation are presented in Figure 42. Although the bomblet despins in about 1.5 seconds the angle of attack remains near 90 degrees for several seconds, and after five seconds the angle of attack oscillations still have an amplitude of 45 degrees. Inspection of the azimuth motion (Euler angle ψ) reveals that the bomblet develops a very rapid coning motion during despin, which persists even though the spin rate approaches zero. The coning motion damps slowly and only when the coning rate has decreased to about 4 cps does the angle of attack begin to diminish.

An arbitrary increase in the spin damping coefficient by a factor of two did not significantly reduce the large amplitude coning motion of this configuration.

From a dynamical viewpoint, the transitional motion of this bomblet is quite complex. For the first 0.34 second of transition, the motion is characterized by a highly unstable nutation, but subsequently the motion breaks out into a precessional-type motion, with the coning opposite to the direction of axial spin. The above behavior is believed to be initiated by the large negative magnus moment which exists at 90 degrees angle of attack. The persistence of the large angle of attack coning motion is due to the fact that this mode is lightly damped.

Vane-Type Dual-Mode Bomblet ($\zeta = 45$ Degrees) The effect of increasing the vane trail angle, ζ , to 45 degrees is depicted in Figure 43. The transition dynamics are greatly improved, primarily as a result of the change in magnus moment characteristics. The spin momentum is dissipated without the development of a rapid coning motion and the nutational motion is suppressed. Within 1.5 seconds from the time of vane deployment, the total angle of attack decreases to less than 10 degrees. The altitude loss during this period is approximately 250 feet.

69
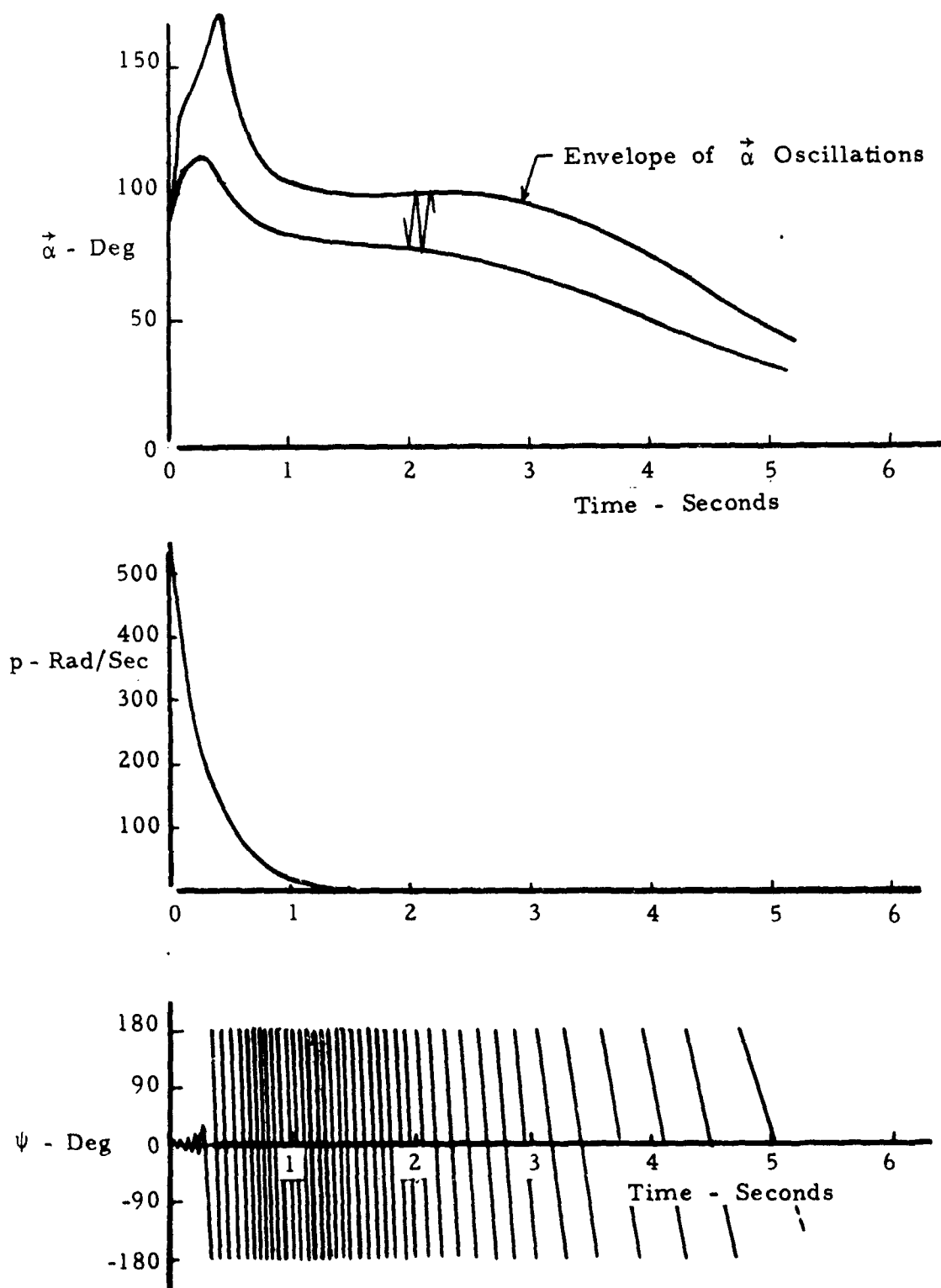
Figure 42. Motion Histories During Transition from
Glide-to-Ballistic Flight

Vane-Type Dual Mode Bomblet ($\zeta = 0$)

70
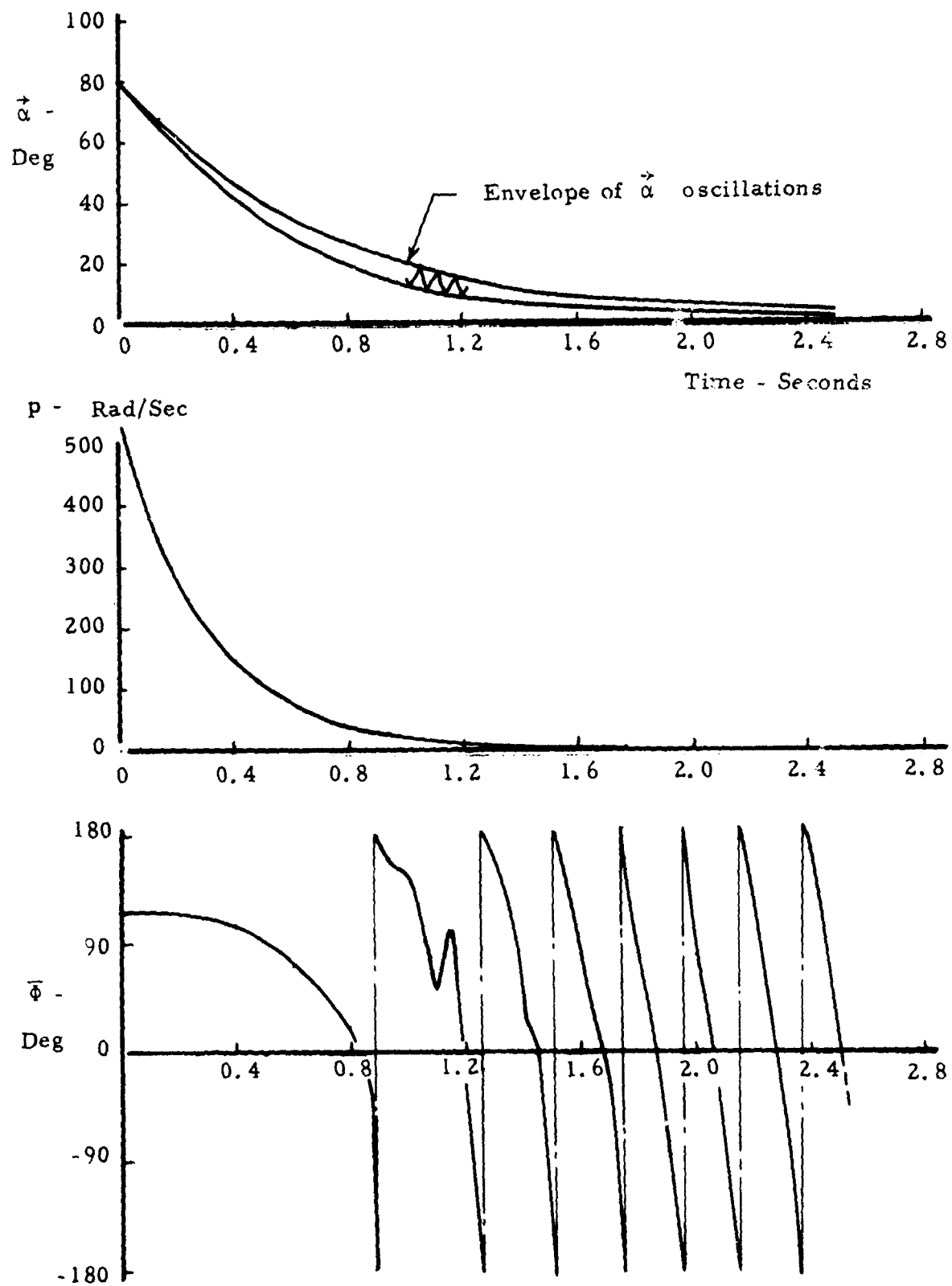
Figure 43. Motion Histories During Transition from
Glide-to-Ballistic Flight

Vane-Type Dual-Mode Bomblet (ζ = 45 degrees)

The effects of unintentional fin cant and longitudinal misalignment, on the transition dynamics of the vane-type dual-mode bomblet ($\zeta = 45$ degrees) have also been investigated. A small negative fin cant angle of 0.2 degree was introduced to determine the susceptibility to roll lock-in. The motion data are shown in Figure 44. Although the roll orientation of the body axes, ϕ, approaches a fixed value between 1.1 and 1.5 seconds, there is no corresponding tendency of the aerodynamic roll angle, Φ, to become constant (i.e., to lock-in). The lock-in is avoided, principally because of the finite counterclockwise coning motion during the 1.1- to 1.5-second time period. Thus, the change in angle of attack plane orientation has more effect on the time history of Φ than does the rolling motion.

The effect of longitudinal misalignment is most significant when the bomblet passes through or approaches a pitch-roll resonance condition. One resonant condition occurs during despin, and a second resonant condition occurs after despin, if the cant angle is large and negative. For a misalignment corresponding to $C_{m_o} = 0.05$ (1.25 degrees non-rolling trim) and a fin cant angle of -2.0 degrees, motion history data are presented in Figure 45. The motion histories of the angle-of-attack parameters do not reveal any large disturbances or extreme trim amplificatio: s, although resonance conditions were experienced for both positive and negative spin rates.

Both resonance periods are of short duration, the second being about 0.4 second. Thus, there is insufficient time for a noticeable change in the angle of attack due to trim amplification.

During the second resonance, there is a momentary roll lock-in, evidenced by the reversal in sign of $\dot{\Phi}$. This situation occurs at the second resonance because both the rolling and coning motions have the same direction and angular rate. There does not appear to be a noticeable effect of the side moment during the lock-in period.

Ballute-Stabilized Dual-Mode Bomblet   The transitional motion of the ballute-stabilized dual-mode bomblet is shown in Figure 46. A period of about 7 seconds is required for the angle of attack to decrease below 10 degrees, and the spin rate decays very slowly. However, the motion is well damped at all angles of attack, and there is practically no coning motion.

The trajectory and impact pattern characteristics of the dual-mode type bomblet have been evaluated for standard dispenser opening conditions III and IV, and for a high altitude vertical descent dispenser opening condition. For the first two conditions only the vane-stabilized dual-mode bomblet ($\zeta = 45$ degrees) was considered. The high altitude release condition was selected for investigation of the dispersion of the

72
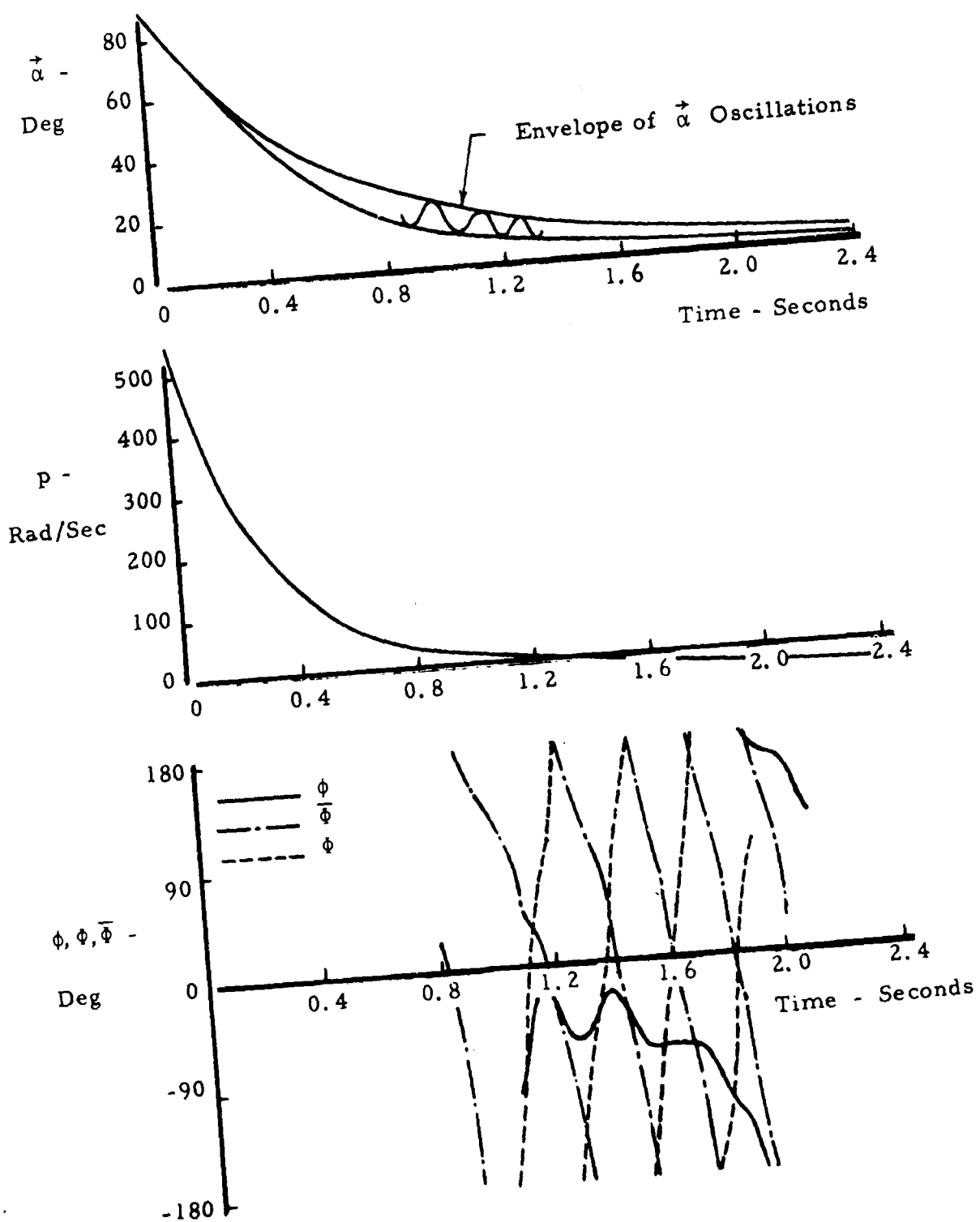
Figure 44. Effect of 0.2 Degree Negative Fin Cant on the Transitional Motion of a Vane-Type Dual-Mode Bomblet (ζ = 45 Degrees)

73
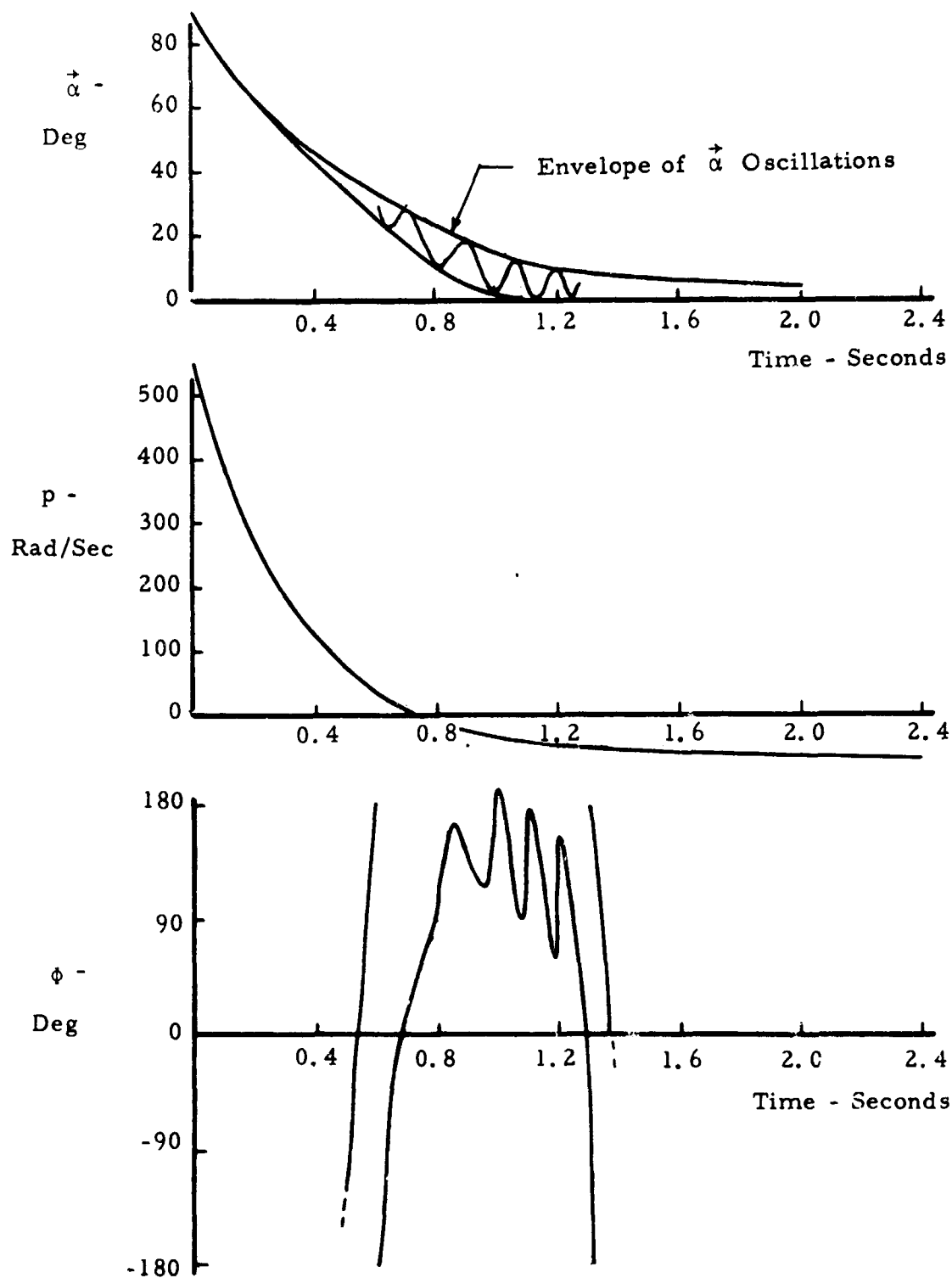
Figure 45. Effect of 2.0 Degrees Negative Fin Cant and
$C_{m_0} = 0.05$ on the Transitional Motion of a
Vane-Type Dual-Mode Bomblet (ζ = 45 Degrees)

74
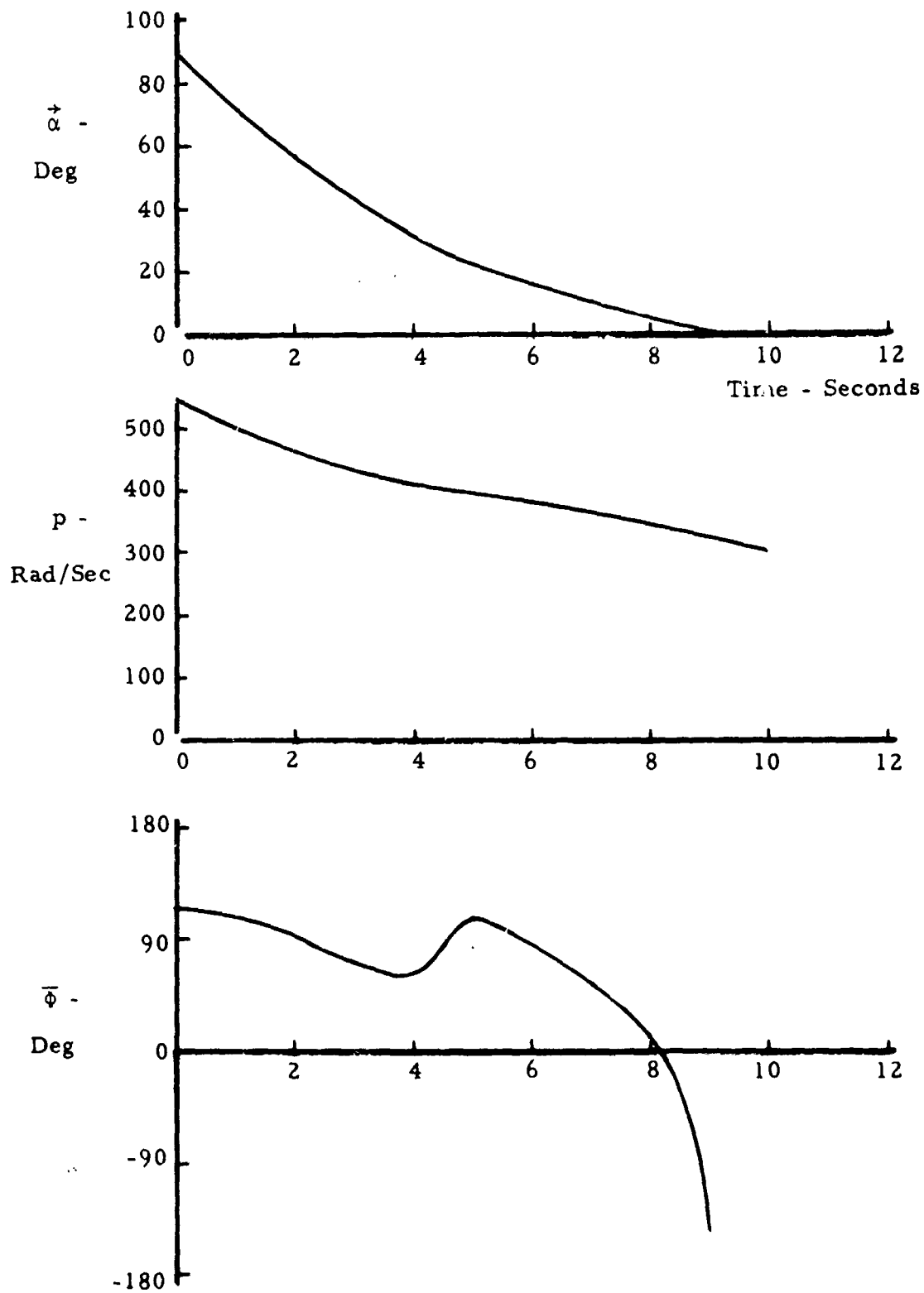
Figure 46.   Motion Histories During Transition from
Glide-to-Ballistic Flight

Ballute-Stabilized Dual-Mode Bomblet

75

Cross-Range - Ft

h - Ft

Magnus Rotor Dispersion Phase

Transition and Ballistic Flight

t = 4 Sec (Start of Transition)

Range - Ft
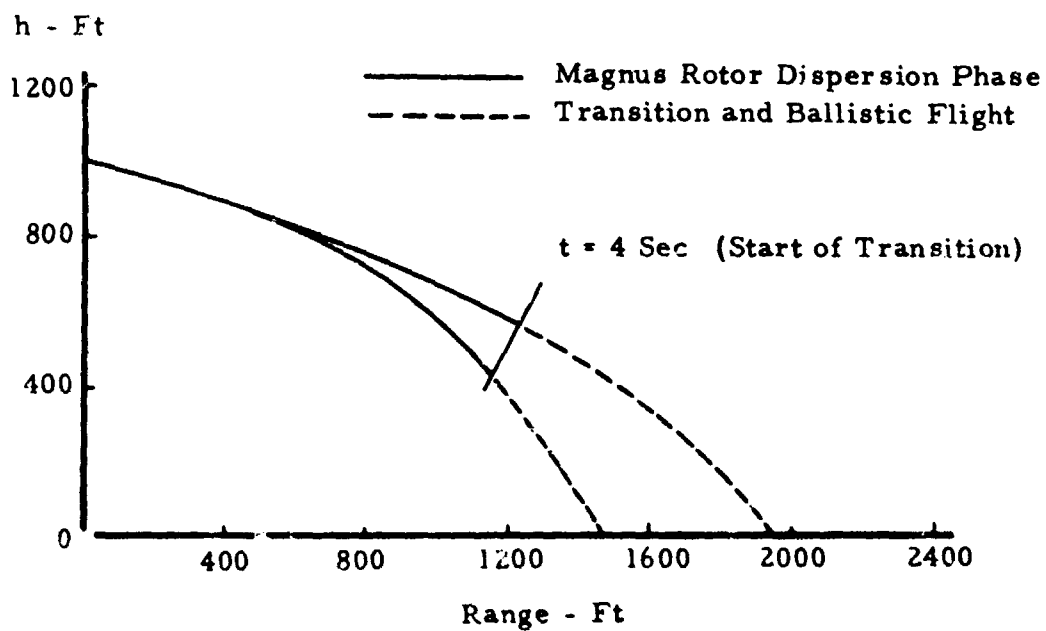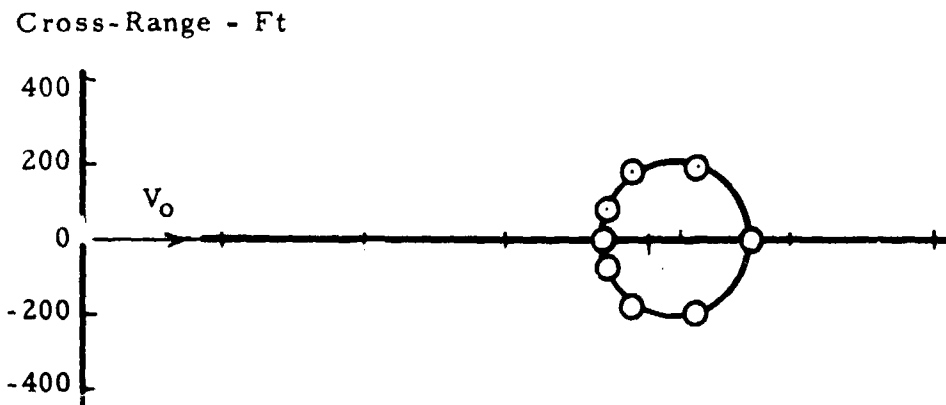
Figure 47.   Trajectory and Impact Boundary Data
for Vane-Stabilized Dual-Mode Bomblet

Dispenser Opening Conditions: h_o = 1000 ft,
V_o = 600 ft/sec, Y = 15 degrees
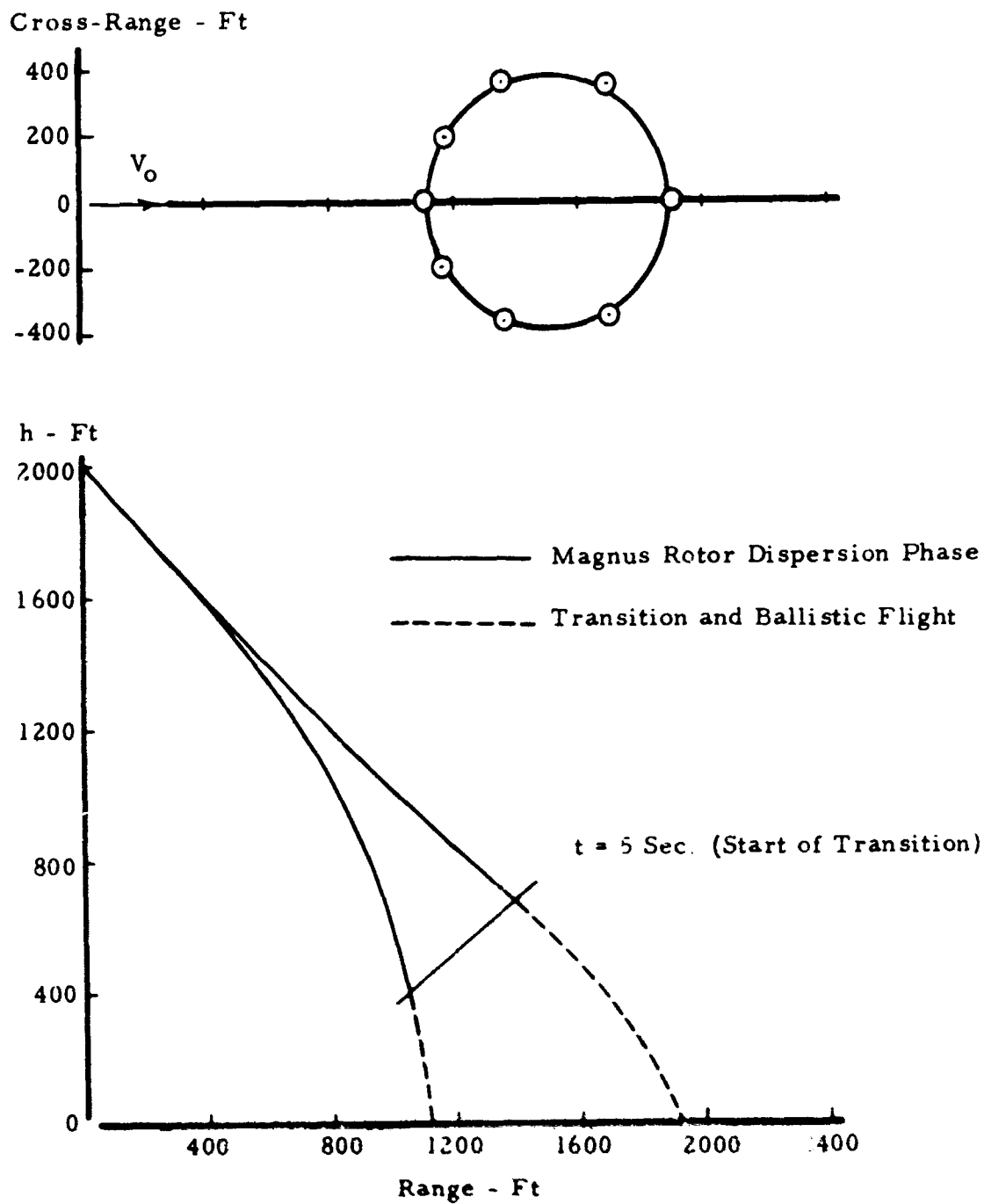
Figure 48. Trajectory and Impact Boundary Data
for Vane-Stabilized Dual-Mode Bomblet

Dispenser Opening Conditions: h_o = 2000 ft,
V_o = 900 ft/sec, Y = 45 degrees

77

Cross-Range - Ft

h - 1000 Ft

Magnus Rotor Dispersion Phase

Transition and Ballistic Flight

t = 15 Sec (Start of Transition)

Range - Ft
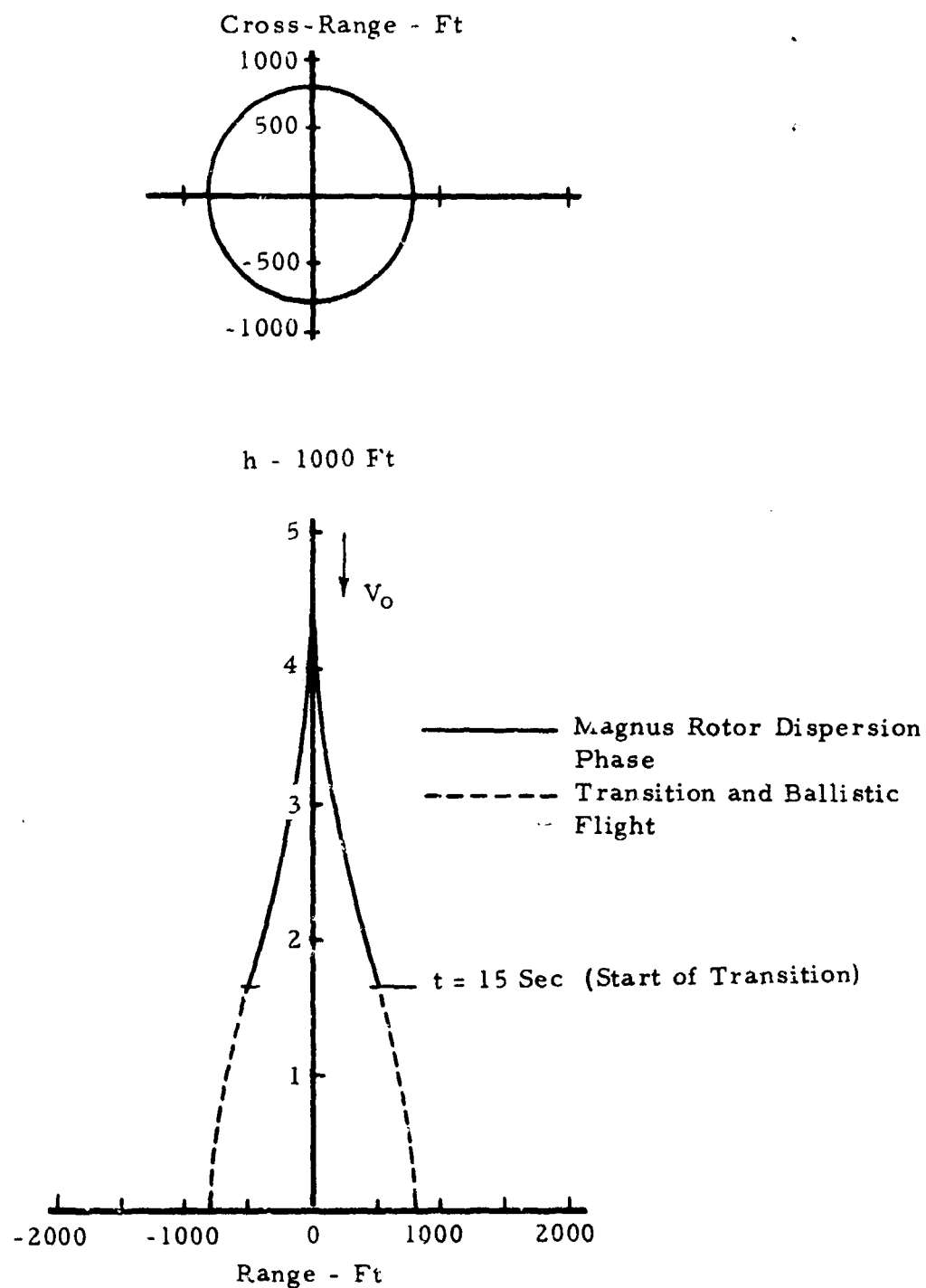
Figure 49. Trajectory and Impact Boundary Data for Ballute-Stabilized Dual-Mode Bomblet

Dispenser Opening Conditions: $h_o = 5000$ ft, $V_o = 400$ ft/sec, $\gamma = 90$ degrees

78

ballute-stabilized bomblet, because this bomblet requires a much greater time to complete transition from glide to ballistic flight.

The dispersion pattern at impact was approximated in the following manner. First a series of magnus rotor trajectories were computed, using the 6-DOF trajectory program, (3). The trajectories were initiated with the rotor at 90 degrees angle of attack. For the non-vertical release conditions, various initial orientations of the angle-of-attack plane were assumed. The resulting trajectories describe the near-maximum dispersion attainable during the magnus-rotor flight phase. At a fixed time after dispenser opening, the magnus-rotor trajectories were terminated. The starting time for glide-to-ballistic flight transition was selected such that the transition would be completed prior to impact, i.e., such that the bomblet angle of attack would be less than 10 degrees at impact. From the beginning of transition to impact, trajectory data were computed on the assumption of pure ballistic flight, using a constant drag coefficient representative of a fully deployed stabilizer.

The trajectory and impact pattern data for dispenser opening conditions III (h_O = 1000 feet, V_O = 600 ft/sec, γ_O = 15 degrees) and IV (h_O = 2000 ft, V_O = 900 ft/sec, γ_O = 45 degrees) are presented in Figures 47 and 48, respectively. For each of these release conditions the impact boundary is nearly circular. The impact pattern is about 400 feet in diameter for the 1000-foot release altitude and about 800 feet in diameter for the 2000-foot release altitude; thus, the pattern size increases in a nearly direct relation with the release altitude.

The dispersion characteristics of the ballute-stabilized dual-mode bomblet are shown in Figure 49 for a 5000 foot dispenser opening altitude, with vertically downward release velocity of 400 ft/sec. It will be noted that an impact pattern diameter of about 1600 feet is achieved.

D.   SPINNING-DISK BOMBLET

1.   Description of Concept.

The spinning-disk bomblet achieves dispersion both as a result of the aerodynamic magnus force (normal to disk axis) and the aerodynamic lift or side force (normal to the plane of the disk). The angular momentum of the disk prevents the body from pitching and yawing rapidly, and this tends to stabilize the orientation of the plane of incidence and the direction of the magnus and lift forces. It is sometimes useful to refer to this approach as the spin-stabilized incidence dispersion concept. The advantage of the disk shape, when applied to the spin-stabilized incidence concept, lies in the fact that the lift force remains large at high subsonic and supersonic

Mach numbers, whereas the magnus force becomes extremely small for all body shapes at Mach numbers above critical.

2. Background.

Previous studies of spinning disks during re-entry [for example, (12)], have shown that sizeable dispersion can occur even though the magnus force is not considered. Likewise, flight simulations of low-fineness ratio magnus rotors, with relatively large polar moments of inertia, have shown that the aerodynamic side force can contribute to the dispersion. Further, ballistic range tests of magnus rotors at supersonic velocities have revealed dispersions which cannot be attributed to the magnus force, but which appear to be related to the bomblet side force (13).

3. Disk Bomblet Configuration.

For the present investigation a 5.15-inch diameter elliptical cross-section disk-shaped bomblet was selected for investigation. Small vanes were added to the disk for the purpose of providing the required axial spin. The complete physical characteristics of the disk bomblet are described in Figure 50.

4. Aerodynamic Characteristics.

For computational purposes, the aerodynamic characteristics of the disk have been described using the aeroballistic notation of Appendix I. Subsonic and transonic values for the coefficients C_x, C_N, and C_m were obtained from (14) and (15). Figure 51 depicts the variations of C_L and C_m with disk incidence.

The dynamic coefficients were determined by use of slender-body theory and magnus rotor wind tunnel data and by consideration of the force and moment contributions of the vanes during rotational motion. These estimates are described in (16). The aerodynamic coefficients used for the 6-DOF simulations are summarized in Table IV.

5. Simulation Results.

The disk-bomblet dispersion characteristics have been evaluated for a representative cluster dispenser event condition as follows:

$$h_o = 2000 \text{ feet}$$

$$V_o = 900 \text{ ft/sec}$$

$$\gamma_o = 20 \text{ degrees}$$
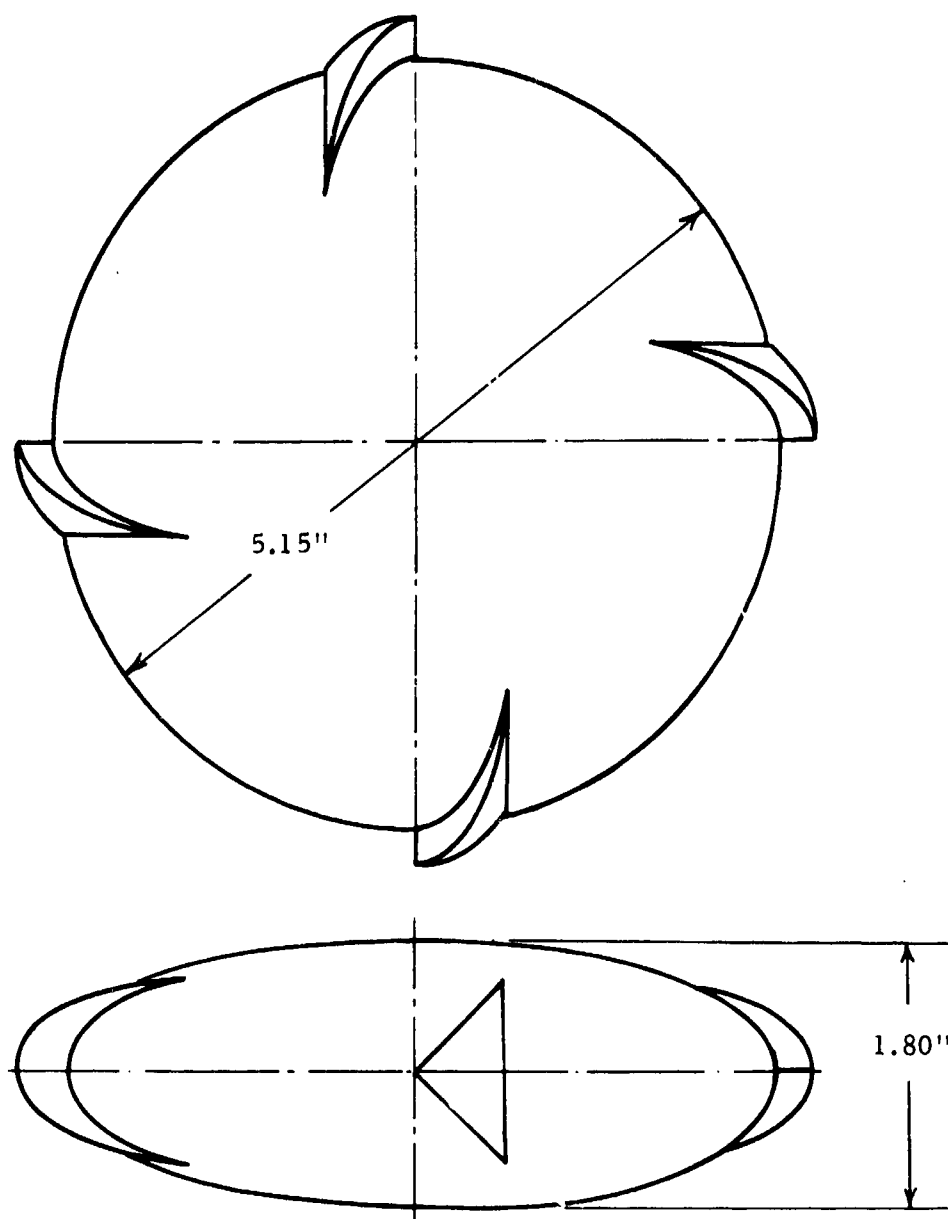
Physical Data

Weight $= 2.0$ pounds

$I_x = 1.145 \times 10^{-3}$ slug-ft^2

$I = 0.643 \times 10^{-3}$ slug-ft^2

Figure 50.   Disk-Bomblet Configuration

Figure 51. Lift and Pitching Moment Characteristics of Disk Bomblet

82

TABLE IV. AERODYNAMIC DATA SUMMARY: DISK BOMBLET

AEROBALLISTIC COEFFICIENTS

α ~ Degrees

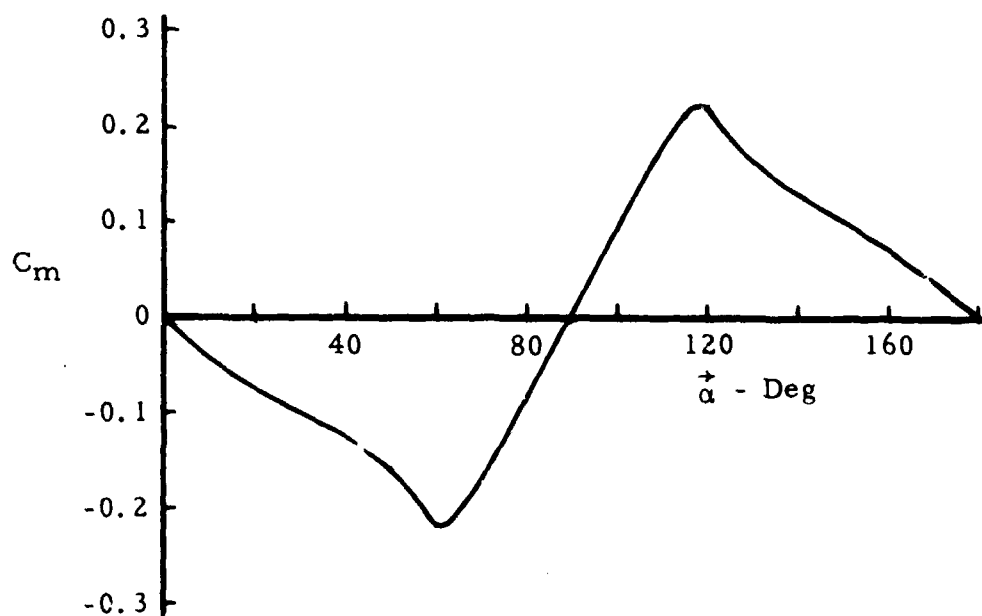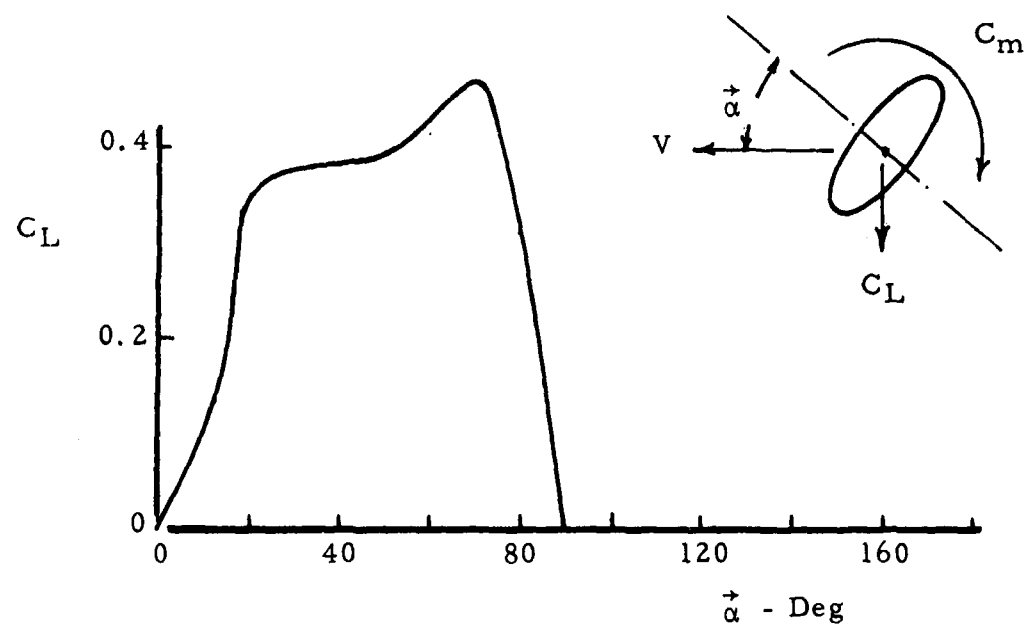| Coefficient	Mach Number	0	10	20	30	40	50	60	70	80	90	100	110	120	130	140	150	160	170	180
CX	0	-1.150	-1.151	-.981	-.850	-.755	-.610	-.580	-.5465	-.3415	0	.3415	.5465	.580	.610	.755	.850	.981	1.151	1.150
	0.6	-1.150	-1.151	-.981	-.850	-.755	-.610	-.580	-.5465	-.3415	0	.3415	.5465	.580	.610	.755	.850	.981	1.151	1.150
	0.9	-.985	-.950	-.935	-.900	-.810	-.690	-.540	-.380	-.205	0	.205	.380	.540	.690	.810	.900	.935	.950	.985
	1.2	-1.115	-1.075	-1.080	-1.010	-.940	-.845	-.780	-.600	-.290	0	.290	.600	.780	.845	.940	1.010	1.080	1.075	1.115
CN	0	0	.023	-.006	.087	.192	.168	.1735	.141	.153	.230	.153	.141	.1735	.168	.192	.087	-.006	.023	0
	0.6	0	.023	-.006	.087	.192	.168	.1735	.141	.153	.230	.153	.141	.1735	.168	.192	.087	-.006	.023	0
	0.9	0	.055	.090	.130	.160	.187	.198	.185	.173	.173	.173	.185	.198	.187	.160	.130	.090	.055	0
	1.2	0	.055	.090	.130	.170	.212	.265	.290	.295	.295	.295	.290	.265	.212	.170	.130	.090	.055	0
CM	0	0	-.036	-.070	-.101	-.127	-.162	-.220	-.175	-.095	0	.095	.175	.220	.162	.127	.101	.070	.036	0
	0.6	0	-.036	-.070	-.101	-.127	-.162	-.220	-.175	-.095	0	.095	.175	.220	.162	.127	.101	.070	.036	0
	0.9	0	-.033	-.062	-.086	-.102	-.110	-.122	-.107	-.060	0	.060	.107	.122	.110	.102	.086	.062	.013	0
	1.2	0	-.030	-.057	-.077	-.092	-.100	-.104	-.085	-.050	0	.050	.085	.104	.100	.092	.077	.057	.030	0
CMQ	0-1.2	-.1	-.1	-.1	-.1	-.1	0	0	0	0	0	0	0	0	0	-.1	-.1	-.1	-.1	-.1
CMR	0-1.2	-.1	-.1	.2	.2	.2	.2	.115	.035	-.050	-.125	-.050	.035	.115	.2	.2	.2	.2	-.1	-.1
CNPQ	0-1.2	0	0	0	0	0	0	0	0	0	0	0	0	0	0	0	0	0	0	0
CMPR	0-1.2	0	0	0	0	0	0	0	0	0	0	0	0	0	0	0	0	0	0	0
CNP*	0	0	.139	.274	.400	.515	.613	.694	.752	.788	.8	.788	.752	.694	.613	.515	.400	.274	.139	0
	0.6	0	.139	.274	.400	.515	.613	.694	.752	.788	.8	.788	.752	.694	.613	.515	.400	.274	.139	0
	0.9	0	0	0	0	0	0	0	0	0	0	0	0	0	0	0	0	0	0	0
	1.2	0	0	0	0	0	0	0	0	0	0	0	0	0	0	0	0	0	0	0
CLA*	0	.0200	.0200	.0200	.0200	.0200	.0200	.0200	.0200	.0200	.0200	.0200	.0200	.0200	.0200	.0200	.0200	.0200	.0200	.0200
	0.6	.0136	.0136	.0136	.0136	.0136	.0136	.0136	.0136	.0136	.0136	.0136	.0136	.0136	.0136	.0136	.0136	.0136	.0136	.0136
	0.9	.0105	.0105	.0105	.0105	.0105	.0105	.0105	.0105	.0105	.0105	.0105	.0105	.0105	.0105	.0105	.0105	.0105	.0105	.0105
	1.2	.0075	.0075	.0075	.0075	.0075	.0075	.0075	.0075	.0075	.0075	.0075	.0075	.0075	.0075	.0075	.0075	.0075	.0075	.0075
CLP*	0	-.0800	-.0800	-.0800	-.0800	-.0800	-.0800	-.0800	-.0800	-.0800	-.0800	-.0800	-.0800	-.0800	-.0800	-.0800	-.0800	-.0800	-.0800	-.0800
	0.6	-.0544	-.0544	-.0544	-.0544	-.0544	-.0544	-.0544	-.0544	-.0544	-.0544	-.0544	-.0544	-.0544	-.0544	-.0544	-.0544	-.0544	-.0544	-.0544
	0.9	-.0420	-.0420	-.0420	-.0420	-.0420	-.0420	-.0420	-.0420	-.0420	-.0420	-.0420	-.0420	-.0420	-.0420	-.0420	-.0420	-.0420	-.0420	-.0420
	1.2	-.0300	-.0300	-.0300	-.0300	-.0300	-.0300	-.0300	-.0300	-.0300	-.0300	-.0300	-.0300	-.0300	-.0300	-.0300	-.0300	-.0300	-.0300	-.0300
CMP*	0-1.2	0	-.020	-.033	-.0435	-.0425	-.0407	-.0387	-.033	-.023	0	.023	.033	.0387	.0407	.0425	.0435	.033	-.020	0

* $\dfrac{pd}{2V} = 0 - 1.0$

83

The disk bomblets were assumed to be randomly oriented in the warhead, and initial values of the angle-of-attack parameters were selected accordingly.

Figure 52 depicts typical transient motion data for a spinning-disk bomblet following release from the dispenser. The motion consists of a high-frequency nutation, with a peak-to-peak amplitude of about 15 degrees and a slow counterclockwise precession. The angle-of-attack history reveals that the disk configuration has a strong tendency to stabilize with spin axis normal to the flow. In this example, the bomblet angle of attack increases from an initial value of 33 degrees to 90 degrees in about two seconds. Because the disk lift force is maximum at an angle of attack of 70 degrees and zero at 90 degrees, the deflection of the trajectory, due to lift, also occurs within the first two seconds of flight.

Trajectory and impact data for several spinning-disk bomblets with random initial values of the angle-of-attack parameters are presented in Figure 53. It can be observed that flight-path dispersion occurs in two phases. The initial deflection of the trajectories begins at about 400-foot slant range and is a result of the lift force. Subsequently, the trajectories are deflected further by the magnus force but not necessarily in the same directions as the initial deflections occurred. The impact points, while not uniformly distributed, indicate a maximum dispersion pattern diameter of about 1800 feet.

More detailed study of the trajectory and motion data reveals that the lift force contributes only a small fraction of the total dispersion and that most of the dispersion results from the magnus force. The equivalent radial ejection velocity, corresponding to the initial deflection of the flight path by the lift force, is about 20 ft/sec.

The present results show the spin-stabilized incidence concept to be feasible, even though the dispersion achieved by this technique appears to be small, based on the aerodynamic input data utilized. The use of configurational asymmetry or axial displacement of the center-of-gravity, as a means of reducing the overturning moment in the angle-of-attack range for maximum lift, should be considered in future studies.

84
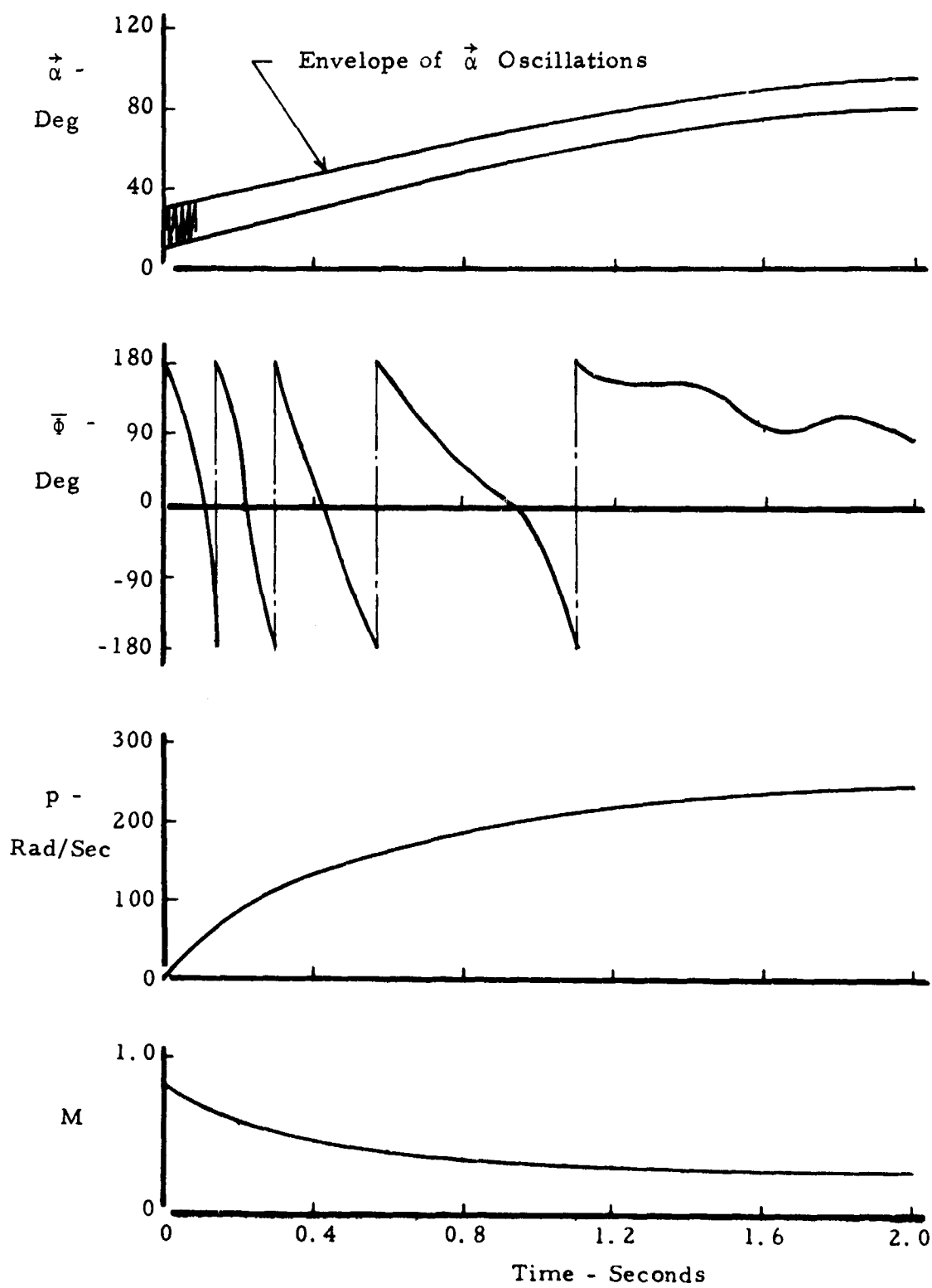
Figure 52. Transient Motion Data for Spinning-Disk Bomblet

85
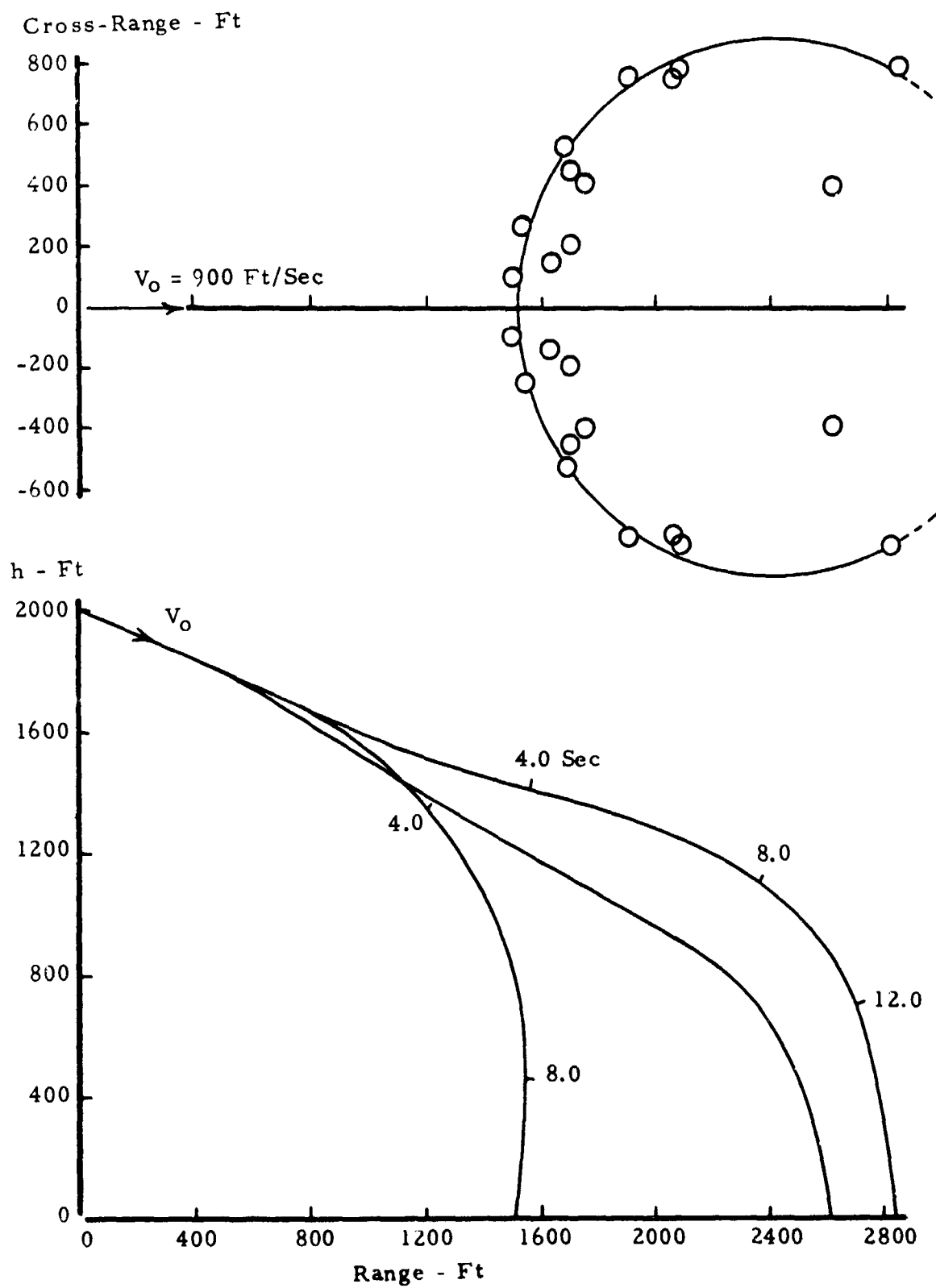
Figure 53.   Trajectory and Impact Data for Spinning-Disk Bomblet

86

SECTION III.

DISCUSSION AND COMPARISON OF
PROPOSED BOMBLET CONCEPTS

A.   DISPERSION AND AREA COVERAGE

Comparison of S-Curve and RT0 Bomblet Concepts   Of the four bomblet concepts investigated, the S-curve bomblet has the largest area coverage potential for low-altitude high-speed weapons delivery. S-curve bomblets manufactured to a high degree of precision (accidental fin cant equal or less than about 0.02 degree) can produce an impact pattern boundary exceeding 3500 feet in width for a dispenser functioning altitude of 300 feet. The roll-through-zero type bomblet can also provide extensive dispersion under low-altitude-high-speed delivery conditions, and a pattern width in excess of 800 feet can be realized when the design roll-torque coefficient is 0.0005.

Direct comparison of the S-curve and RT0 bomblet requires consideration of the allowable asymmetries and misalignments. For example, comparison of the data from Figures 18 and 33, for dispenser opening condition II, shows that the S-curve and RT0 bomblets have about the same area coverage, if the S-curve bomblet fin cant is of the order of 0.5 degree, and the fin cant of the RT0 bomblet is 0.23 degree, (C_{l_0} = .0015). If the S-curve bomblet has a 0.5-degree misalignment of two opposing fins (C_{m_0} or C_{n_0} = 0.004), the area coverage is less than that of the RT0 bomblet.

Considering a fin cant angle of 0.1 degree for the S-curve bomblet, which is a realistic magnitude of fin cant for test bomblets*, it will be noted from Figure 54 that the impact pattern boundaries for the S-curve bomblet have dimensions which are about twice those of the RT0 bomblet impact patterns with C_{l_0} = 0.0005.

Dual-Mode and Disk Bomblet Comparisons   For high speed delivery, the vane-stabilized dual-mode bomblet requires dispenser opening altitudes in excess of 1000 feet to permit both effective dispersion and transition from magnus-rotor to ballistic flight. For a 2000-foot delivery altitude (dispenser opening condition IV), the dual-mode bomblet dispersion is compared with the S-curve and RT0 bomblets in Figure 55. For this condition, both the dual-mode and RT0 bomblets have impact patterns about 800 feet in diameter. For higher delivery altitudes, the area coverage of the dual-mode

---

* Measurements made by The Weapons Research Establishment [17] on a group of test bomblets have indicated a mean cant angle of 0.09 degree, with 0.077 degree standard deviation.
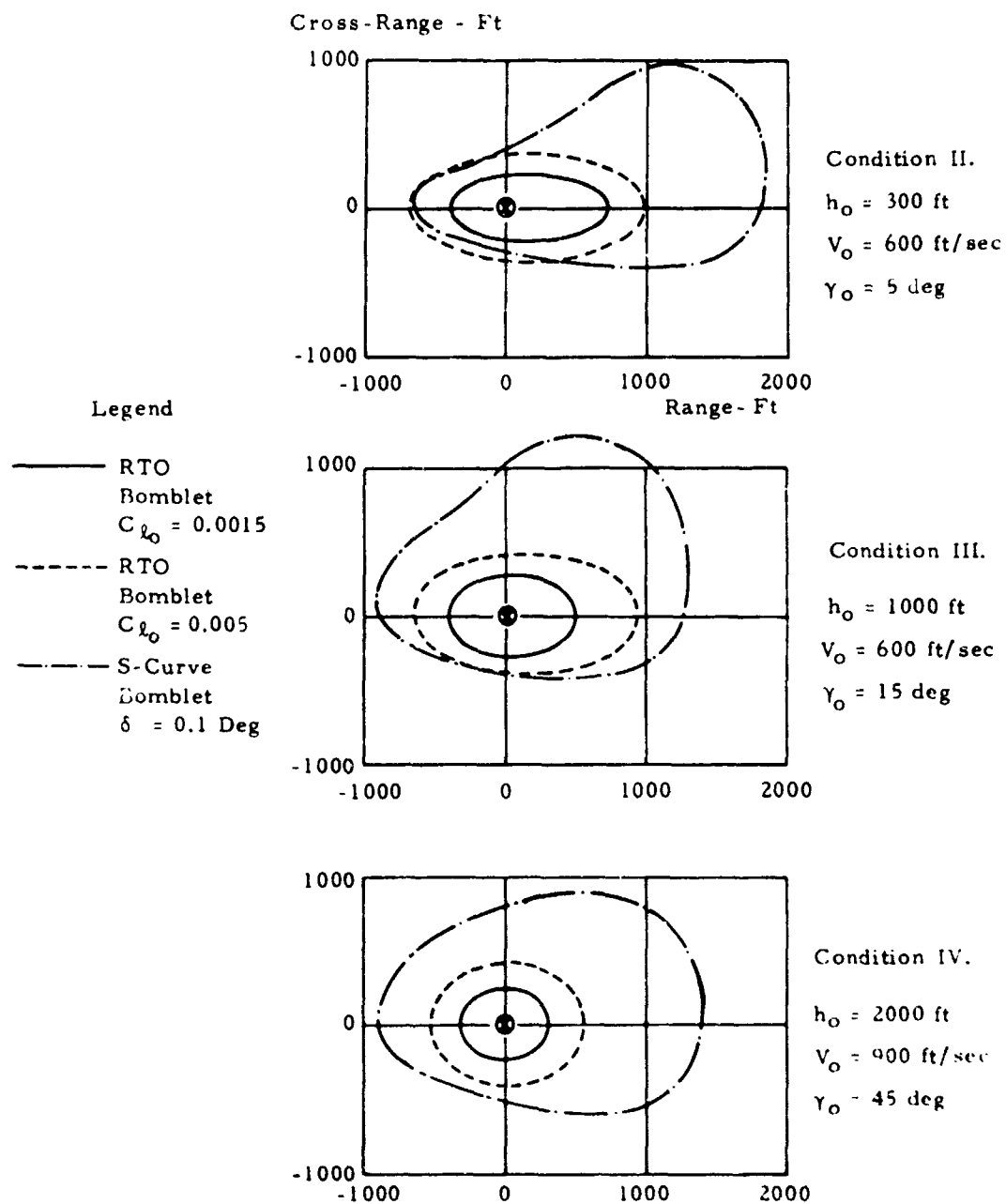
Figure 54. Comparison of Impact Area Coverage Capability of S-Curve and RTO Bomblets for Dispenser Opening Conditions II, III, and IV

88

Cross-Range - Ft

Range - Ft
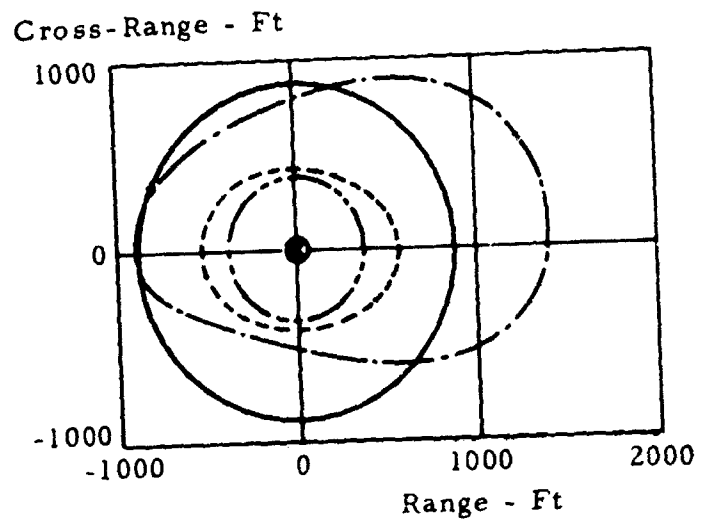
Legend

——————— Disk Bomblet

—..——..— Dual-Mode Bomblet (Vane Stabilized; ζ = 45 Deg)

-------- RT0 Bomblet (C_{ℓ_o} = 0.0005)

—.——.— S-Curve Bomblet (δ = 0.01 Deg)

Figure 55. Comparison of Area Coverage Capability of S-Curve, RT0, Dual-Mode, and Disk Bomblets for 900 ft/sec Release Velocity at 2000 Feet Altitude

bomblet will become progressively greater and will eventually exceed that of either the S-curve or RT0 bomblets.

Figure 55 also shows, for comparison, the impact dispersion boundary for the disk bomblet, which is about 1800 feet in diameter. The disk bomblet dispersion is approximately equal to that of the S-curve bomblet for the delivery conditions indicated. As noted previously, the disk bomblet impact dispersion is only slightly influenced by the disk lift force.

Comparison of Proposed Concepts with Radial Force Ejection Systems. Figure 56 compares the S-curve and RT0 bomblet dispersion with the area coverage capability of a zero-lift bomblet dispersed by a radial-force-ejection system. For trajectory computations, the zero-lift bomblet is assumed to have a ballistic coefficient matching that of the S-curve and RT0 bomblets. Ejection velocities of 50 and 100 ft/sec are considered for the radial-force-ejection system.

As can be seen from the data, the radial-force-ejection system is most effective for low-speed and low-altitude delivery conditions. Considering a dispenser opening velocity of 300 ft/sec, for example, a radial ejection velocity of 50 ft/sec results in greater area coverage than that obtained with either the S-curve or RT0 bomblets.

However, at high-speed dispenser opening conditions, both the S-curve and RT0 bomblets are capable of impact patterns larger than those obtainable using an ejection velocity of 100 ft/sec.

Comparison of Proposed Bomblet Concepts with BLU-26/B Magnus-Rotor. The dispersion performance of the CBU-24 munition (BLU-26/B magnus-rotor bomblet and SUU-30 type dispenser) has been extensively investigated (18) for delivery conditions approximating those considered in this report. A comparison of the area coverage of the proposed bomblets with that of the BLU-26/B is illustrated in Figure 57.

For dispenser opening condition III, the BLU-26/B dispersion pattern has an outer diameter of about 800 feet. This pattern size is greatly exceeded by the S-curve type bomblet, while the RT0 bomblet exhibits about the same size pattern for a roll torque coefficient of $C_{l_o} = 0.0005$. The dispersion achieved with the dual-mode bomblet, for dispenser opening condition III, is about one-half that of the BLU-26/B.

The disk bomblet impact dispersion is comparable to that of the BLU-26/B, when allowance is made for the effect of the flight path angle at dispenser opening. The latter comparison is illustrated in Figure 57(C).
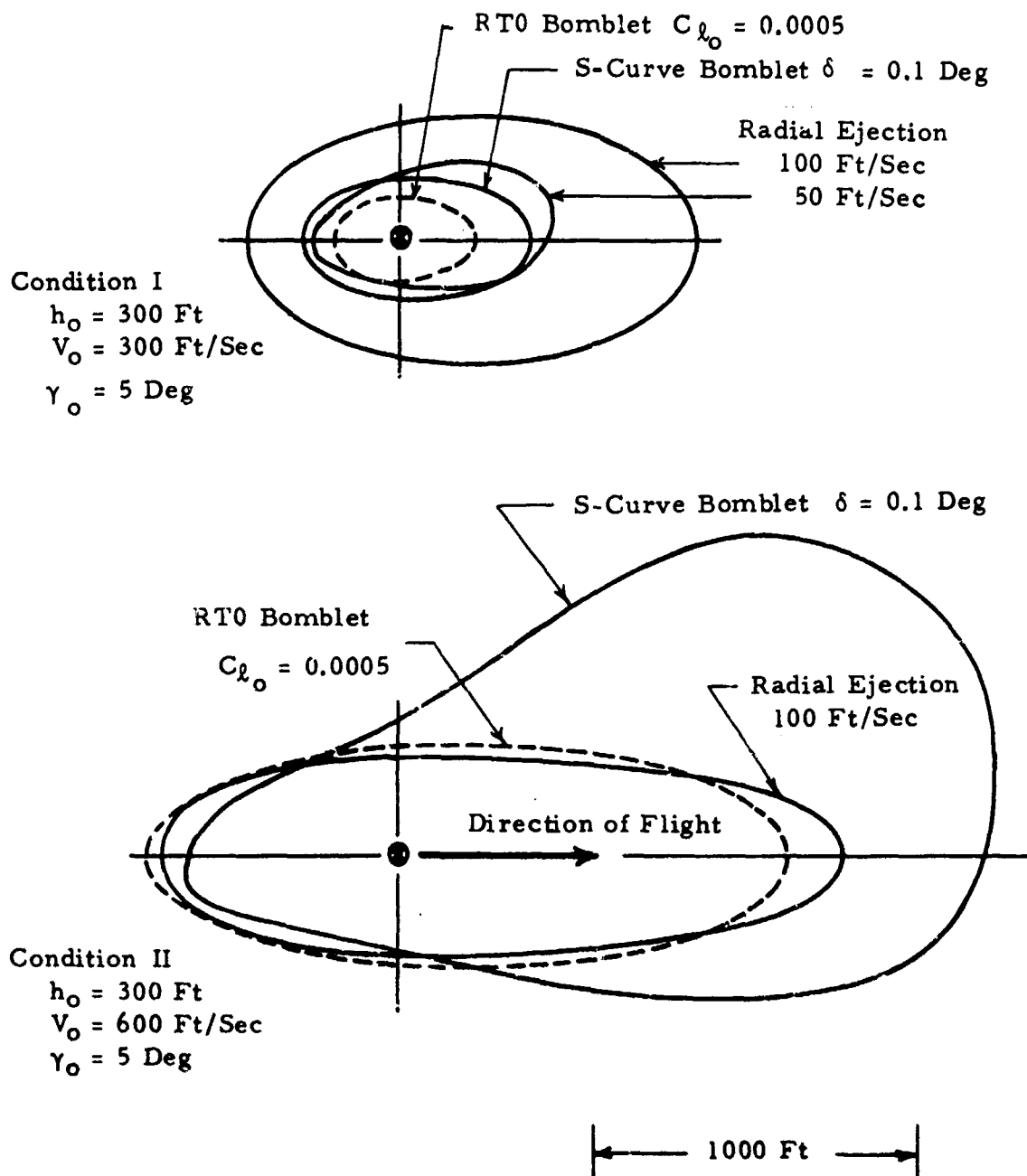
Figure 56. Comparison of S-Curve and RT0 Bomblet Dispersion with Area Coverage Capability of Force Ejection System

Condition III
h_o = 1000 Ft
V_o = 600 Ft/Sec
γ_o = 15 Deg

Condition IV
h_o = 2000 Ft
V_o = 900 Ft/Sec
γ_o = 45 Deg

Figure 56. (Continued)

A)

Condition III.

h_o = 1000 ft

V_o = 600 ft/sec

γ_o = 15 deg

Legend

———— BLU-26/B
SUU-30 Dispenser

—·—·— S-Curve
Bomblet
δ = 0.1 Deg

——————— RTO Bomblet
C_{ℓ_o} = 0.0005

——·——· Dual-Mode
Bomblet

—·—··— Disk
Bomblet

B)

Condition IV.

h_o = 2000 ft

V_o = 900 ft/sec

γ_o = 45 deg

Cross-Range - Ft

C)

h_o = 2000 ft

V_o = 900 ft/sec

γ_o = 20 deg

Range - Ft
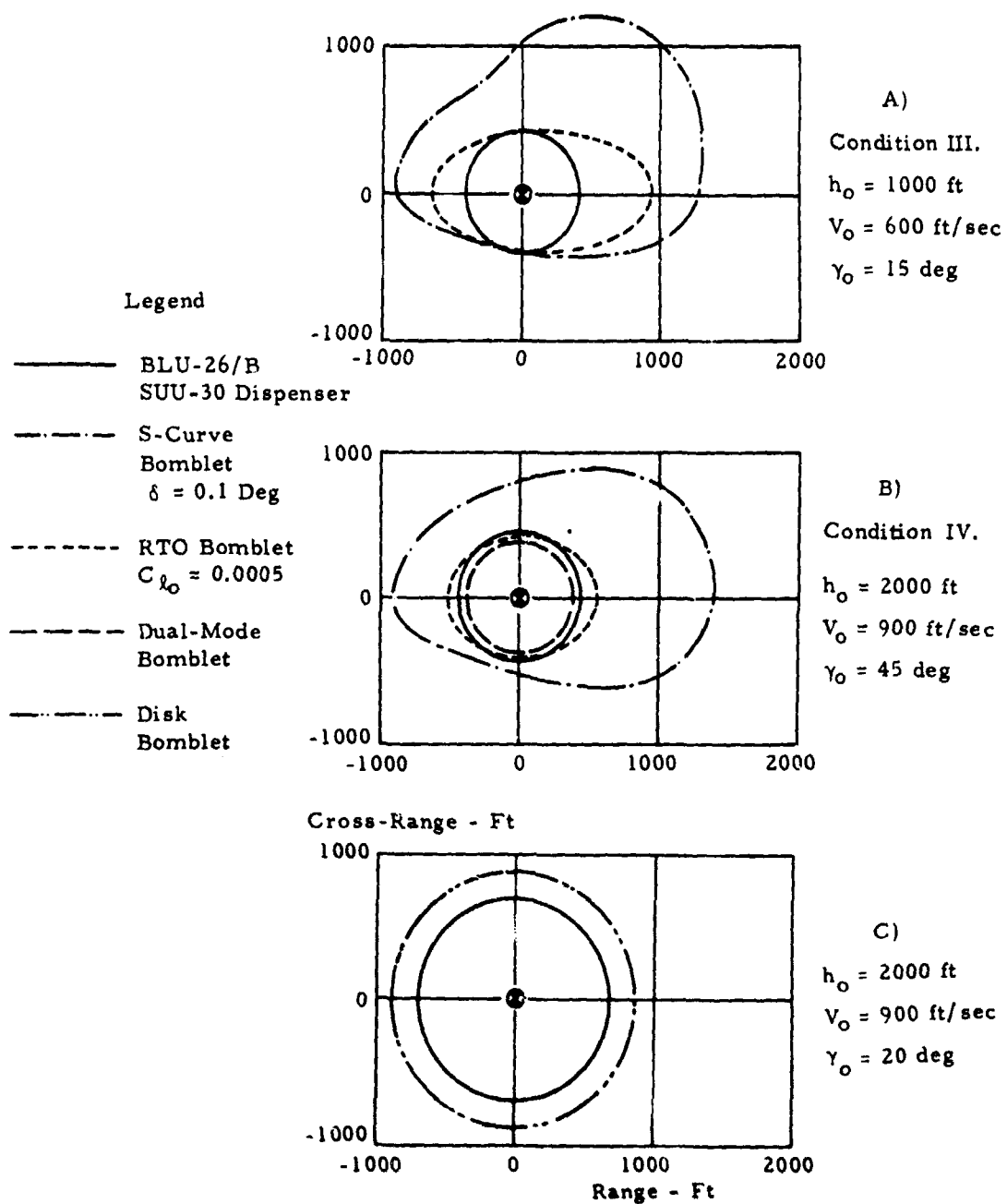
Figure 57.   Comparison of Area Coverage Capability of S-Curve,
RTO, Dual-Mode, and Disk Bomblet with BLU-26/B
Magnus Rotor Performance

93

Effect of Delivery Velocity and Mach Number. The dispersion of the S-curve-type bomblet is extremely sensitive to velocity and Mach number effects. With increasing velocity and dynamic pressure, the aerodynamic lateral force becomes larger, thus increasing the dispersion. At the same time, the spin rate increases with velocity, and if the accidental cant is large enough, the spin rate will exceed the critical spin rate. This will result in coning motion and reduced dispersion. In addition to the above effects, the S-curve bomblet lift can change appreciably with Mach number due to the sensitivity of the stability and trim angle of attack to Mach number.

The RT0 bomblet dispersion is essentially independent of the delivery velocity, except as it modifies the distance between release and impact. The aerodynamic stability, trim, and roll dynamics of this bomblet are only slightly affected by velocity and Mach number.

The effect of velocity and Mach number on the dual-mode bomblet dispersion will be the same as for any other magnus rotor. The altitude and time required for transition from magnus-rotor flight to ballistic flight is almost invariant, since this flight phase occurs after the rotor has decelerated to nearly constant velocity.

The effect of velocity and Mach number on the disk-bomblet dispersion has not been determined since only one delivery condition was investigated.

Effect of Delivery Altitude. The impact dispersion of the S-curve and RT0 bomblets is not significantly influenced by dispenser opening altitude for the range of delivery conditions investigated. The dual-mode bomblet dispersion increases linearly with altitude, for altitudes above the minimum altitude required for magnus-rotor-to-ballistic-flight transition. This minimum altitude is about 250 feet for the vane-stabilized dual-mode bomblet if transition is initiated from steady-state gliding flight.
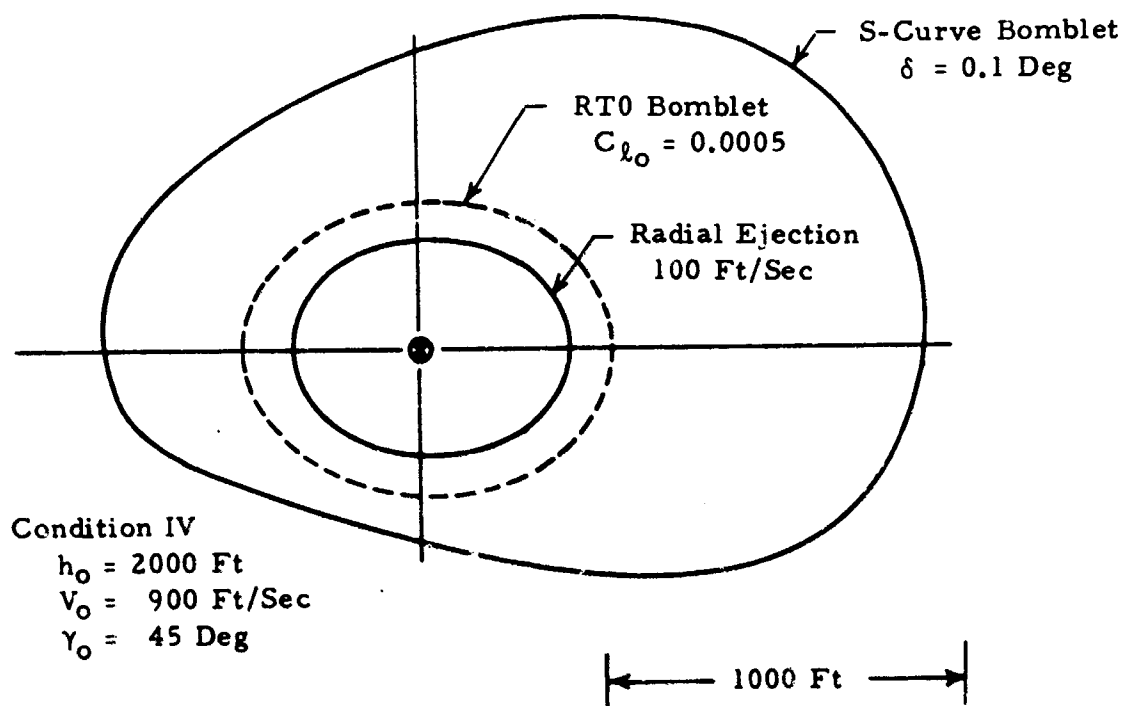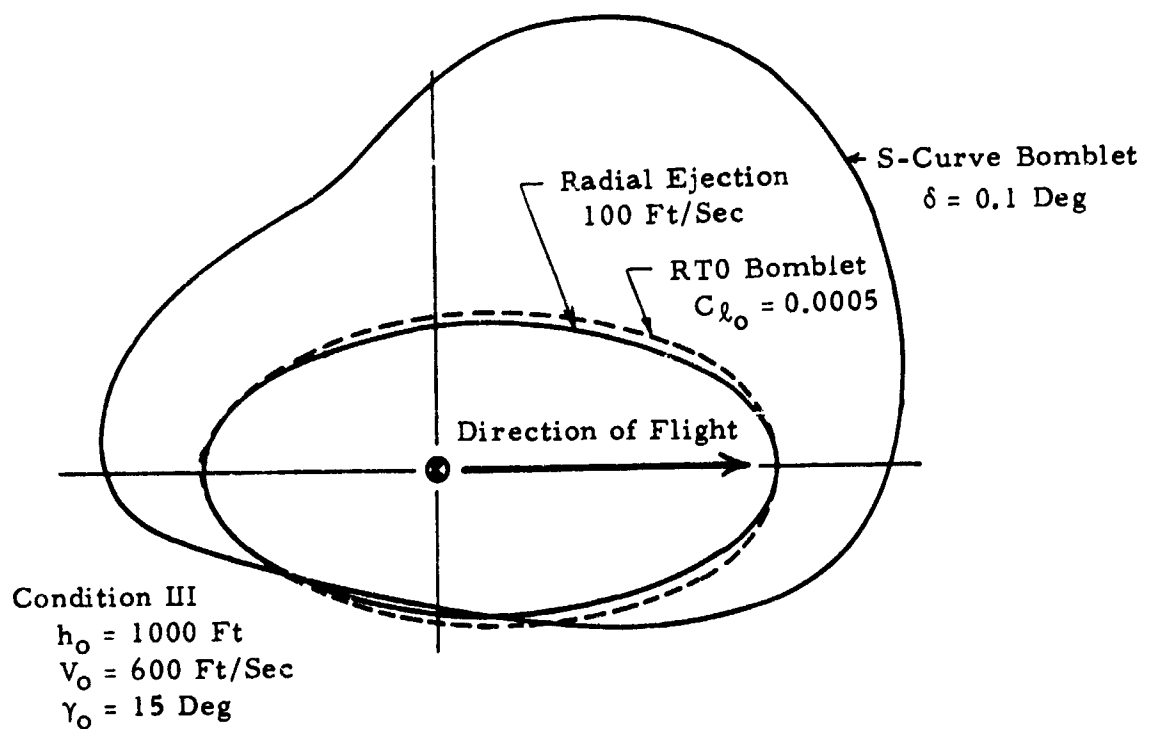

B. IMPACT PATTERN CHARACTERISTICS

The motion theories and results from the 6-DOF simulations provide some indication of the manner in which bomblet impact points will be distributed with the respective boundary curves.

1. S-Curve Bomblet Impact Pattern Characteristics.

Assuming that the S-curve bomblets in a particular dispenser have a wide range of fin cant angles, the impact pattern will resemble the sketch below and will be comprised of an inner elliptical-shaped core

(representing bomblets with spin rates above critical) and a wide fan of sparse impact points, extending forward of the ballistic impact center (representing bomblets with spin rates less than critical). The fraction of bomblets in the central elliptical core will increase when the bomblets have large longitudinal misalignments. The density of impacts at the extreme rear and narrow portion of the pattern will be relatively high, because bomblets will impact in this area regardless of whether their spin rate is small or large. If the S-curve bomblet asymmetries are extremely small, the impact points will form a single annular ring, roughly matching the predicted pattern boundary for subcritical spin rates.

Sketch of Probable Impact Pattern
for S-Curve Bomblet

V_o

Sparse
Impacts

Concentrated
Impacts

Greatest
Concentration
of Impacts
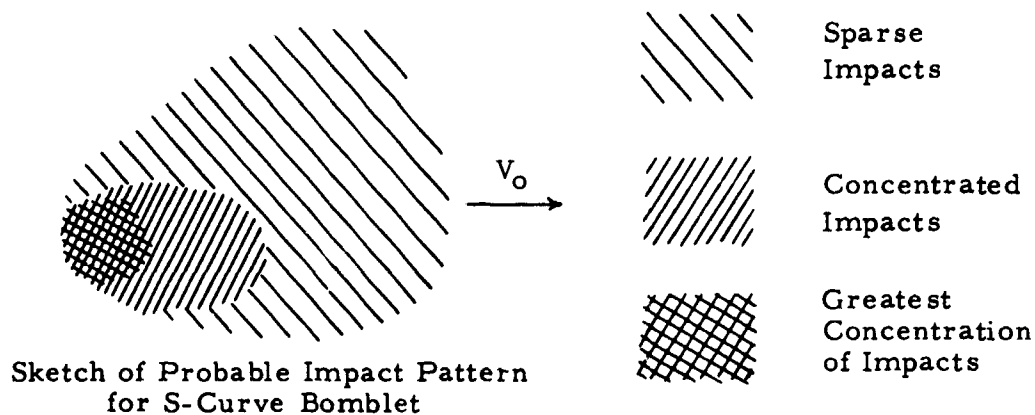
2.   RT0 Bomblet Impact Pattern Characteristics.

The impact pattern of the roll-through-zero type bomblet could have a distribution of impact points not unlike that sketched below:

Sketch of Probable Impact Pattern
for RT0 Bomblet

V_o

Sparse
Impacts

Concentrated
Impacts

95
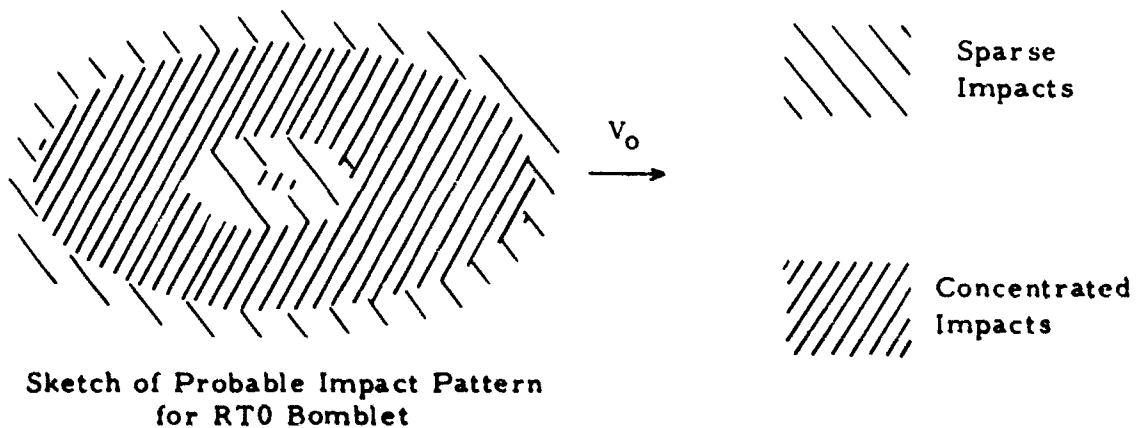
The pattern is comprised of a wide annulus, containing the impact points of all bomblets whose roll torque (or fin cant) deviation from the mean is less than some standard statistical measure, such as 1σ . Inside the annulus will be the impact points of those bomblets which have roll torque deviations exceeding the statistical measure, as well as the bomblets which have roll torques of the same sense as the dispenser roll. The latter bomblets will have poor dispersion and will impact near the pattern center.

The fraction of interior impact points can be increased or decreased by a change in the mean roll torque. This provides the designer with a possible means of impact pattern control.

Dual-Mode Bomblet and Disk Bomblet. The dual-mode and disk bomblets will have impact pattern distributions characteristic of magnus rotors in general. A discussion of magnus-rotor impact pattern distributions is beyond the scope of the present endeavor.

C.   DISCUSSION OF FACTORS AFFECTING BOMBLET PERFORMANCE

1.   Sensitivity to Manufacturing Tolerances.

The dispersion of the S-curve type bomblet is particularly sensitive to configurational asymmetries and manufacturing tolerances. The trim angle of attack (of the bomblet considered in Section II) varies about one degree for each 0.027 caliber shift in the longitudinal center-of-gravity. An accidental fin cant of 0.1 degree significantly reduces the maximum dispersion at release velocities of 600 ft/sec or greater. Fin and body misalignments resulting in values of C_{m_0} greater than about 0.005 (C_{m_0} = C_{n_0} = 0.005 corresponds to about one-half degree incidence of two opposing fins) can result in coning and an attendant reduction in area coverage.

The roll-through-zero type bomblet is sensitive only to the roll torque. All sources of roll torque, other than the design (or built-in) roll torque, cause erratic flight behavior. In addition to the aerodynamic-induced moment, there exists the possibility of spurious roll torques due to the combined effects of lateral center of gravity offset and a trimmed normal force. The maximum value of the roll moment due to lateral c. g. offset should not exceed the design rolling moment. For the basic wingless RTO bomblet, the allowable c. g. offset for a design roll torque coefficient of 0.0015 is given by

$$\Delta y/d = \frac{C_{\ell_0}}{C_{N_{TRIM}}} = \frac{0.0015}{0.55} \doteq 0.0027 \tag{10}$$

For the 3-inch-diameter bomblet, $\Delta y = 0.08$ inch.

The 6-DOF motion simulations, for the vane-stabilized dual-mode bomblet, show that the transition dynamics of this configuration are not degraded by accidental fin cant or longitudinal misalignment.

Small asymmetries should not appreciably affect either the aerodynamics or the transitional motion of the ballute-stabilized dual-mode bomblet.

2. Sensitivity to Launch Environment.

The impact point of an S-curve type bomblet depends significantly on the initial orientation of the angle-of-attack plane. Therefore, if the dispenser has an angle of attack at time of functioning, the impact pattern will be heavily biased, i.e., all of the bomblets will tend to impact in the same area, even though the dispersion from the ballistic impact point is large. The biasing effect due to dispenser angle of attack will be greatest when the bomblets are aligned with the dispenser. On the other hand, random perturbations in the initial values of the motion parameters ($\vec{\alpha}$, p, q, r, etc.) will alter the impact locations of individual bomblets but will not influence the pattern size or distribution of impact points.

A uniformly distributed impact pattern for the RT0 bomblet depends primarily upon random orientation of the bomblet trim vector, and therefore, the motion of this type bomblet is influenced less by the dispenser angle of attack. Large angle-of-attack perturbations at launch would be detrimental to RT0 bomblets possessing a sizeable induced roll moment at large angles of attack.

3. Scale Effects.

The dispersion of the S-curve type bomblet is a function, principally, of the ratio of the aerodynamic lift to bomblet weight. For a particular bomblet-fineness ratio and trim lift coefficient, dispersion will be inversely proportional to the loading parameter W/S. Changes in bomblet geometry and inertia will modify the critical spin rate in accordance with Equation (3).

The theoretical dispersion of the RT0 bomblet is proportional to $\frac{1}{m'} \sqrt{I_x'}$. Thus, the RT0 bomblet can be scaled up or down in size without affecting dispersion, provided the m' and I_x' parameters remain constant.

The dispersion of the dual-mode type bomblet is significantly affected by the scaling of the magnus-rotor configuration. The spin-up or

97

spin-down time constant for the scaled bomblet is proportional to the product of the geometric scale factor and the non-dimensional inertia ratio $\bar{I}_x{}'/I_x{}'$, where $\bar{I}_x$ represents the scaled bomblet. Thus, an increase in magnus-rotor size increases the time for spin-up or spin-down and conversely.

D.   CONFIGURATION SELECTION AND OPTIMIZATION

1.   S-Curve Bomblet.

Optimization of the S-curve type bomblet for maximum dispersion is best achieved by increasing the critical spin rate and decreasing the allowable fin cant. The former requires the selection of configurations which have large damping and a small magnus moment coefficient, while the latter depends primarily upon the accuracy of bomblet fabrication. For high-speed delivery, the bomblet must possess a finite trim angle of attack throughout the flight Mach number range. The use of large trim angles of attack, as a means of improving dispersion, appears ill advised. Operation at large angles of attack will, in many instances, lead to undesirable roll characteristics and an increased magnus moment.

The S-curve pitching moment characteristics should be attainable for a wide variety of bomblet geometries, provided proper attention is paid to the effects of nose shape, afterbody shape, fineness ratio, and fin size. For supersonic operation, spike-nose configurations can also be considered since they have nonlinear S-curve-type moment characteristics.

2.   RT0 Bomblet.

Optimization of the RT0-type bomblet for maximum dispersion requires that the induced aerodynamic roll torques be minimized, while concurrently providing a large trimmed normal force. The present effort has shown that the use of planar lifting surfaces is detrimental because their adverse roll characteristics more than offset the increased normal force. The results of the present studies suggest the use of configurations with a high degree of axial symmetry (many fins or ring tail) as a means of decreasing or eliminating the roll-induced aerodynamic moments.

Although desirable, a high-fineness-ratio slender body does not appear to be necessary. For example, the blunt-nose 4-caliber-length configuration has a normal force slope which is about 75 percent that of the elliptical-nose 6-caliber finned bomblet.

3. Dual-Mode Bomblet.

The factors which must be given greatest consideration in the aerodynamic design of the dual-mode type bomblet are the spin damping and magnus moment coefficients. The magnus moment coefficient at large angles of attack must have a positive value if transition is to occur rapidly.

The dual-mode bomblet concept is, for practical purposes, limited to cylindrical bodies with fineness ratios less than 2.0, because of magnus-rotor stability considerations.

The use of a ballute stabilizer, larger in size than that investigated in this study, appears feasible, and could make the ballute-stabilized dual-mode bomblet more suitable for low-altitude weapon delivery.

The mechanics and dynamics of stabilizer deployment are significant problem areas requiring extensive future design and test efforts.

4. Disk Bomblet.

Motion simulation and aerodynamic data for the disk bomblet are presently insufficient for optimization of this concept.

SECTION IV.

WIND TUNNEL INVESTIGATIONS

A. TEST PROGRAM

In support of the present effort, a comprehensive wind tunnel test program was accomplished in the 4T transonic tunnel at the Arnold Engineering Development Center. The test plan and model configurations were specified by the contractor. Model design and fabrication, including the necessary support and drive systems, were provided by AEDC, through special arrangement with the Air Force Armament Laboratory.

The test program was conducted in three phases. The first phase consisted of static force and moment measurements, in both pitch and roll, for the S-curve, roll-through-zero, and dual-mode bomblet models. These tests were accomplished for a Mach number range of 0.3 - 1.2, except for the dual-mode bomblet which was evaluated only at Mach 0.3 and 0.5. In addition, limited tests were accomplished at three different Reynolds numbers.

In the second phase a forced-oscillation balance was used for measurement of the planar pitch-damping of the S-curve bomblet models from Mach 0.3 to 1.2. *

The third test phase provided both roll dynamics data for the roll-through-zero and dual-mode bomblet models and magnus data for the S-curve and dual-mode bomblet models. A special hydraulic drive system, with pneumatically operated clutch and braking system, was provided for the S-curve and dual-mode bomblet tests. The third phase tests for the S-curve and RT0 bomblet models were accomplished from Mach 0.3 to 1.2, while the dual-mode bomblet model tests were accomplished only at low speed.

B. S-CURVE BOMBLET CONFIGURATIONS

The seven S-curve bomblet models utilized for the AEDC tests are depicted in Figure 58. In addition, three body-alone configurations $(B_S N_{S1} A_{S1}$, $B_S N_{S2} A_{S1}$, and $B_S N_{S2} A_{S2})$ were evaluated. The model configurations were selected for the purpose of determining the aerodynamic

---

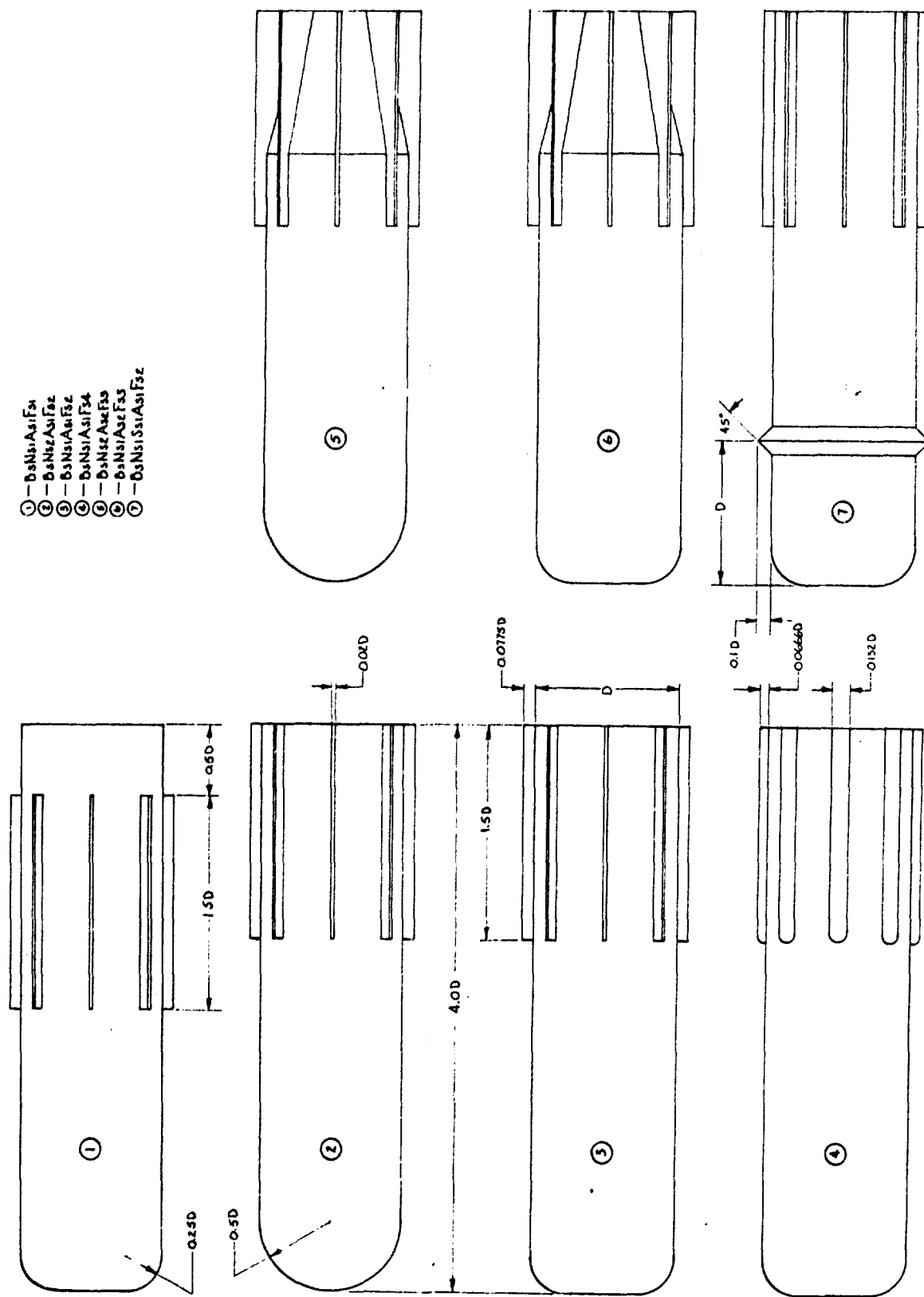* The boattail models could not be tested because of sting interference effects.

Figure 58. S-Curve Bomblet Model Configurations for AEDC Wind Tunnel Tests

101

effects of nose-shape, afterbody-shape, fin location, fin cross-section, and a nose spoiler ring. The latter two configuration modifications were of interest primarily from the standpoint of spin damping and magnus characteristics.

All S-curve bomblet models were 3.0 inches in diameter.

C.   RT0 BOMBLET CONFIGURATIONS

The RT0 Bomblet model is depicted in Figure 59. The RT0 bomblet concept was evaluated both in the body-alone and wingless configurations. The effect of the wings was determined for incidence angles of 10 degrees and 20 degrees. Three configuration modifications were employed as a means of providing a design roll torque: differential wing incidence, a wing roll tab, and asymmetrical body indentations.

The RT0 bomblet models were 3.0 inches in diameter.

D.   DUAL-MODE BOMBLET CONFIGURATIONS

The vane-stabilized dual-mode bomblet model is shown in Figure 60. The dual-mode bomblet models had the same geometry as the bomblets depicted in Figure 37, and the body diameter of each model was 3.0 inches.

E.   STATIC TEST RESULTS

The AEDC test report describing the static wind tunnel tests is being published separately as (4). Supplementary plots of the test data showing the effects of angle of attack, Mach number, Reynolds number, and aerodynamic roll angle are available[19]. The latter reference also presents a breakdown of the normal force and pitching moment characteristics of the S-curve and RT0 bomblets, showing the contributions of the fins and wings.

S-Curve Bomblet Aerodynamic Data. The variation of the pitching moment with angle of attack for each of the various S-curve bomblet configurations is shown in Figure 61 for Mach 0.3 and 0.9. At Mach 0.3, all of the configurations, except that with the nose spoiler, exhibit the characteristic S-shaped pitching moment curve. The trim angles of attack range from four degrees to as much as 22.5 degrees at low speed. The trim angle-of-attack variation with Mach number is shown in Figure 62. The moment
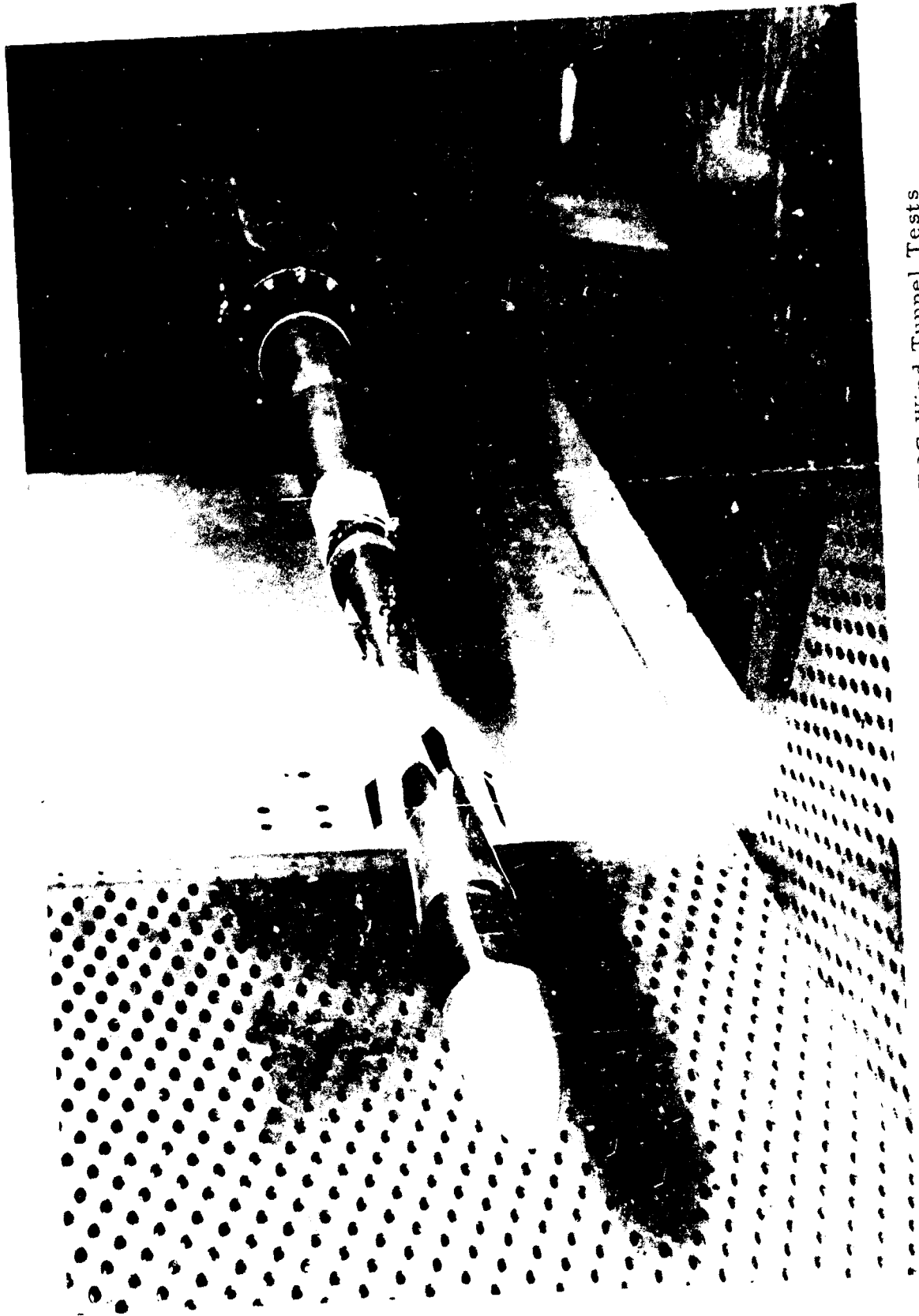
Figure 59. RT0 Bomblet Model Configuration for AEDC Wind Tunnel Tests

Figure 60. Vane-Stabilized Dual-Mode Bomblet Model

104

$\vec{a}$ - Deg

M=0.3

24

20

16

12

8

4

-4

-8

-0.3   -0.2   -0.1   0.1   0.2   0.3

C_m

B_SN
B_SN
B_SN
B_SN
B_SN
B_SN
B_SN

M = 0.9

B

$S_1 A_{S1} F_{S2}$
$S_2 A_{S1} F_{S2}$
$S_1 A_{S2} F_{S3}$
$S_1 A_{S1} F_{S1}$
$S_1 A_{S1} F_{S4}$
$S_1 S_{S1} A_{S1} F_{S2}$
$S_2 A_{S2} F_{S3}$

$\vec{\alpha}$ - Deg

20

16

12

8

4

C_m

-0.3   -0.2   -0.1   0.1   0.2

-4

-8
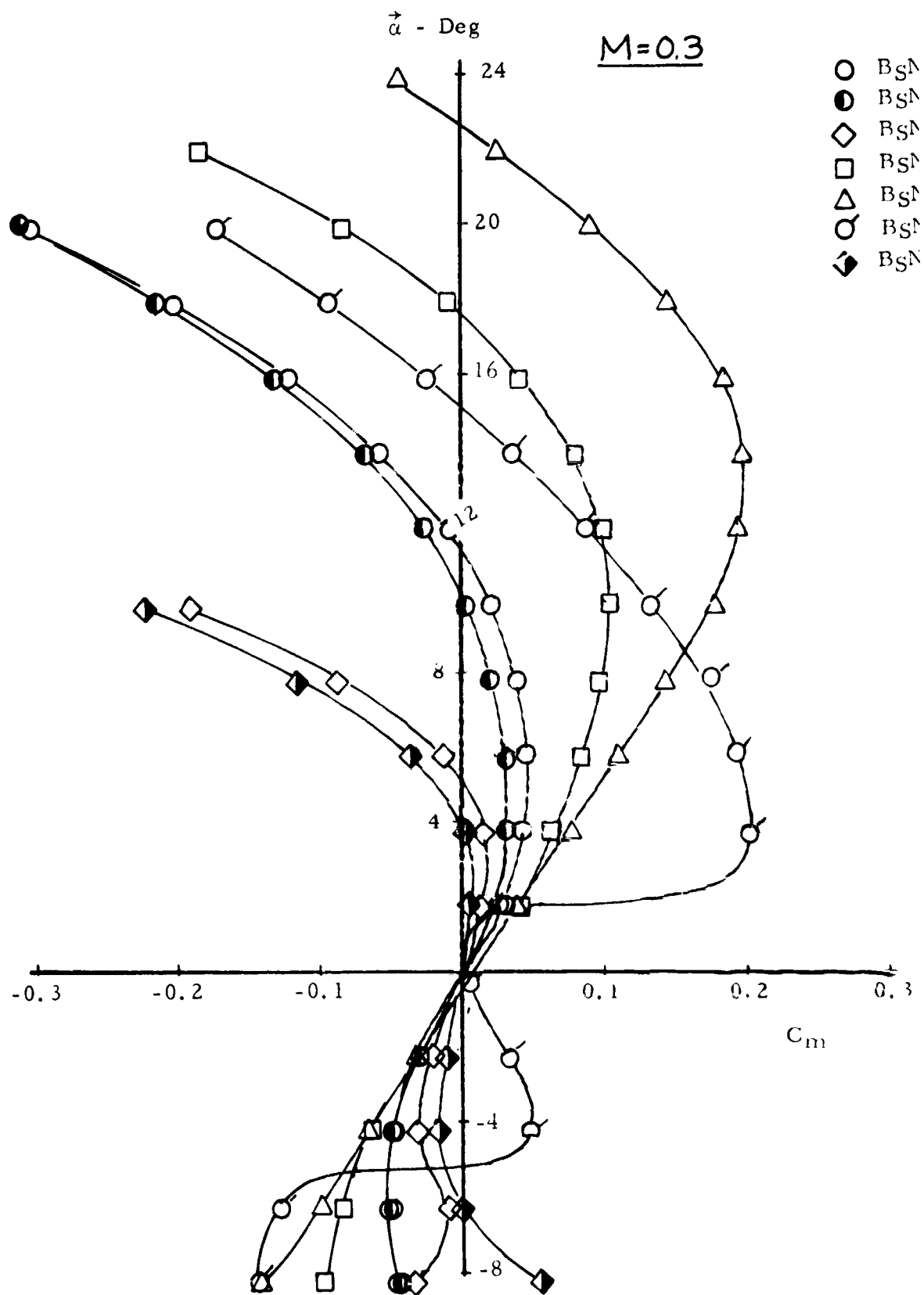
Figure 61.   Pitching Moment Characteristics of S-Curve Bomblet Models
as Determined from AEDC Static Wind Tunnel Tests

105

(The reverse of this page is blank)
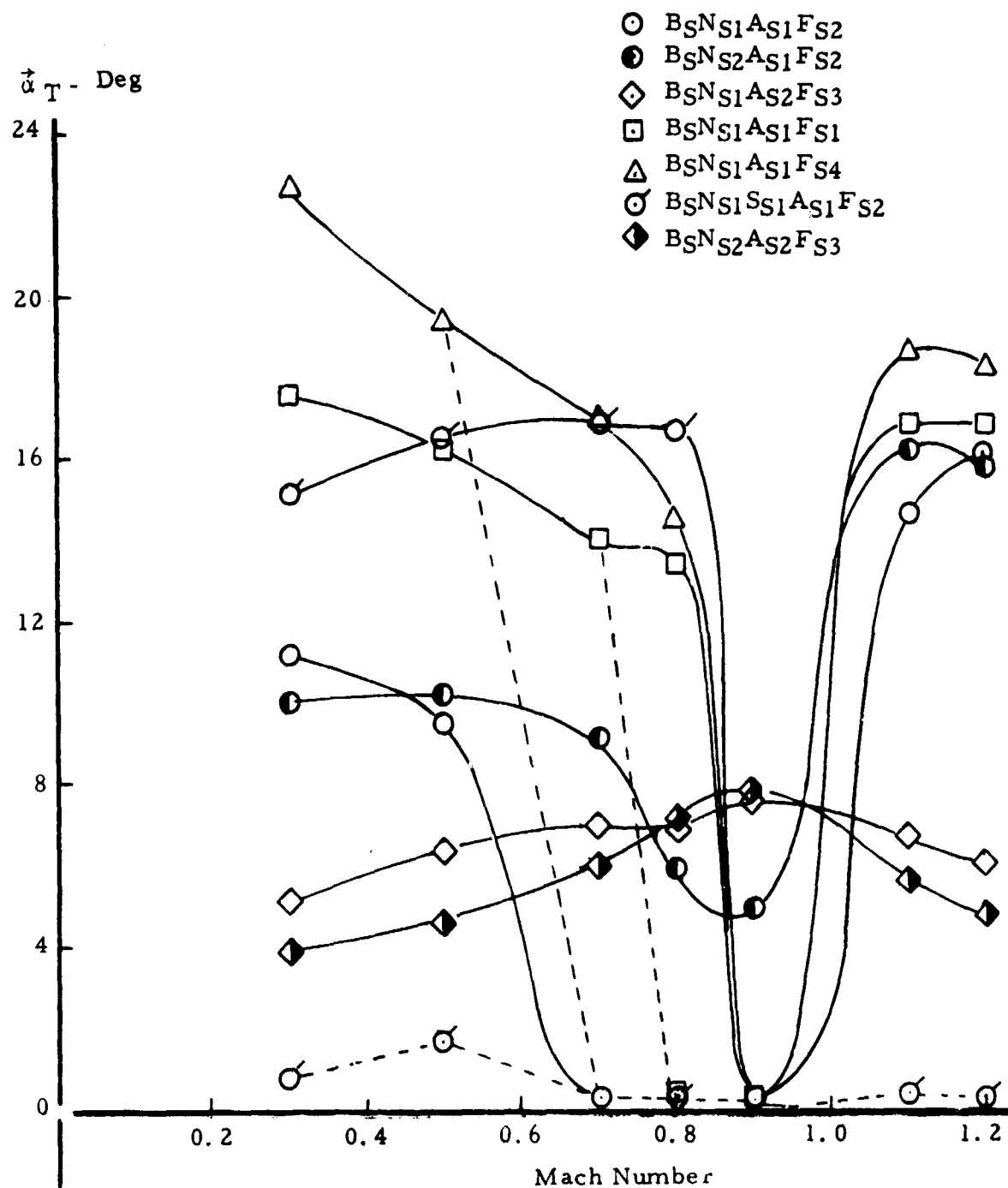
Figure 62.   Trim Characteristics of S-Curve Bomblet Models as
Determined from AEDC Static Wind Tunnel Tests

107

reference center is 1.5 calibers aft of the bomblet nose for all of the config-
urations. Two different types of trim characteristics are noted: the boattail
afterbody models exhibit an increase in trim angle of attack in the transonic
range, while all of the other configurations display a large decrease in the
trim angle of attack at transonic conditions. Of the cylindrical afterbody
configurations, only configurations $B_SN_{S2}A_{S1}F_{S2}$ has a non-zero trim angle
of attack at Mach 0.9. The observed transonic trim changes for the cylin-
drical afterbody models is due, principally, to the increase in body-alone
stability at small angles of attack. The decrease in transonic stability of
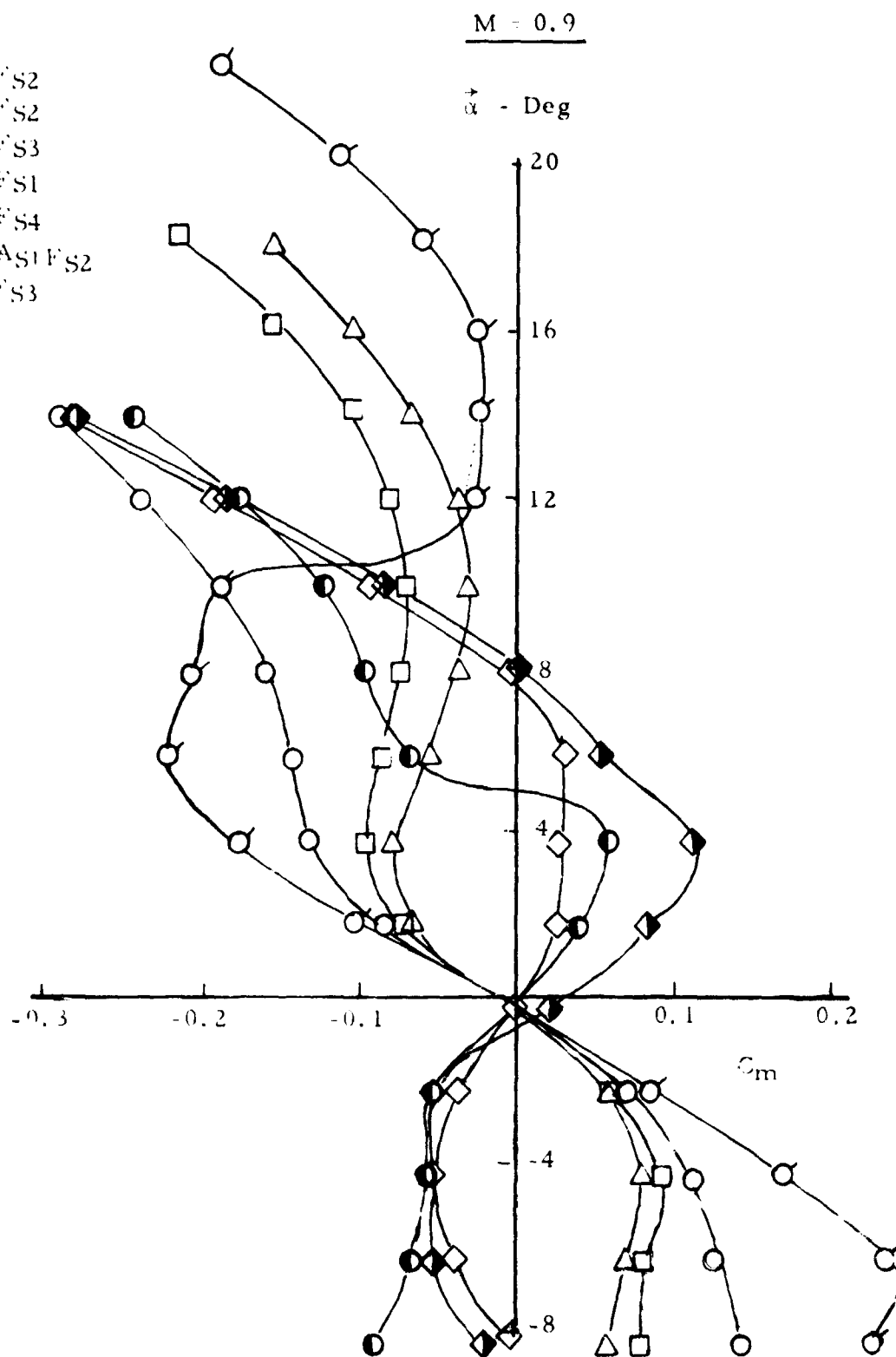the boattail models results from a loss in fin effectiveness, since the change
in stability is not reflected by the body-alone data. At transonic conditions
(M = 0.9) the blunt nose greatly increases the stability at angles of attack
below 4 degrees, while at large angles the blunt nose is destabilizing.

The normal force coefficient characteristics of the seven basic
configurations are presented in Figure 63 for Mach 0.3 and 0.9. In the
low Mach number range, the boattail afterbody models display the largest
normal force slopes, probably due to the fact that these models have a
larger exposed fin area. The drag coefficient variation with Mach number
for each configuration is plotted in Figure 64. At low speeds, the boattail
afterbody models have about one-half the drag of the basic cylindrical after-
body models.

RTO Bomblet. The pitching moment characteristics of the RTO
bomblet models, for a moment reference point 2.6 calibers aft of the body
nose, are presented in Figure 65. These data are for Mach 0.3 and are
typical of the results obtained at all of the test Mach numbers.

The body-plus-fins configuration, $B_{R1}F_{R2}$, exhibits a stable
moment curve which is approximately linear at small angles of attack but
with an increasingly stable slope at large angles of attack. With the wing
attached at incidence, the pitching moment becomes highly nonlinear and
the slope is unstable at positive angles of attack less than six degrees. The
destabilizing effect of the wing at small angles of attack had been anticipated
due to wing-vortex fin interference, but the measured data exhibit a greater
instability than had been predicted using (20). These results necessitated
a forward center-of-gravity movement in order to achieve the desired trim
angle of attack of eight degrees.

The normal force data for Mach 0.3 are shown in Figure 66. With
the wing attached at 10 degrees incidence, the normal force at eight degrees
angle of attack is about 1.1, while the body-fin configuration produces a
normal force coefficient of 0.58 at this angle of attack.

Zero-lift drag coefficient data for the RTO bomblet configurations
are presented in Figure 67.

$\vec{\alpha}$ - Deg

M = 0.3

C_N

$B_S N_{S1} A_{S1} F$
$B_S N_{S2} A_{S1} F$
$B_S N_{S1} A_{S2} F$
$B_S N_{S1} A_{S1} F$
$B_S N_{S1} A_{S1} F$
$B_S N_{S1} S_{S1} A$
$B_S N_{S2} A_{S2} F$

Figure 63. ... ... orce Characteristics of S-Curve Bomblet Models
... ... mined from AEDC Static Wind Tunnel Tests

(The reverse of this page is blank)
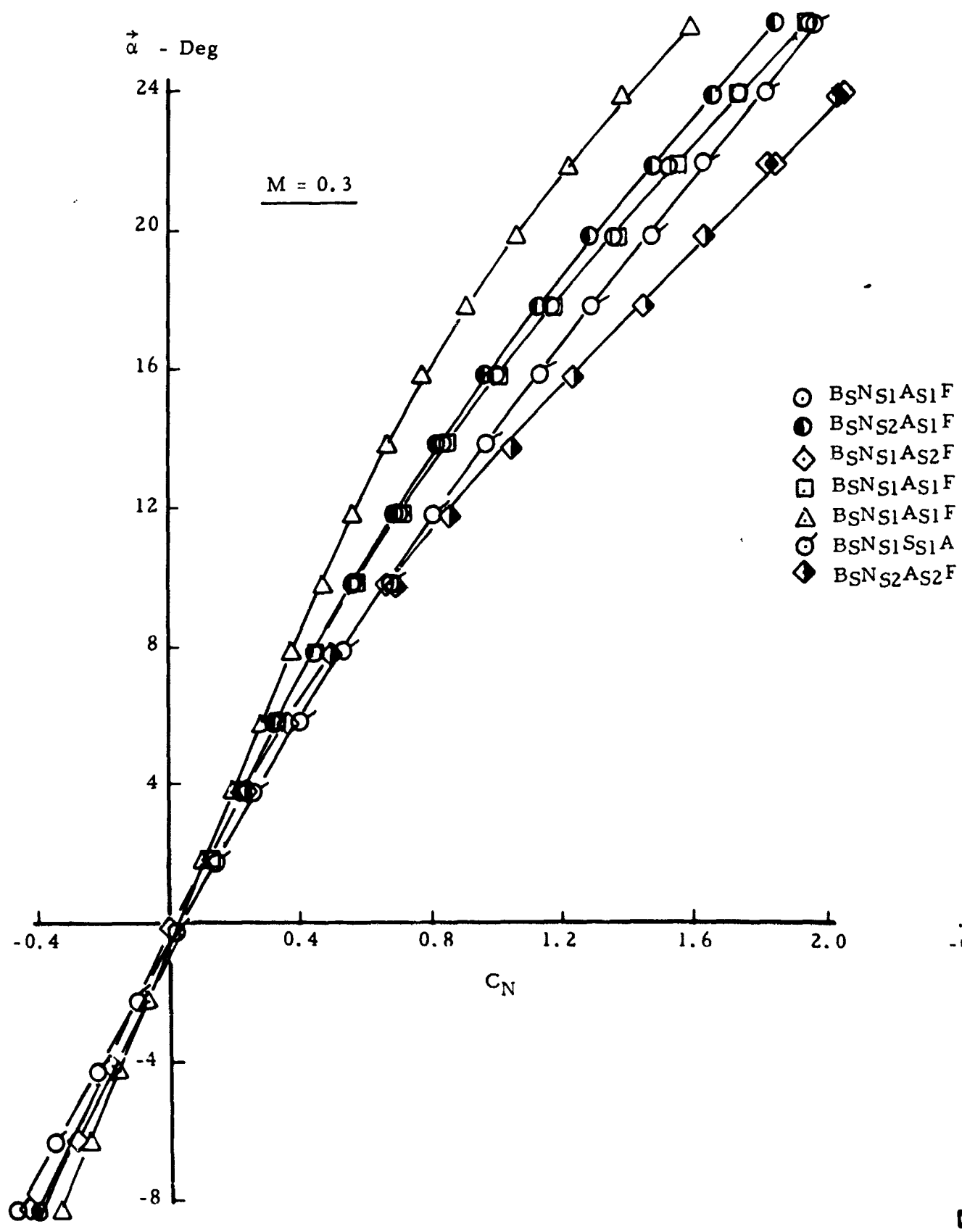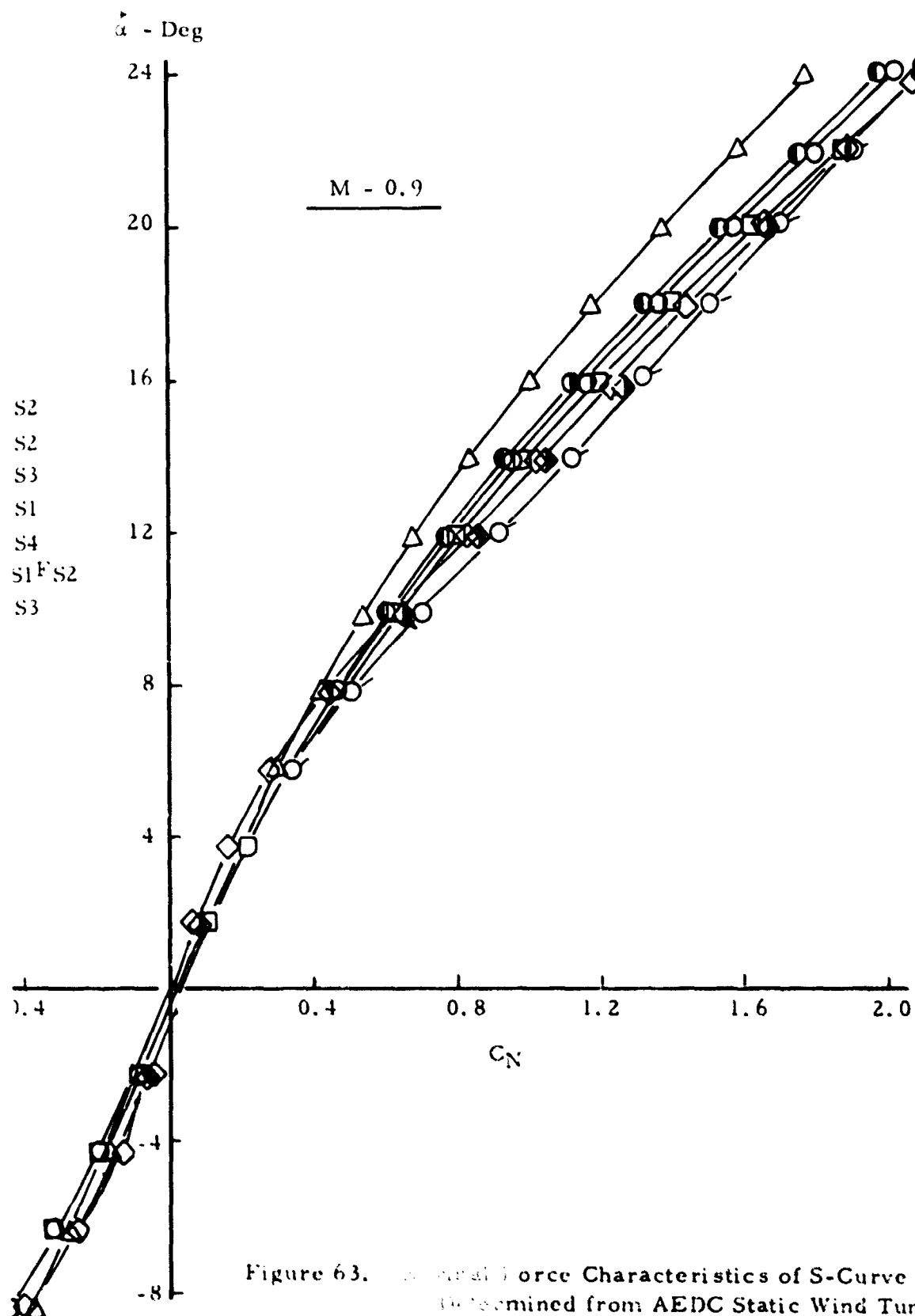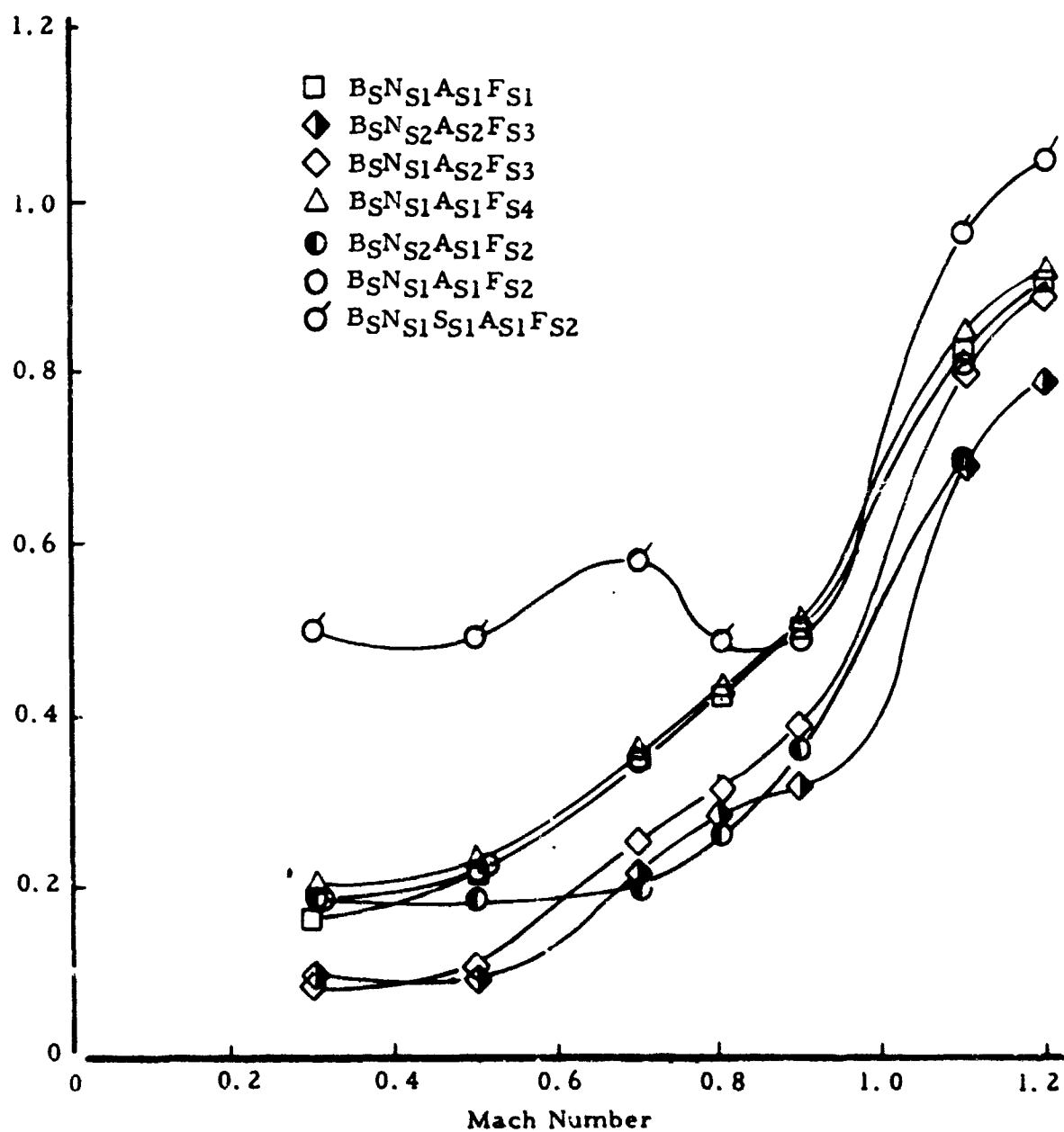
Figure 64.   Zero-Lift Drag Characteristics of S-Curve Bomblet Models
as Determined from AEDC Static Wind Tunnel Tests

111

(The reverse of this page is blank)

M 0. 3
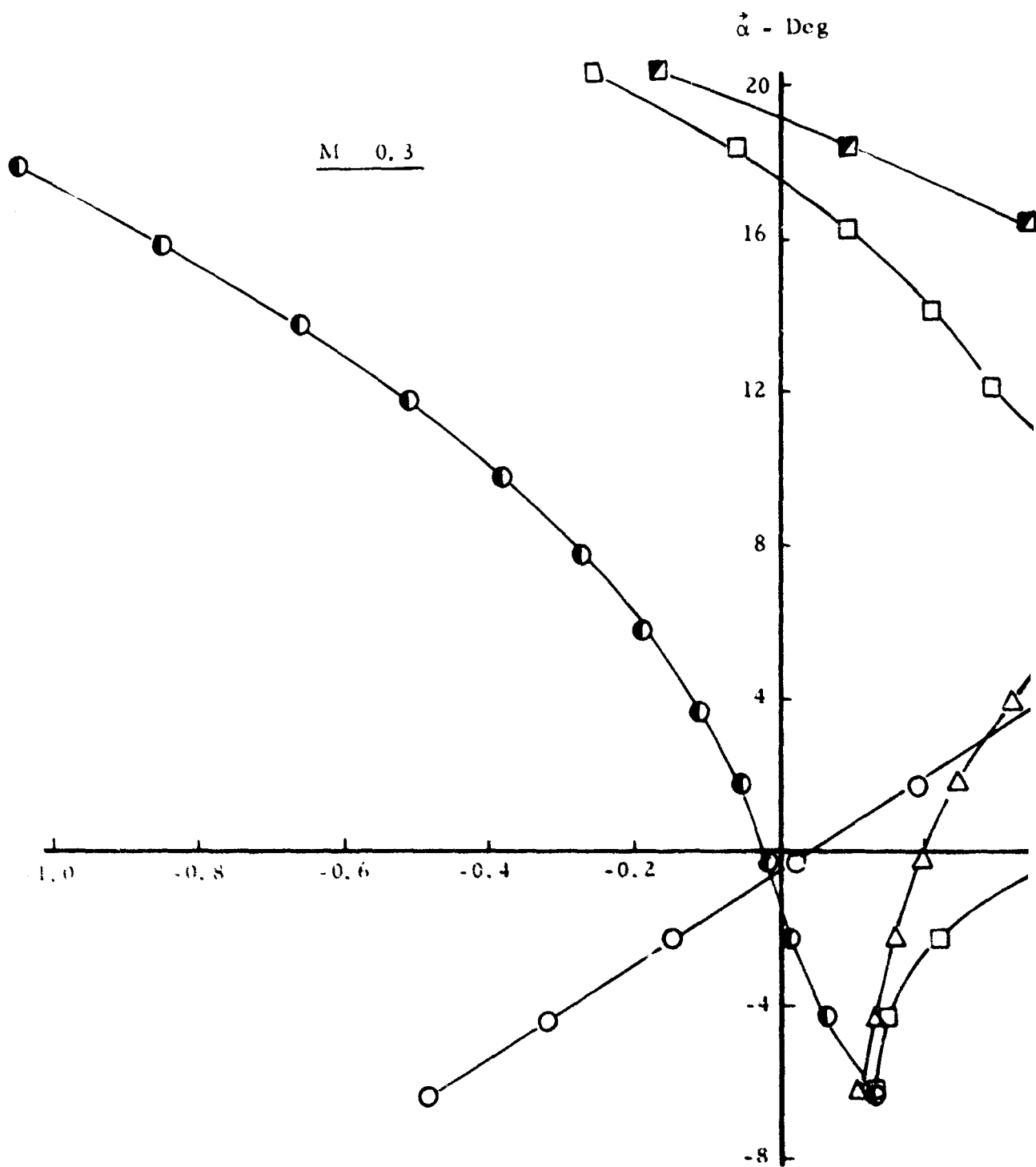
$\vec{\alpha}$ - Deg

Figure 65. Pitching Moment Characteristics of RTO Bomblet Model
as Determined from AEDC Static Wind Tunnel Tests

113

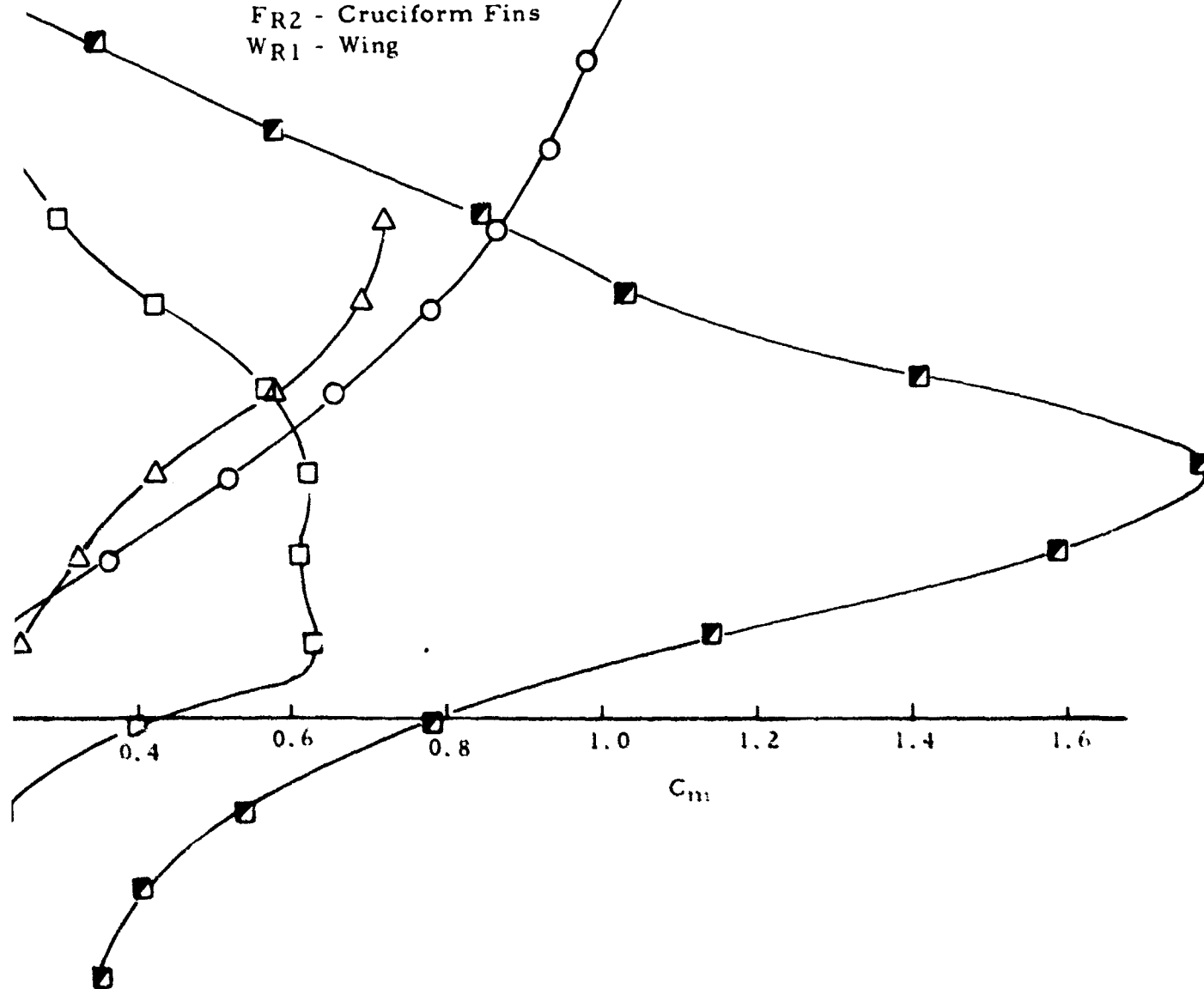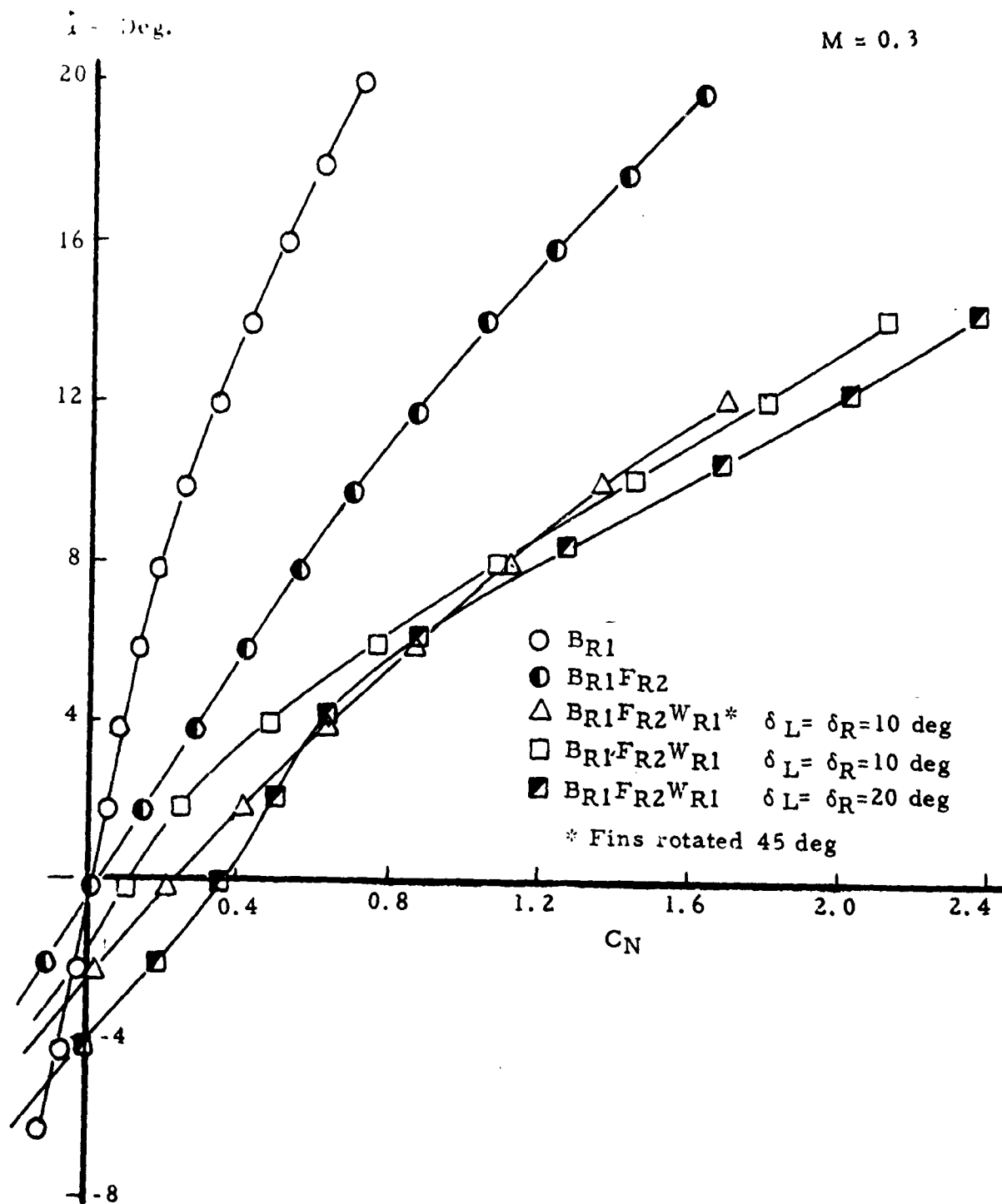Figure 66. Normal Force Characteristics of RT0 Bomblet Models as Determined from AEDC Static Wind Tunnel Tests

$(C_D) \vec{\alpha} = 0$
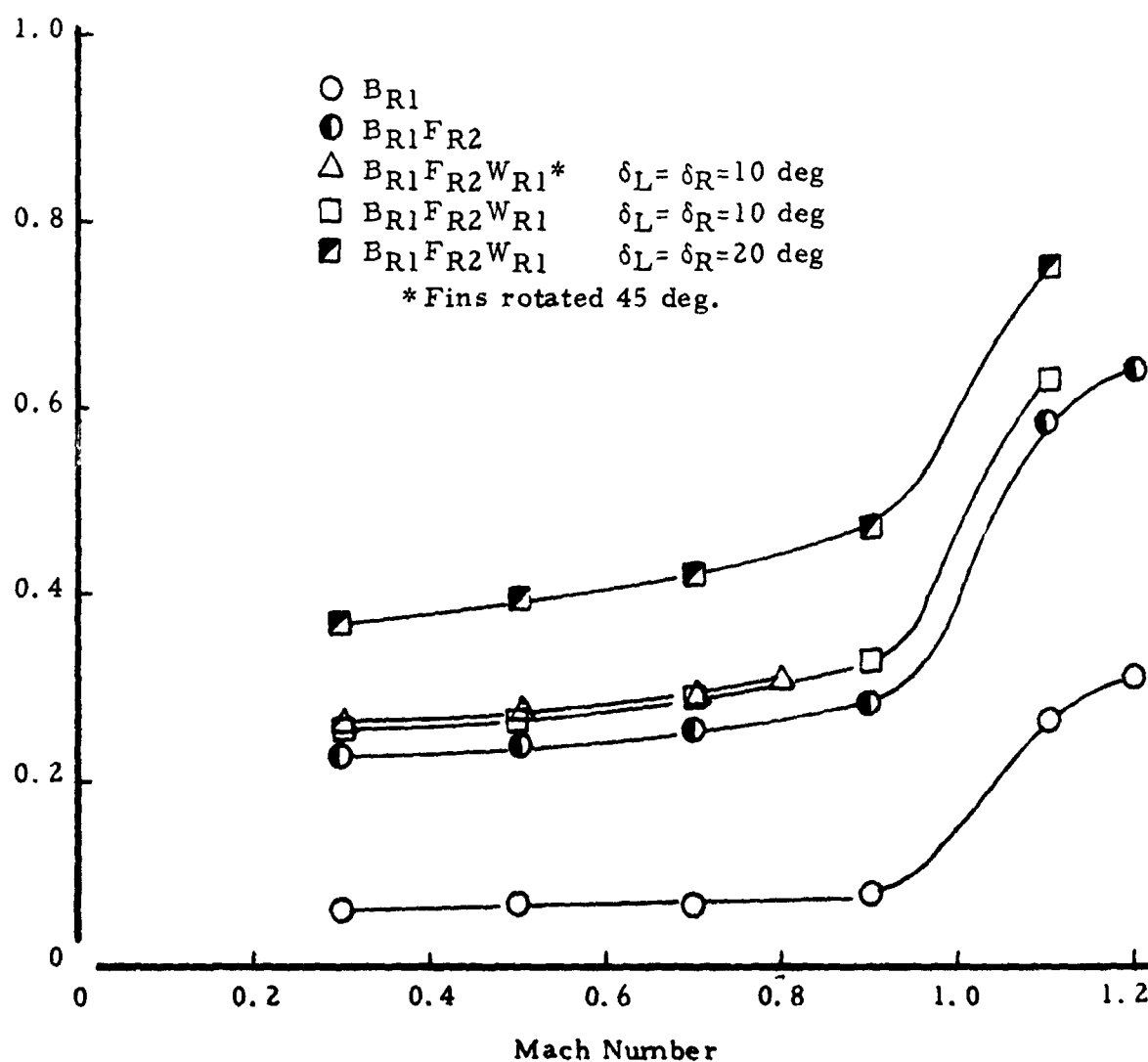
Figure 67. Zero-Lift Drag Characteristics of RT0 Bomblet Models as Determined from AEDC Static Wind Tunnel Tests

116

The roll moment, side force, and side moment characteristics, as a function of the aerodynamic roll angle, are described in Section II and illustrated in Figures 24 and 26.

Dual-Mode Bomblet. The static aerodynamic data for the dual-mode bomblets are presented in Figures 38 - 41 and described in Section II.

F.   PITCH DAMPING TESTS

A detailed description of the pitch damping tests of the S-curve bomblet models will be found in (21). The measured pitch damping characteristics of the basic configuration with hemisphere nose, $B_S N_{S2} A_{S1} F_{S2}$, are presented in Figure 68. The configuration has good damping at all Mach numbers and in both zero lift and trimmed flight attitudes. The blunt nose shape did not influence the damping appreciably except at transonic conditions where the blunt nose was slightly unstable. Configuration $B_S N_{S1} A_{S1} F_{S4}$, with the rounded fin cross-section, was stable at all conditions tested, but the damping for most flight conditions was not as good as the basic hemisphere-nose model. The nose spoiler was extremely effective at small angles of attack and low Mach numbers and also at large angles of attack at Mach 0.7. The spoiler was not effective at transonic conditions.

The damping characteristics of the boattail afterbody models were not determined because of model-sting clearance problems.

117

Figure 68. Pitch-Damping Characteristics of S-Curve Bomblet Model $B_SN_{S2}A_{S1}F_{S2}$, as Determined from AEDC Forced-Oscillation Wind Tunnel Tests

118

SECTION V.

CONCLUSIONS AND RECOMMENDATIONS

A.   CONCLUSIONS

Based on six-degrees-of-freedom motion simulations and available aerodynamic data, the following conclusions are made:

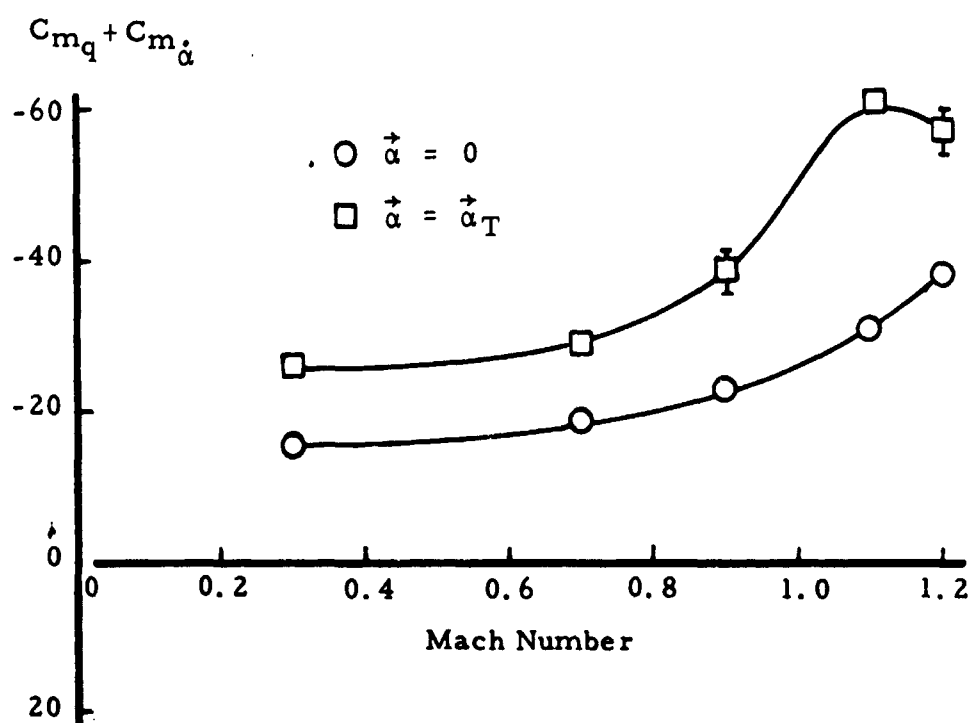1.   Each of the four proposed bomblet concepts investigated (S-curve, roll-through-zero, dual-mode, and spinning-disk) is feasible and capable of dispersing a cluster bomb over a wide area from a functioning altitude of 2000 feet or less.

2.   Under high-speed delivery conditions, the S-curve bomblet can disperse a warhead over an area 3500 feet in width from a dispenser functioning altitude of 300 feet.

3.   The performance of the S-curve type bomblet is extremely sensitive to accidental fin cant, longitudinal misalignment, trim variations with Mach number, and the attitude of the bomblet at release.

4.   The roll-through-zero (RTO) type bomblet can disperse a warhead over an area 800 feet in width under high-speed release conditions at 1000 feet altitude.

5.   The RTO-type bomblet is sensitive to induced roll moments from fin or wing orientation and lateral center-of-gravity offset but provides desirable dispersion variations with delivery airspeed and altitude, and the impact pattern distribution is readily modified by a change in the design roll torque.

6.   The vane-stabilized dual-mode bomblet can provide effective dispersion and ballistic impact under high-speed delivery conditions for dispenser opening altitudes in excess of 1000 feet.

7.   The dual-mode bomblet with 45 degrees trailing vane can accomplish transition from magnus-rotor flight to ballistic flight attitude in about 1.5 seconds (or within about 250 feet altitude); pitch-roll resonance and roll lock-in effects, due to accidental fin cant and longitudinal misalignment, do not significantly affect the angle-of-attack history during transition.

8.   The ballute-stabilized dual-mode bomblet requires about seven seconds for transition to ballistic flight and must be restricted to delivery altitudes of 2000 feet or greater.

119

9. The symmetrical spinning-disk bomblet has about the same dispersion as a spherical magnus rotor for a 900 ft/sec dispenser opening velocity, but the amount of dispersion which occurs due to the disk lift force at high velocities is small and equivalent to a radial velocity of about 20 ft/sec.

10. In comparison with the CBU-24 munition (BLU-26/B bomblet), the S-curve bomblet has greater area coverage capability for low-altitude high-speed delivery conditions, while the RT0 bomblet has about the same area coverage capability. For dispenser opening altitudes of 2000 feet or higher, the impact dispersion boundaries for the vane-stabilized dual-mode bomblet and BLU-26/B bomblet are approximately the same.

11. Within their operational envelopes, the proposed aerodynamic dispersion concepts provide greater area coverage than a force ejection system with 100 ft/sec radial velocity capability, except for low-altitude and low-speed (300 ft/sec) dispenser opening conditions.

B. RECOMMENDATIONS

The following recommendations are made for further investigation of the proposed dispersion concepts:

1. More accurate simulations of the S-curve and RT0 bomblet impact patterns should be accomplished by use of the Monte Carlo method. Appropriate statistical variations for the initial motion perturbations and the bomblet configurational asymmetries should be established.

2. Representative magnitudes for the asymmetries of existing bomblets (particularly fin cant and fin misalignment) should be determined, and the adequacy of existing manufacturing tolerances and quality control procedures for production of the S-curve and RT0-type bomblets should be investigated.

3. The dispersion characteristics of the S-curve and RT0 bomblets should be evaluated for supersonic delivery conditions, and the necessary supporting aerodynamic data for these calculations should be acquired from additional wind tunnel tests.

4. The aerodynamic characteristics of the S-curve and dual-mode type bomblets should be investigated more fully, particularly with respect to the pitch-yaw damping, magnus moment, and spin parameters. It would be desirable to obtain these data from dynamic tests, where the model has two or more degrees of angular freedom.

120

5. Free-flight testing of the S-curve and RT0 bomblets should be accomplished for verification of flight and dispersion characteristics. Both gun-launch and air-drop techniques should be exploited.

6. Further testing of the dual-mode bomblet concepts is warranted, with emphasis on stabilizer deployment.

7. Further investigations of asymmetrical versions of the spinning disk bomblet are warranted, to the extent that the disk shape is advantageous for warhead packaging and functioning.

8. Further geometric modifications of the proposed bomblet configurations should be studied as a means of improving dispersion, the attitude and flight path angles at impact, packaging, and warhead compatibility.

(The reverse of this page is blank)

APPENDIX I

DESCRIPTION OF AERODYNAMIC SYSTEM FOR BOMBLET MOTION SIMULATIONS

The six-degrees-of-freedom computer program used in conjunction with the present investigation[3] employs an aeroballistic system which is consistent with that which is used for symmetric missiles. With either body-fixed or fixed-plane coordinate axes, the orientation of the force and moment vectors can be described by two angle-of-attack parameters, $\vec{\alpha}$ and ξ , as depicted in Figure I-1. For computational purposes, the aeroballistic coefficients are scalar functions of $\vec{\alpha}$, Mach number and non-dimensional spin. Note also that C_{n_r} and C_{m_q} are specified independently and are related to q' and r', the components of the cross-angular velocity in the angle of attack and magnus planes, respectively. Thus, the difference between planar and circular motion damping can be distinguished.

Figure I-2 depicts additional body-fixed aerodynamic coefficients which can be introduced into the 6-DOF simulations. These include five coefficients which have a sinusoidal dependence upon the aerodynamic roll angle ϕ . The aerodynamic roll angle is defined in Figure I-3. All of the added body-fixed aerodynamic coefficients are functions of both $\vec{\alpha}$ and Mach number.

The other important roll orientation parameters are also described by Figure I-3. The angle ζ represents the angular displacement between the body axes and a symmetry plane and is used in conjunction with the investigation of lateral c.g. offset, etc. Otherwise, ζ is zero. The orientation of the angle of attack plane with respect to horizontal, angle $\bar{\phi}$, is frequently used for portrayal of the bomblet motion. For $\zeta = 0$, the angle $\bar{\phi}$ is related to ϕ and ϕ by the identity

$$\bar{\phi} = \pi/2 + \phi - \phi \text{ , radians; } \zeta = 0$$
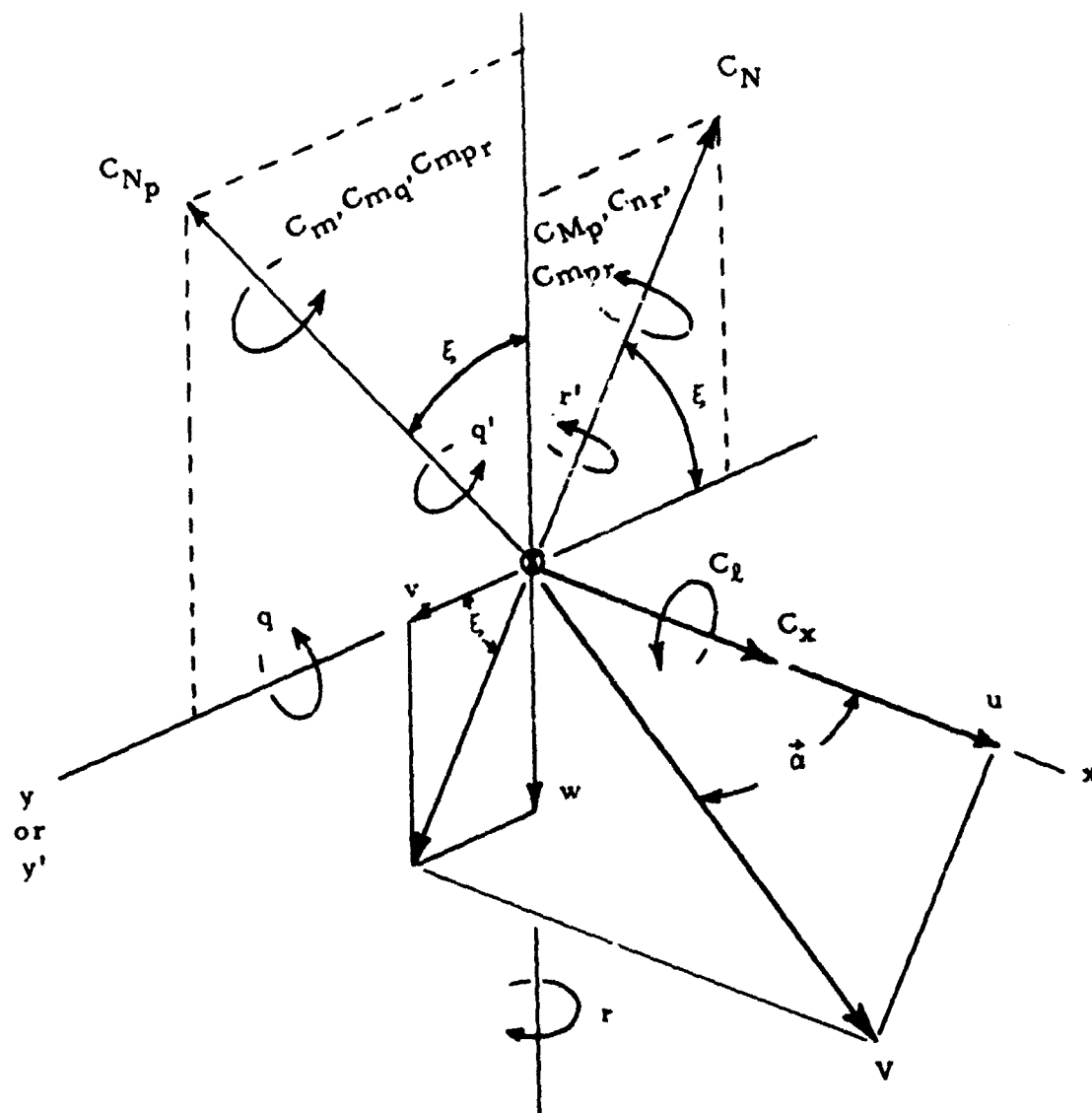
Preceding page blank

Figure 1-1. Aeroballistic Force and
Moment Coefficient Definitions

124
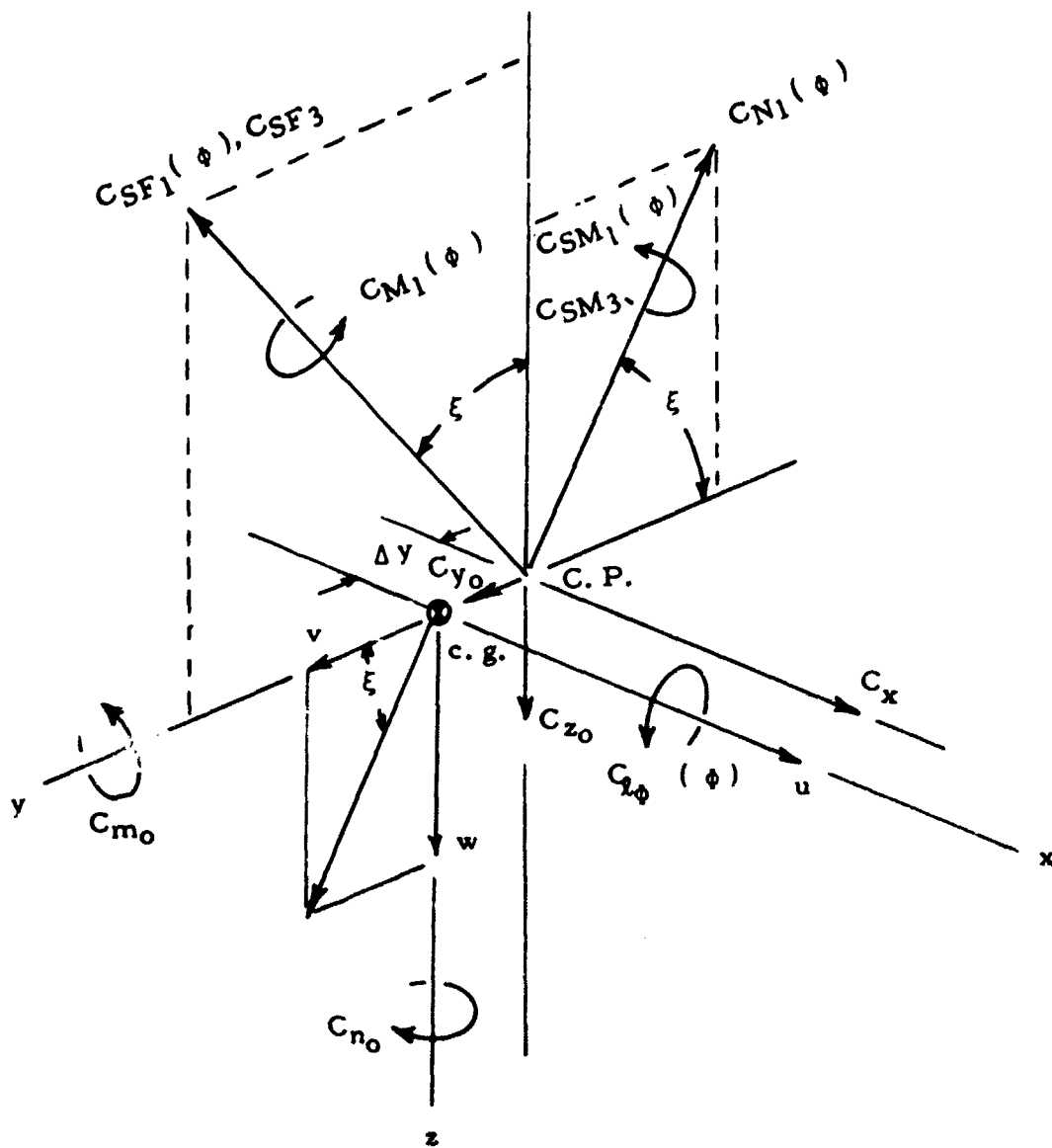
Figure 1-2. Additional Aerodynamic Forces and Moments for Body-Fixed Axes

125

Figure I-3. Roll Orientation Parameters

126

APPENDIX II

CONING MOTION ANALYSIS

First, the usual fixed-plane equations of motion are derived to show the basic coning motion. These equations are then transformed into a set of modified fixed-plane equations which are more convenient for analysis of motions which are influenced by gravity. The modified equations are used to investigate the requirements for zero coning motion.

The basic coordinate axes are depicted in Figure II-1. The x, y, z axes are a system of fixed-plane axes, wherein y always lies in the Y Z inertial reference plane, x is coincident with the body axis of symmetry, and z is directed such as to constitute a right-handed orthogonal system. The rotational velocity, $\vec{\Omega}$, of this triad with respect to the inertial system is given in terms of the Eulerian angles as

$$\Omega_x = \dot{\lambda} \cos \sigma$$

$$\Omega_y = \dot{\sigma}$$

$$\Omega_z = \dot{\lambda} \sin \sigma$$

while the angular velocity components of the body are given by

$$\omega_x = p = \dot{\phi} + \dot{\lambda} \cos \sigma$$

$$\omega_y = \dot{\sigma}$$

$$\omega_z = \dot{\lambda} \sin \sigma$$

Then from the fundamental rigid-body equations of motion

$$\vec{F} + m\vec{g} = m\dot{\vec{V}} + \vec{\Omega} \times m\vec{V}$$

$$\vec{M} = [I] \dot{\vec{\omega}} + \vec{\Omega} \times [I] \vec{\omega},$$

where

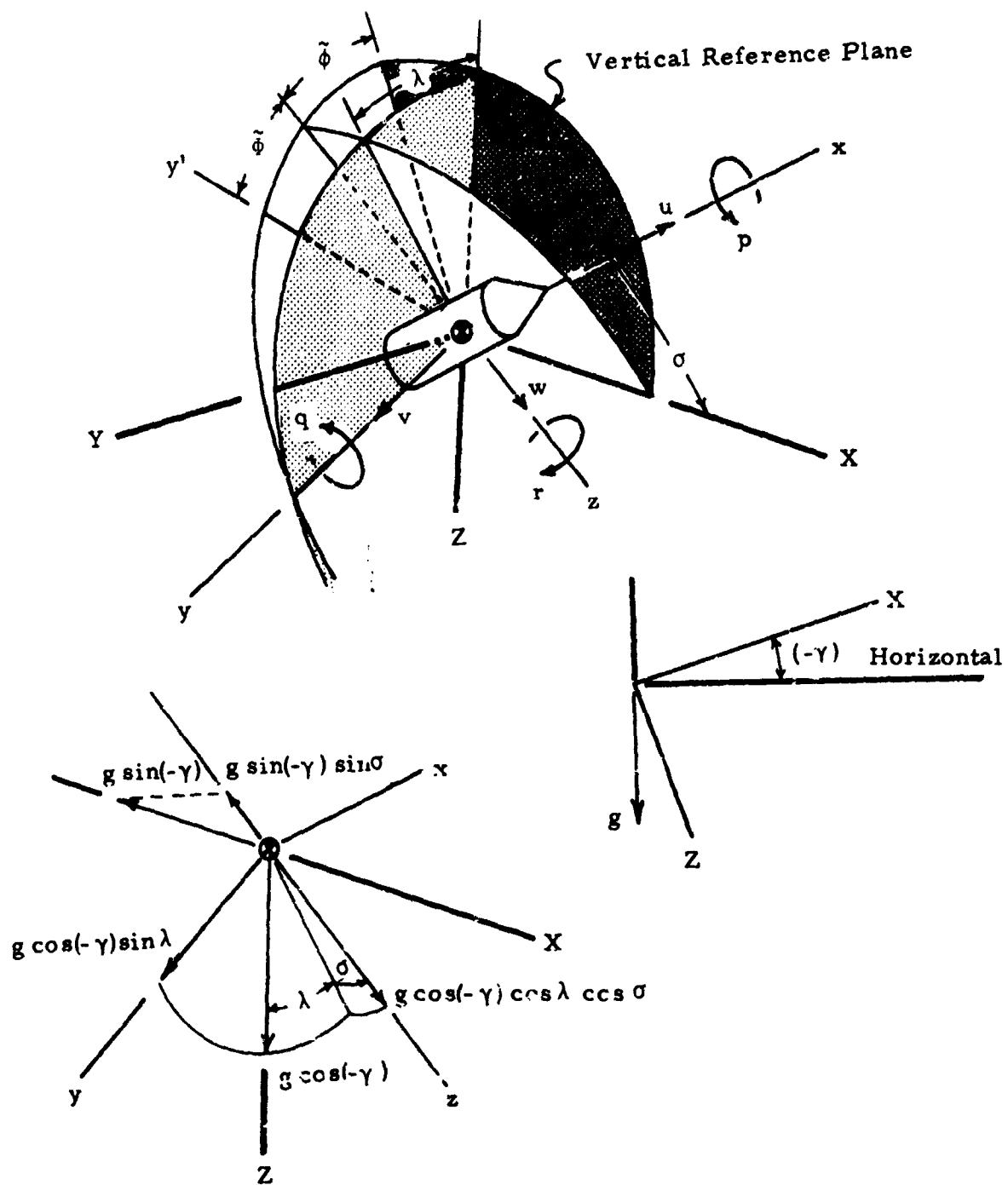$$[I] = \begin{bmatrix} I_x & 0 & 0 \\ 0 & I_y & 0 \\ 0 & 0 & I_z \end{bmatrix},$$

127

Figure II-1.   Coordinate Axes and Notation for
Coning Motion Analysis

the basic fixed-plane scalar equations are derived

$$\dot{v} + u\dot{\lambda}\sin\sigma - w\dot{\lambda}\cos\sigma = g\sin\lambda\cos(-\gamma) \qquad\qquad \text{(II-1)}$$

$$\dot{w} + v\dot{\lambda}\cos\sigma - u\dot{\sigma} = g[\cos(-\gamma)\cos\lambda\cos\sigma - \sin(-\gamma)\sin\sigma] \qquad \text{(II-2)}$$

$$-\frac{C_N\ \rho/2\ V^2\ S}{m}$$

$$I\ddot{\sigma} - I\dot{\lambda}^2\sin\sigma\cos\sigma + I_x p\dot{\lambda}\sin\sigma = [C_{m_q}\frac{\dot{\sigma}d}{2V} + C_M]\frac{1}{2}\rho V^2 Sd \qquad \text{(II-3)}$$

$$I\ddot{\lambda}\sin\sigma + 2I\dot{\lambda}\dot{\sigma}\cos\sigma - I_x p\dot{\sigma} = [C_{n_r}\frac{\dot{\lambda}d}{2V}\sin\sigma + C_{M_p}\frac{pd}{2V}]\frac{1}{2}\rho\ V^2 Sd \qquad \text{(II-4)}$$

For motions which involve negligible translation, the last two equations may be solved simultaneously. Steady-state coning solutions are obtained by letting $\ddot{\sigma} = \dot{\sigma} = \ddot{\lambda} = 0$. The resulting equations, even though nonlinear in σ, can readily be solved graphically or by other means to determine the limit cycle amplitude and frequency. Extensive analyses of these equations, including highly nonlinear magnus and damping moments, are described in (22) and (23).

In the present case, the translational motion, which includes the effects of the aerodynamic normal force and gravitational force, has a significant effect on the solutions, because the spin rate and magnus moment are expected to be small. To include the coupling of the force and moment equations, it is convenient to consider the following transformation of variables.

$$\dot{\phi} = \dot{\lambda}\cos\sigma \qquad\qquad \text{(II-5)}$$

$$r = \dot{\lambda}\sin\sigma \qquad\qquad \text{(II-6)}$$

These, together with the derivative of r,

$$\dot{r} = \ddot{\lambda}\sin\sigma + \dot{\lambda}\dot{\sigma}\cos\sigma \ , \qquad\qquad \text{(II-7)}$$

and the identity $q = \dot{\sigma}$ transform Equations (II-1) - (II-4) to a more symmetrical form: *

---

* This form of the equations of motion also avoids distinguishing between $\dot{\sigma}$ and $\dot{\alpha}$.

$$\dot{v} + ru - \dot{\tilde{\phi}} w = g \sin \lambda \, \cos \gamma \qquad\qquad\qquad (II-8)$$

$$\dot{w} - qu + \dot{\tilde{\phi}} v = g (\cos \gamma \cos\lambda \, \cos \sigma + \sin \gamma \sin\sigma) \qquad (II-9)$$

$$- \frac{C_N \, \rho/2 \, V^2 S}{m}$$

$$I \dot{q} - I \dot{\tilde{\phi}} r + I_x p r = [C_{m_q} \frac{qd}{2V} + C_M] \frac{1}{2} \rho V^2 S d \qquad (II-10)$$

$$I \dot{r} + I \dot{\tilde{\phi}} q - I_x p q = [C_{n_r} \frac{rd}{2V} + C_{M_p} \frac{pd}{2V}] \frac{1}{2} \rho V^2 S d \qquad (II-11)$$

The variable $\tilde{\phi}$ defines the angle of attack plane orientation as in Figure II-1. Equations (II-8) - (II-11) are nearly identical with those presented in (1).

If a small constant angle of attack is now assumed and the basic assumption made that the translational motion stays in phase with the angle of attack plane, the following simplifications can be introduced:

$$\dot{\alpha} = \ddot{\alpha} = 0$$

$$\cos \sigma = \cos \alpha = \cos \alpha_T \simeq 1$$

$$\sin \sigma = \sin \alpha = \sin \alpha_T \simeq \alpha_T$$

$$v = \dot{v} = 0$$

$$w \simeq u \, \alpha_T$$

With these assumptions, together with

$$\cos \lambda \simeq \cos \tilde{\phi}$$

$$\sin \lambda = \sin \tilde{\phi}/\cos \sigma \simeq \sin \tilde{\phi}$$

Equations (II-8) and (II-9) can be expressed as

$$r = \frac{g}{u} \sin \tilde{\phi} \, \cos \gamma + \dot{\tilde{\phi}} \, \alpha_T \qquad\qquad (II-12)$$

$$q = \frac{C_N \frac{1}{2} \rho V^2 S}{mu} - \frac{g}{u} (\cos\gamma \, \cos \tilde{\phi} + \alpha_T \sin \gamma) \quad (II-13)$$

Substituting r , q , and $\dot{r}$ into Equation (II-11) the special coning solution can be obtained

$$
I \, \alpha_T \ddot{\tilde{\phi}} - \left\{ \frac{I g \, \alpha_T \, \sin\gamma}{V} - \frac{I \, C_N \, \rho S V}{2m} + \frac{C_{n_r} \, \rho S d^2 V}{4} \alpha_T \right\} \dot{\tilde{\phi}} \qquad (II-14)
$$

$$
+ \left[\frac{I_x \, g \cos\gamma \cos\tilde{\phi}}{V} \right] p - \frac{C_{n_r} \, g \, \rho S d^2 \cos\gamma \, \sin\tilde{\phi}}{4} =
$$

$$
\left\{ \frac{C_{M_p} \, \rho S d^2 V}{4} + \frac{I_x \, C_N \, \rho S V}{2m} - \frac{I_x \, g \, \alpha_T \sin\gamma}{V} \right\} p
$$

APPENDIX III

SIMPLIFIED DISPERSION PREDICTION FOR ROLL-THROUGH-ZERO BOMBLET

ROLL DYNAMICS

An approximate solution for the dispersion of the roll-through-zero bomblet is formulated, using a simplification of the bomblet roll dynamics. The general form of the roll differential equation for a symmetric missile is

$$\phi'' + K_p \phi' - K_\delta = 0$$

which has the solution

$$\phi = \phi_o + \frac{K_\delta}{K_p} \hat{t} + \frac{1}{K_p} \left(\frac{K_\delta}{K_p} - \phi_o' \right) \left(e^{-K_p \hat{t}} - 1 \right) \tag{III-1}$$

where, for $V = $ constant

$$K_\delta = \frac{\rho S d^3}{2 I_x} \quad C_{\ell_\delta} \delta = \frac{C_{\ell_\delta} \delta}{2 I_x'}$$

$$K_p = -\frac{\rho S d^3}{4 I_x} \quad C_{\ell_p} = \frac{C_{\ell_p}}{4 I_x'}$$

$$C_{\ell_p} = \frac{\partial C_\ell}{\partial \frac{pd}{2V}}$$

$$\hat{t} = \left(\frac{V}{d} \right) t$$

and the derivatives are with respect to nondimensional distance $s = \frac{1}{d} \int V dt$. With $\phi_o = \phi_o' = 0$, Equation (III-1) reduces to

$$\phi = \frac{K_\delta}{K_p} \hat{t} + \frac{K_\delta}{K_p^2} \left(e^{-K_p \hat{t}} - 1 \right) \tag{III-2}$$

For the roll-through-zero bomblet, dispersion occurs while ϕ' is small, so that the damping moment is small during the dispersion phase.

132

Therefore, for small ϕ', and $\phi_0 = \phi_0' = 0$

$$\phi \simeq \frac{K_\delta}{2} \, \hat{t}^2 \tag{III-3}$$

A comparison of the solution for Equation (III-3) with that for Equation (III-2) for representative values of the parameters is shown in Figure III-1. As will subsequently be shown, the region of interest is between $\phi = 0$ and $\phi \simeq \pi/4$. It is seen that the time from zero roll rate to $\phi = \pi/4$ is only about 12 percent greater if Equation (III-2) is used instead of the approximation (III-3). Since the dispersion will be proportional to the time in the neighborhood of zero-roll rate, the use of the approximate roll solution for dispersion prediction should lead to conservative results.

LATERAL MOTION

The lateral motion of the bomblet due to a body-fixed trim angle of attack and/or asymmetric lateral force, over a short duration of flight, can be expressed in terms of earth-fixed coordinates y_e, z_e by the following equation

$$\frac{y_e' + i \, z_e'}{d} = \frac{C_N \, \rho S d}{2m} \int_{\hat{t}_o}^{\hat{t}_1} e^{i \phi} \, d\hat{t} \tag{III-4}$$

where we have arbitrarily let the lateral force coefficient, C_N, be directed along the real body axis, i.e., the body y axis. Equation (III-4) can be rewritten as

$$\frac{y_e' + i \, z_e'}{d} = \frac{C_N \, \rho S d}{2m} \left[\int_{\hat{t}_o}^{\hat{t}_1} \cos \phi \, d\hat{t} + i \int_{\hat{t}_o}^{\hat{t}_1} \sin \phi \, d\hat{t} \right] \tag{III-5}$$

With the approximation of the roll dynamics given by Equation (III-3), ϕ becomes

$$\phi = \frac{1}{2} \left(\frac{C_{\ell_\delta} \delta}{2 I_{x'}} \right) \quad .$$

133

$$C_{\ell_\delta}\ \delta\ = 0.00488$$
$$C_{\ell_p}\ \ \ = -1.03$$
$$I'_x\ \ \ = 450$$
$$d\ \ \ \ = 0.25$$

ϕ - Radians

$\phi = \dfrac{\pi}{4}$

Damping Neglected
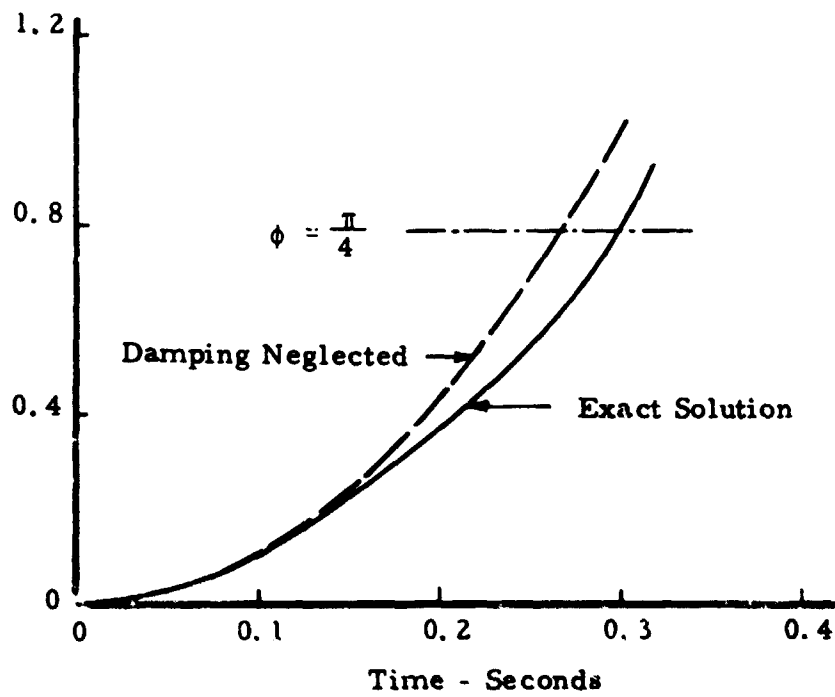
Exact Solution

Time - Seconds

Figure III-1. Roll Dynamics in the Vicinity
of Zero Roll Rate

Defining the arbitrary parameter u

$$u = \hat{t} \sqrt{\frac{C_{\ell_\delta} \delta}{2\pi I_x'}}$$

and letting $\hat{t}_o = 0$, Equation (III-5) can be expressed in terms of the standard Fresnel integrals

$$C(x) = \int_0^x \cos\left(\frac{\pi u^2}{2}\right) du$$

$$S(x) = \int_0^x \sin\left(\frac{\pi u^2}{2}\right) du$$

where $x = \sqrt{\frac{2\phi}{\pi}}$

Values of these integrals can be found in several texts, such as (24). Thus, the lateral motion from the time at which the spin rate is initially zero, to the time, $t = x$, can be expressed as

$$\frac{y_e' + i z_e'}{d} = \frac{C_N}{2m'} \sqrt{\frac{2\pi I_x'}{C_{\ell_\delta} \delta}} \left[C(x) + i S(x) \right] \tag{III-6}$$

Figure III-2 shows a typical solution of Equation (III-6) for representative values of the parameters. The various values of ϕ are indicated.

A useful property of the Fresnel integrals is that they have asymptotic values for $\phi \to \infty$:

$$C(x) = \frac{1}{2}$$

$$S(x) = \frac{1}{2}$$

In addition, the absolute value of the Fresnel integrals for $x = \infty$ is

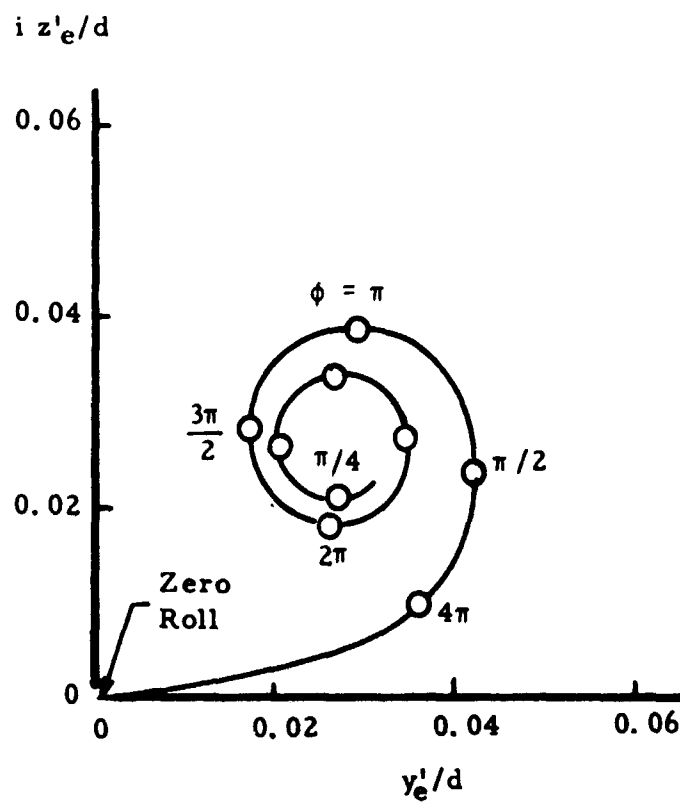$$\left| C(x) + i S(x) \right| = \frac{1}{\sqrt{2}}$$

135

Figure III-2. Typical Trajectory Deflection of Rolling Bomblet
Computed Using Fresnel Integrals

136

The same result is also approximated by

$$\left| C\left(x = \frac{1}{\sqrt{2}}\right) + i\, S\left(x = \frac{1}{\sqrt{2}}\right) \right| \approx \frac{1}{\sqrt{2}}$$

which with

$$x = \sqrt{\frac{2\phi}{\pi}} = \frac{1}{\sqrt{2}}$$

leads to

$$\phi \approx \frac{\pi}{4}$$

Therefore, starting from zero roll rate, the lateral deflection of the trajectory after rolling through an angle of $\phi = \pi/4$ is nearly identical to the deflection which would occur after a large number of roll cycles.

It is obvious that the roll rate history prior to roll-through-zero is the negative image of that which occurs after roll-through-zero, if the roll damping is neglected. Thus, the total deflection of the trajectory during the interval from $\phi = -\pi/4$ to $\phi = \pi/4$ is given by

$$\Delta Y = \left| \frac{y_e' + i\, z_e'}{d} \right| = 2\left| \frac{C_N}{2m'} \right| \sqrt{\frac{2\pi I_x'}{C_{\ell_\delta} \delta}} \left| C\left(\phi = \frac{\pi}{4}\right) + i\, S\left(\phi = \frac{\pi}{4}\right) \right|$$

$$= 2\left| \frac{C_N}{2m'} \right| \sqrt{\frac{2\pi I_x'}{C_{\ell_\delta} \delta}} \left| \frac{1}{\sqrt{2}} \right| \qquad (III-7)$$

$$= \left| \frac{C_N}{2m'} \right| \sqrt{\frac{\pi I_x'}{C_{\ell_\delta} \delta}}$$

RELATION BETWEEN TRAJECTORY DEFLECTION AND DISPERSION

If the ballistic coefficient, $W/C_D S$, is sufficiently large, the flight path following roll-through-zero is relatively straight. Thus, with the aid of Figure III-3, along-range dispersion at the ground, R , and the cross-range dispersion at the ground, r , can be evaluated from the simplified relationships:

$$r = \frac{h}{\sin \gamma} \Delta Y \qquad (III-8)$$

$$R = \frac{r}{\sin \gamma} = \frac{h}{\sin^2 \gamma} \Delta Y \qquad (III-9)$$
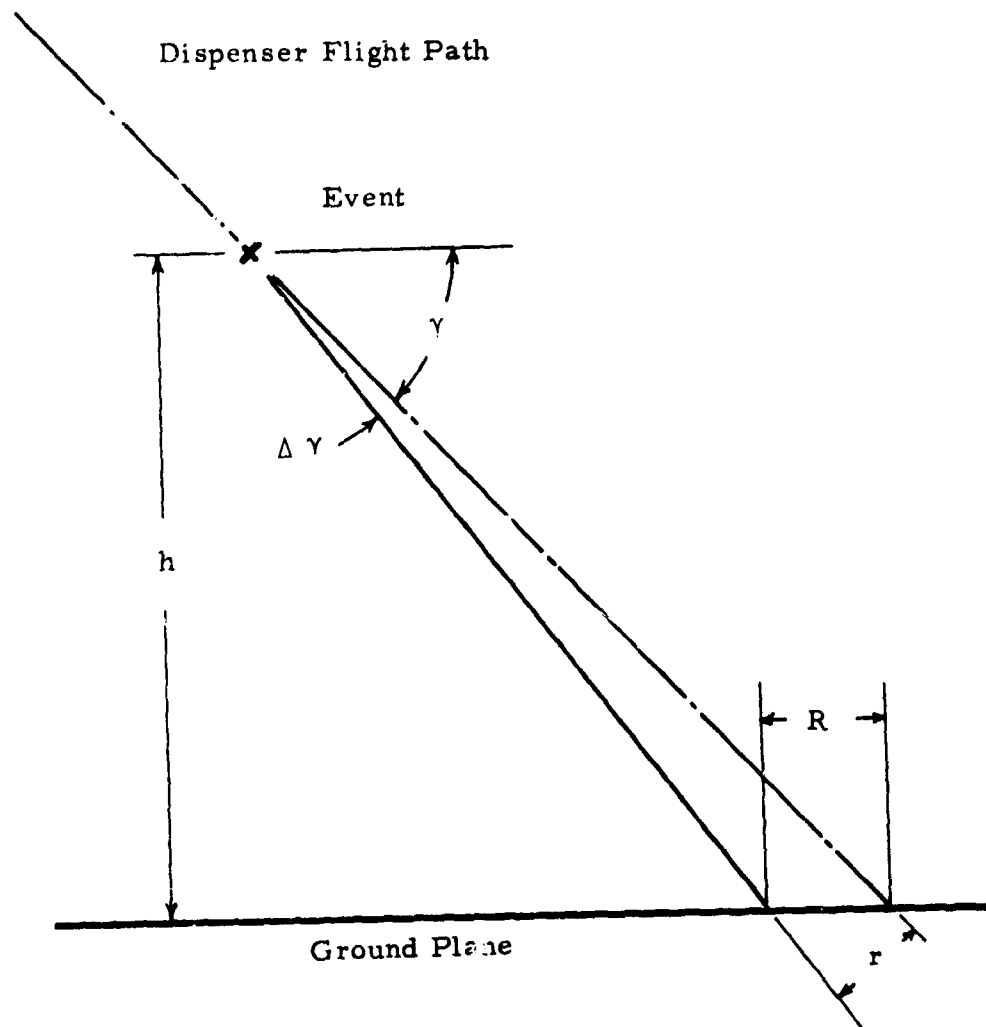
Figure III-3.   Ground Dispersion as Related
to Deflection of Trajectory

138

Substituting the result of Equation (III-7), the result is

$$r = \frac{h \, C_N}{2m' \sin \gamma} \sqrt{\frac{\pi \, I_x{'}}{C_{\ell_\delta} \delta}} \qquad \text{(III-10)}$$

$$R = \frac{h \, C_N}{2m' \sin^2 \gamma} \sqrt{\frac{\pi \, I_x{'}}{C_{\ell_\delta} \delta}} \qquad \text{(III-11)}$$

139

REFERENCES

1   Merchant, D. G. and R. L. Pope, "The Scattering of Bomblets by
    an Aerodynamic Method," Australian Defence Scientific Service,
    Weapons Research Establishment, Technical Note HSA 126, October
    1967 (Confidential).

2   Fletcher, C. A. J., "Wind Tunnel Tests on an Axisymmetric, Lifting
    Bomblet with Body Mounted, Rectangular Fins," Australian Defence
    Scientific Service, Weapons Research Establishment, Technical Note
    HSA 141, December 1968, AD 855 048.

3   Alpha Research, Inc., "User's Manual: Extended Capability Magnus
    Rotor and Ballistic Body 6-DOF trajectory Program," Air Force
    Armament Laboratory Report No. AFATL-TR-70-40, May 1970.

4   Shadow, T. O., "Wind Tunnel Investigation of the Transonic Static
    Stability Characteristics of Three Bomblet Munition Models Used in
    the Evaluation of Aerodynamic Dispersion Techniques," Arnold
    Engineering Development Center Report No. AEDC-TR-70-233,
    September 1970.

5   Brunk, James E., "Aerobee 150A Roll Lock-In Study," Alpha
    Research, Inc. Final Summary Report No. 65-9566-7, prepared for
    NASA Goddard Space Flight Center, Greenbelt, Md., under Contract
    No. NAS 5-9566, November 1965.

6   Alexander, Dr. J. D., Hayes International, "Dual Mode Magnus
    Rotor Bomblet," Proceedings of Conference on Dynamics and
    Aerodynamics of Bomblets, Air Force Armament Laboratory
    Report No. AFATL-TR-67-195, Vol. I, pages 389-418, October
    1967.

7   Falkowski, E. W., Picatinny Arsenal, "Static Stability and Spin
    Characteristics of Various Spherical and Cylindrical Bodies,"
    Proceedings of Conference on Dynamics and Aerodynamics of
    Bomblets, Air Force Armament Laboratory Report No. AFATL-
    TR-67-195, Vol. I, pages 357-389, October 1967.

8   Shortridge, W. K., Aerojet-General Corp., "Advanced Cylindrical
    Bomb (Fliptail)," Air Force Armament Laboratory Report No.
    AFATL-TR-69-38, March 1969, AD 502 528 (Confidential).

9   Brunk, James E., Alpha Research, Inc., "Aerodynamics and Flight
    Mechanics of Magnus-Rotor Bomblets, Volume III. Special Aero-
    dynamic Studies," Air Force Armament Laboratory Technical
    Report No. AFATL-TR-68-73, Volume III, June 1968.

REFERENCES (Continued)

10 Mikulas, Martin M., Jr., and Herman L. Bohon, NASA Langley
Research Center, "Summary of the Development Status of Attached
Inflatable Decelerators," AIAA Paper No. 68-929, presented at
AIAA 2nd Aerodynamic Deceleration Systems Conference, El Centro,
California, September 23-25, 1968.

11 Adams, Gaynor J. and Duane W. Dugan, "Theoretical Damping in
Roll and Rolling Moment Due to Differential Wing Incidence for
Slender Cruciform Wings and Wing-Body Combinations," NACA
Report 1088, 1952.

12 Bird, John D. and Charles P. Llewellyn, "An Analysis of the Stability
of Spinning Disks During Atmospheric Reentry," NASA Report No.
TM X-248, March 1960.

13 Anderson, H. K., G. Chadwick, and M. Degen, "Ballistic Range
Testing of Self-Dispersing Shapes," Avco Corporation, Missile Systems
Division, Report No. AVMSD-0154-66-RR, May 1966, AD 486 505.

14 Mugler, John P., Jr. and Walter B. Olstad, "Static Longitudinal
Aerodynamic Characteristics at Transonic Speeds of a Lenticular-
Shaped Reentry Vehicle," NASA TM-X-423, December 1960.

15 Demele, Fred A. and Jack J. Brownson, "Subsonic Aerodynamic
Characteristics of Disk Re-entry Configurations with Elliptic Cross
Sections and Thickness-Diameter Ratios of 0.225 and 0.325,"
NASA TM-X-566, May 1961.

16 Brunk, James E., "Aerodynamic Dispersion Techniques," Contract
Status Report No. 2 for Contract F-08635-70-C-0012, Alpha Research,
Inc. Report No. 69-0012-2, 15 December 1969.

17 Hunter, J. S., "Flight Performance of Self-Dispersing Fin Stabilized
Cylindrical Bomblets," Australian Defence Scientific Service,
Weapons Research Establishment, Technical Note HSA 151, May 1969,
(Confidential).

18 Crump, Earl W., "Analysis of Impact Pattern Data for BLU-26/B
Bombs Released from SUU-30 Type Dispensers," Air Force Armament
Laboratory Report No. AFATL-TR-69-18, February 1969, AD 502 563,
(Confidential).

19 Brunk, James E., "Aerodynamic Dispersion Techniques," Contract
Status Report No. 9 for Contract F-08635-70-C-0012, Alpha Research
Inc. Report No. 70-0012-8, 17 July 1970.

141

REFERENCES (Concluded)

20   Pitts, William C., Jack N. Nielsen and George E. Kaattari, "Lift and Center of Pressure of Wing-Body-Tail Combinations at Subsonic. Transonic, and Supersonic Speeds," NACA Report No. 1307, 1957.

21   Uselton, Bob, Jack Carman and Tom Shadow, "Dynamic Stability Characteristics of Axisymmetric Bomblet Munition Models at Mach Numbers 0.3 Through 1.2, "Arnold Engineering Development Center Report No. AEDC-TR-70-266, November 1970.

22   Brunk, James E., Alpha Research, Inc., "Aerodynamic Studies of Non-Planar and Near-Circular Motions," NASA Report No. CR-73067, 15 December 1966.

23   Brunk, James E., Alpha Research, Inc., "Some Aerodynamic Problems Associated with Large Angle of Attack Motions of Axisymmetric Bodies," Paper prepared for the 3rd Techincal Workshop on Dynamic Stability Problems, Nov. 4-7, 1968 at NASA Ames Research Center.

24   Davis, Leverett, Jr., James W. Follin, Jr. and Leon Blitzer, "The Exterior Ballistics of Rockets," D. Van Nostrand Company, 1958.

DOCUMENT CONTROL DATA - R & D

(Security classification of title, body of abstract and indexing annotation must be entered when the overall report is classified)

1. ORIGINATING ACTIVITY (Corporate author)	2a. REPORT SECURITY CLASSIFICATION
Alpha Research, Inc. Santa Barbara, California	UNCLASSIFIED
	2b. GROUP —

3. REPORT TITLE

AERODYNAMIC DISPERSION TECHNIQUES

4. DESCRIPTIVE NOTES *(Type of report and inclusive dates)*

Final Report (6 October 1969 to 6 October 1970)

5. AUTHOR(S) *(First name, middle initial, last name)*

James E. Brunk

6. REPORT DATE	7a. TOTAL NO. OF PAGES	7b. NO. OF REFS
November 1970	153	24

8a. CONTRACT OR GRANT NO. F08635-70-C-0012 ✓	9a. ORIGINATOR'S REPORT NUMBER(S)
b. PROJECT NO.	
c.	9b. OTHER REPORT NO(S) *(Any other numbers that may be assigned this report)* AFATL-TR-70-123
d.	

10. DISTRIBUTION STATEMENT This document is subject to special export controls and each transmittal to foreign governments or foreign nationals may be made only with prior approval of the Air Force Armament Laboratory (DLRA), Eglin AFB, Florida 32542.

11. SUPPLEMENTARY NOTES	12. SPONSORING MILITARY ACTIVITY
Available in DDC	Air Force Armament Laboratory Air Force Systems Command Eglin Air Force Base, Florida

13. ABSTRACT

The motion and dispersion characteristics of four proposed types of aerodynamic self-dispersing bomblets (S-curve bomblet, roll-through-zero bomblet, dual-mode bomblet, and spinning-disk bomblet) are evaluated for representative tactical cluster-dispenser delivery environments. Six-degrees-of-freedom simulations are used to investigate the flight dynamics of each type bomblet, and in addition, approximate motion theories are developed for the S-curve and roll-through-zero bomblets. The effects of various configurational asymmetries on the motion and dispersion are considered. Impact patterns are computed for each of the proposed bomblets, and the area coverage capabilities are compared for low-speed and high-speed dispenser opening conditions, ranging in altitude from 300 to 2000 feet and flight path angle from 5 to 45 degrees. The area coverage of the proposed bomblets is contrasted with that of the CBU-24 munition and a hypothetical radial-force-ejection system. The aerodynamic characteristics of each type bomblet are reviewed, and the problems of selecting candidate configuration are discussed. Results of supporting wind tunnel tests, accomplished in the 4T transonic wind tunnel at the Arnold Engineering Development Center (AEDC), are briefly described.

DD FORM **1473** (1 NOV)

14 KEY WORDS	LINK A		LINK B		LINK C	
	ROLE	WT	ROLE	WT	ROLE	WT
Aerodynamic self-dispersing bomblets						
S-curve bomblet						
Roll-through-zero bomblet						
Dual-mode bomblet						
Spinning-disk bomblet						
Flight dynamics						
Radial-force-ejection system						
Impact pattern characteristics						
Coning motion analysis						